MEASUREMENTS IN HORIZONTAL AIR-WATER PIPE FLOWS USING WIRE-MESH SENSORS

Étienne Lessard

A thesis submitted to the Faculty of Graduate and Postdoctoral Studies

In partial fulfilment of the requirements of the degree of

Master of Applied Science

In Mechanical Engineering

Department of Mechanical Engineering

University of Ottawa

Ottawa, Ontario, Canada

Abstract

This thesis is concerned with the performance and measurement uncertainty of wire-mesh sensors in different air-water flow regimes in horizontal pipes. It also presents measurements of void fraction and interfacial velocity in such flows. It was found that the interfacial velocity measurements of the wire-mesh sensors were in good agreement with those taken with a high-speed camera and estimates of the uncertainties of these measurements are presented. Drift-flux models were fitted to the measurements and it was found that the parameters of these models were not only sensitive to the flow regime, but also to the liquid superficial velocity.

Cette thèse porte sur la performance et l'incertitude de mesure du capteur treillis (*wire-mesh sensor*) sous différents régimes d'écoulement air-eau dans un tube horizontal. Elle présente des mesures de fraction vide (porosité) et de vélocité d'interface dans de tels écoulements. Ces vélocités furent comparées et jugées en bon accord avec celles mesurées par un caméscope haute-vitesse, et les incertitudes associées à ces mesures sont calculées et présentées. Des modèles de flux de dérive (*drift-flux models*) sont adaptées aux mesures, et il fut découvert que les paramètres composant ce modèle sont non seulement sensibles au régime de l'écoulement, mais aussi à la vélocité superficielle du liquide.

Acknowledgements

I wish to thank my supervisor, Dr. Stavros Tavoularis, for his guidance and insight throughout the redaction of my thesis. His meticulous care for the presentation and structure of my thesis has been much appreciated, and made me judge my own work through a different perspective. I also wish to thank especially Hassan Shaban and Aurelian Tanase, for their help with the operation of the flow loop and programming. My sincere thanks go to my lab colleagues, Laura Brown, Christina Vanderwel, George Choueiri and Amir Behnamian. I thank my family for their continuous support of my studies over the last years. I couldn't have done it without them. I finally wish to thank the workshop staff of the University of Ottawa for their assistance in building and installing the flow loop. My sincere thanks go to John Perrins, James McDermid, Leo Donner, Stanley Weedmark and Mike Burns.

This research has been funded by the Natural Sciences and Engineering Research Council of Canada (NSERC), the Atomic Energy of Canada Limited (AECL) and the University Network of Excellence in Nuclear Engineering (UNENE).

Table of contents

List of tables

List of figures

Nomenclature

Symbol	Property	Units
A_{cs}	total cross-sectional area	m^2
A_g	cross-sectional area occupied by the gas	m^2
$a_{i,j}$	area weight coefficient of the node located in row *i* and column *j*	dimensionless
c_0	distribution parameter	dimensionless
D	inner diameter of pipe	mm
e	percent difference	
$\overline{e}$	average percent difference	
f	frequency	Hz
f_{meas}	measurement frequency	Hz
G	mass flux	kg/m^2s
j	total superficial velocity / volumetric flux	m/s
j_l	superficial velocity of the liquid	m/s
j_g	superficial velocity of the gas	m/s
k	frame number	dimensionless
L	axial spacing between the two sensors	mm
N_i	number of rows	dimensionless
N_j	number of columns	dimensionless
N_k	number of frames	dimensionless
p	pressure	kPa
$p°$	standard atmospheric pressure	kPa

p_{rot}	air pressure at rotameter	kPa
Q	volume flow rate	m^3/s
S	wire spacing	mm
T	temperature	°C
T_{rot}	air temperature at rotameter	°C
t	time	s
$\mathcal{U}$	interfacial velocity	m/s
U_g	gas velocity	m/s
u	uncertainty of subscripted property	same units as property
V	volume	L
V	voltage signal of measured value	mV
v_{gj}	drift velocity	m/s

Greek symbol	**Property**	**Units**
β	factor based on number of detected interfaces	
Δk_p	frame shift at peak correlation	
Δk_s	frame shift	
Δx	axial distance separating the measurement planes of the sensors	m
ε	void fraction	dimensionless
ε'	void fraction fluctuation	dimensionless

Symbol	Property
$\overline{A}$	time-average of property A
$[A]$	rounding of property A to the nearest integer

Subscript / Superscript	Description
$chauvenet$	Chauvenet criterion parameter
cs	cross-section
fm	flowmeter
g	gas
gl	gas to liquid
hc	histogram calibration
hsp	high-speed photography
i	row number (1 to 8)
j	column number (1 to 8)
l	liquid
lg	liquid to gas
r	reference (at standard conditions)
rms	root mean square
tac	time-averaged calibration
V	volumetric
wms	wire-mesh sensor

Acronym	Description
AECL	Atomic Energy of Canada Limited
CANDU	Canada Deuterium Uranium
ECIS	emergency coolant injection system
HZDR	Helmholtz-Zentrum Dresden-Rossendorf
I.D.	inner diameter
LDV	laser Doppler velocimetry
LOCA	loss of coolant accident
O.D.	outer diameter
PC	personal computer
PIV	particle image velocimetry
SCH	schedule
USB	universal serial bus
WMS	wire-mesh sensor

Chapter 1 Introduction

1.1 Motivation

Multiphase flows, defined as flows of mixtures of several distinct phases of a fluid separated by an interface, are a common occurrence in a variety of industrial and engineering applications. Gas-liquid flows are of particular relevance to the operation and safety analyses of nuclear reactors, including the CANDU (Canada Deuterium Uranium) reactor.

The cores of CANDU reactors (Figure 1) are composed of many fuel channels, each containing rod bundles that are heated by pellets of nuclear fuel. These fuel channels are housed in a low-pressure vessel, called the calandria. The fuel elements (rods) are cooled by high-pressure heavy water flowing in the fuel channels, which is collected in the outlet header and then directed to the steam generator, where it transfers the absorbed heat to low-pressure light water. The coolant from the steam generator is then fed to the coolant pump, which pressurizes and directs the flow to the inlet headers. The inlet and outlet headers are horizontal tanks connected to the fuel channels by pipes, called feeders. These headers provide steady coolant flow to each fuel channel during normal reactor operation. Throughout this process, the heavy water remains in the liquid phase.

In the event of a loss of pressure or coolant accident (LOCA), the reactor is designed to shut down and trigger the Emergency Coolant Injection System (ECIS), which injects high-pressure light water to rapidly enhance the core cooling. In this scenario, however, boiling is expected to occur, resulting in a gas-liquid flow. The phase distribution in the various feeders under these circumstances is not necessarily uniform, and some fuel channels may receive less liquid to cool the fuel rod bundles than others. To ensure that all the fuel channels are cooled adequately, liquid flow distribution in each of the feeders needs to be measured or predicted accurately.

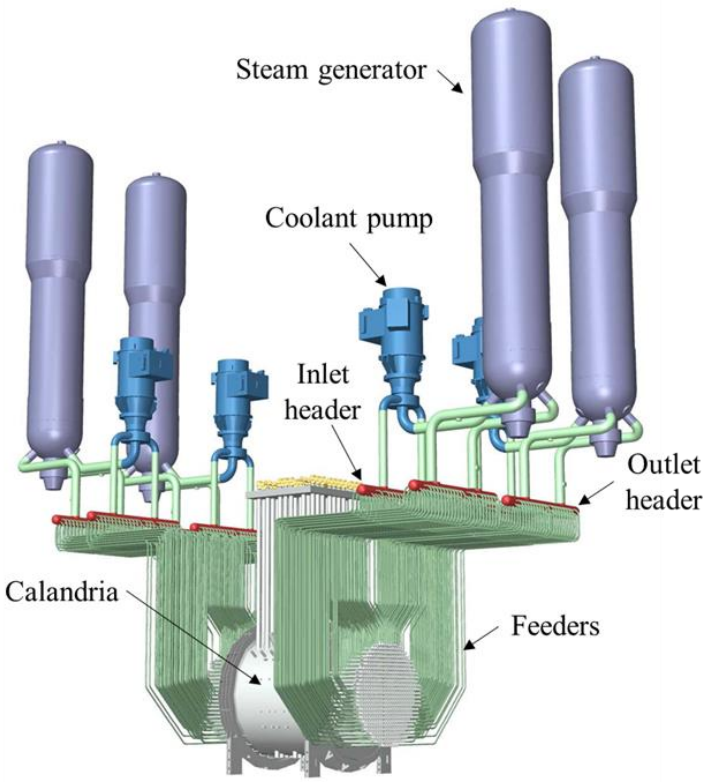

Figure 1: Overview of a CANDU reactor (from canteach.candu.org)

The velocity distribution of single-phase water flows in pipes can be measured by several well established optical methods, including laser Doppler velocimetry (LDV) and particle image velocimetry (PIV), as well as intrusive methods, such as hot film anemometry (Collier, 1994; Crowe, 2006; Balachandar, 2010). Although a number of techniques have also been developed for the measurement of velocity and phase distributions in gas-liquid flows in pipes, this remains a challenging problem, particularly for systems which do not permit optical access.

The wire-mesh sensor (WMS) method is a promising approach for measuring the quality of gas-liquid flows in pipes, but its application has so far been limited and its measurement uncertainty and extent of its applicability remain to be determined. Although this sensor is an intrusive device, and creates flow disturbance and pressure drop, it has certain advantages compared to alternatives. It is not hazardous like radiation

methods, it permits multi-sensor measurements at a relatively low cost compared to most optical methods, and does not require flow seeding.

The scope of this research includes both experimental and computational aspects, as well as experimentation in horizontal pipe flows, vertical pipe flows and header/feeder models.

The Atomic Energy of Canada Limited (AECL) Chalk River Laboratories has recently commissioned a test facility, in order to investigate the phase distribution of air-water flow in a header model (Figure 2). The inlet and outlet headers are connected by twelve banks of six feeders, leaving the headers at different inclinations. Void fraction is measured in each vertical and horizontal section of the feeders and in the inlet turret and discharge locations in the headers by wire-mesh sensors. Interfacial velocity is also measured in the two vertical sections and the horizontal section of the feeders simultaneously by pairs of WMS separated by a flange, as shown in Figure 3.

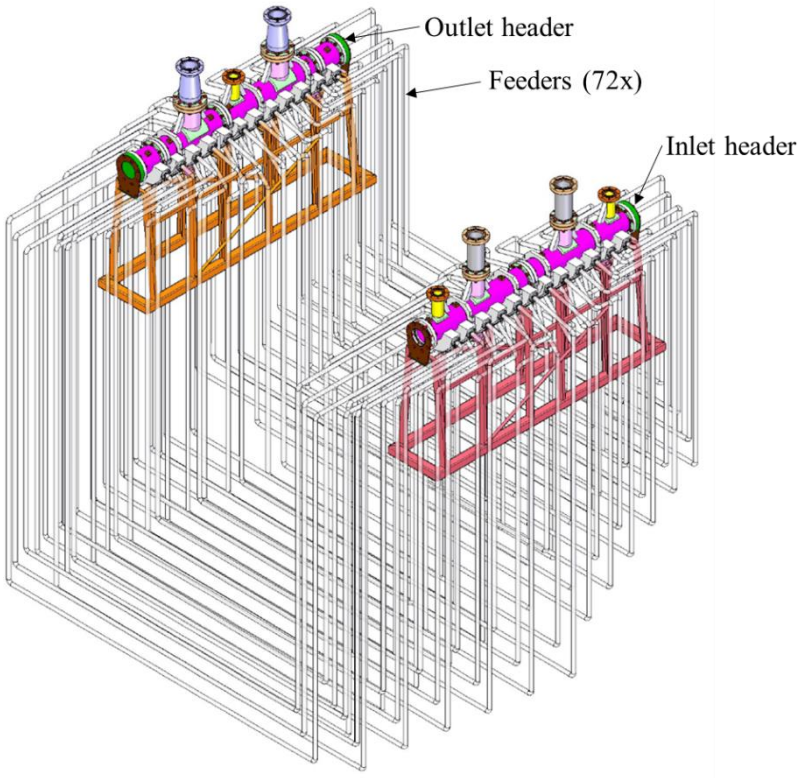

Figure 2: AECL air-water flow facility (Yang, 2013)

The work presented in this thesis is in support of the AECL header/feeder research, specifically in the study of horizontal air-water pipe flow. It is part of a research program at the University of Ottawa, which includes both experimental and computational studies of air-water flows in horizontal and vertical pipes and in simplified header/feeder models.

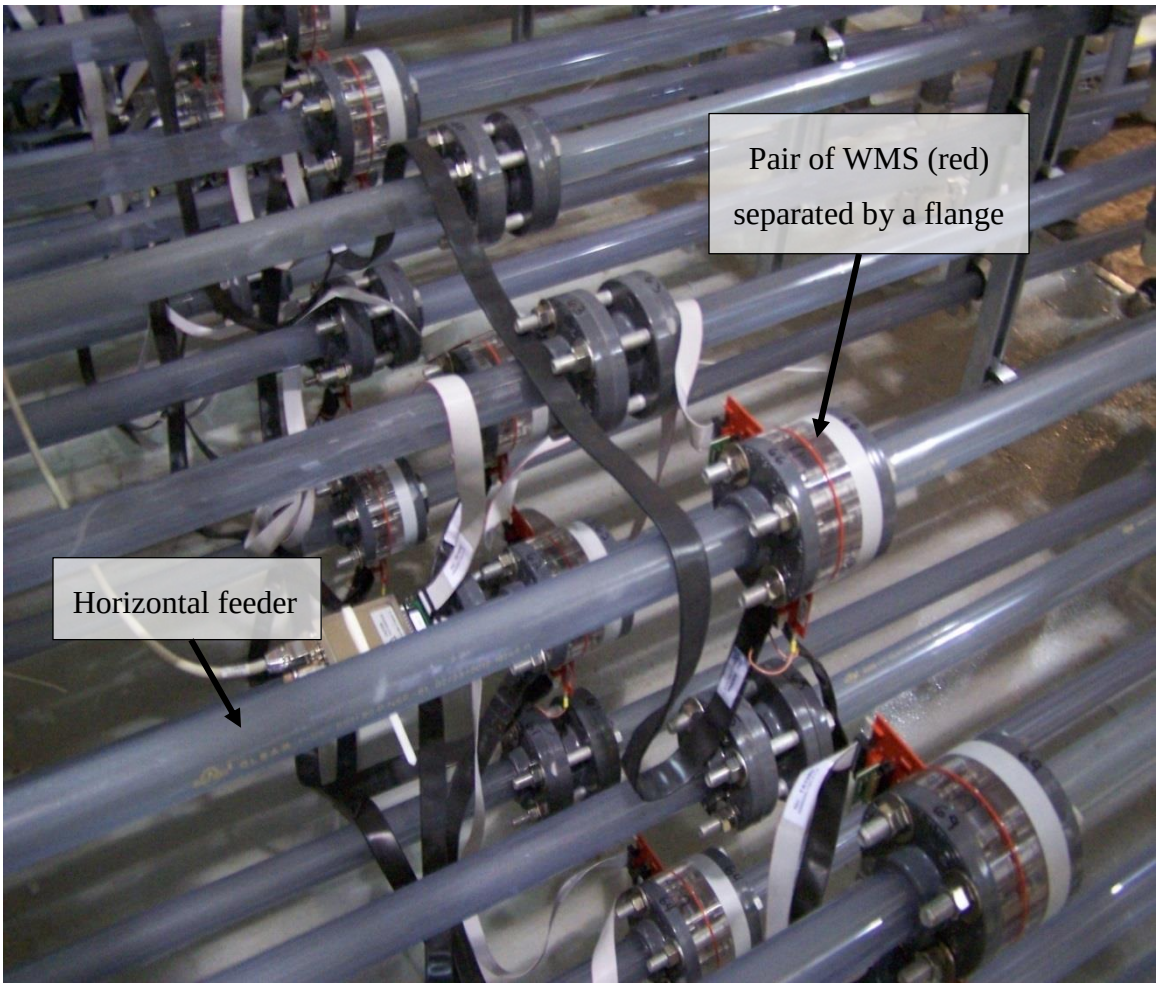

Figure 3: WMS installed on horizontal feeders (Yang, 2013)

1.2 Objectives

The objective of this thesis research is to evaluate and document the resolution and measurement uncertainty of wire-mesh sensors in adiabatic air-water flows in a horizontal pipe and to conduct measurements of liquid and gas velocities, void fraction, and interfacial velocities in such flows.

The main tasks are as follows.

- Design, construct and commission an experimental air-water flow loop capable of operating in a wide range of flow regimes.
- Perform tests in air-water flow under all flow regimes.
- Determine the uncertainty of the wire-mesh sensors for measuring void fraction and interfacial velocities.
- Compare interfacial velocity measurements from the WMS to those taken from high-speed photography.
- Determine, at least qualitatively, the disturbance caused by the WMS on the flow.
- Evaluate the accuracy of available drift-flux models for the prediction of void fraction in air-water horizontal flows.

1.3 Thesis outline

Characteristics of gas-liquid flows in horizontal pipes are first described in Chapter 2, including the various flow patterns typically observed. A summary of methods used for measurements in gas-liquid flows is also included in this chapter. The principles of operation of the WMS are outlined, and an overview of some previous work done with this device is presented. The air-water facility used for the present experiments is discussed in Chapter 3. The main components of interest in this setup are the sensors and the test section where they reside. An overview of the instrumentation is also provided; further details on these may be found in the Appendix. Details of the procedures used to obtain and process the signal of the WMS are expanded upon in Chapter 4; further details, including computer codes used to process the data are found in the Appendix. The results of the experiments are presented in Chapter 5 and a drift-flux model and its analysis is discussed in Chapter 6.

Chapter 2 Background

In this chapter, various fluid mechanics concepts that will be recurring within this thesis will first be defined. An overview of the previous work that has been done in the fields of research which relate to this project is presented, mainly in the area of horizontal flow patterns and prediction methods. Finally, several prior projects involving the wire-mesh sensor and a highlight of their results will be mentioned.

2.1 Basic definitions for gas-liquid flows

In the study of two-phase flow, there are four different common definitions for the void fraction: the local void fraction, the chordal void fraction, the cross-sectional void fraction, and the volumetric void fraction (Thome, 2004).

The local void fraction refers to a very small volume, which may be considered to be a point in the flow. It has two possible values: it is either null (or 0%), if liquid is present at that point, or unity (or 100%), if gas is present.

The chordal void fraction $\varepsilon_{chordal}$ is the average void fraction observed over a given length; it is defined as the ratio of the length L_g occupied by the gas and the total length L

$$\varepsilon_{chordal} = \frac{L_g}{L} \tag{1}$$

The cross-sectional void fraction ε_{cs} is defined as the ratio of the cross-sectional area A_g of the channel occupied by the gas phase and the total cross-sectional area A_{cs}

$$\varepsilon_{cs} = \frac{A_g}{A_{cs}} \tag{2}$$

Finally, the volumetric void fraction ε_V in a channel is defined as the ratio of the volume V_g occupied by the gas and the total volume V

$$\varepsilon_V = \frac{V_g}{V} \tag{3}$$

As an example, consider a single spherical bubble of diameter $D/10$ centered in a pipe of diameter D and length $10D$. The local void fraction in the centre of this bubble would be 1, the chordal void fraction along a line that is perpendicular to the axis of the pipe, and passes through the centre of the bubble would be 0.1, the cross-sectional void fraction across the centre of the bubble would be 0.01, and the volumetric void fraction would be roughly 0.00007.

It should be noted that the volumetric void fraction does not have the same definition as the thermodynamic vapour quality. The volumetric void fraction is a ratio of volumes, whereas the thermodynamic vapour quality is a ratio of masses.

In multiphase flows through channels, the superficial velocity of the liquid or gas, symbolized as j_l and j_g, respectively, is the ratio between the volume flow rate of that particular phase, Q_l or Q_g, and the cross-sectional area of the channel A_{cs}, namely

$$j_l = Q_l / A_{cs} \tag{4}$$

$$j_g = Q_g / A_{cs} \tag{5}$$

The total superficial velocity j is defined as the sum of the liquid and gas superficial velocities, i.e., as

$$j = j_l + j_g \tag{6}$$

Note that the superficial velocities are hypothetical velocities and do not correspond to any observable velocity within the flow.

In gas-liquid flows in which gas is contained in bubbles surrounded by liquid (or partially by solid walls), the interfacial velocity $\mathcal{U}$ may be defined as the average streamwise velocity of the interface between the bubble and the liquid. In cases for which the bubble maintains its shape and size as it is transported, the interfacial velocity and the average velocity of the gas contained in the bubble would be the same. However, an air bubble can deform, rotate, expand or contract and even break down or coalesce with other bubbles; in such cases, the interfacial and gas velocities could be different.

2.2 Gas-liquid flow regimes

Flow regimes in horizontal gas-liquid flows have been extensively researched in the past, especially in the fields of convective boiling and condensation. Unlike in vertical flow, there is typically a large asymmetry in the phases of the flow along the pipe due to the effect of gravity applied on each phase. The lighter phase (commonly either air or steam) naturally tends to coalesce at the top of the channel unless the driving force within the flow largely exceeds the buoyancy force.

Figure 4 shows different horizontal flow patterns corresponding to different flow regimes. On the left side, a sketch of each pattern is shown next to a photograph shown on the right-hand side. The characteristics flow patterns in each regime are as follows (Thome, 2004).

- In bubbly flow, the gas bubbles are dispersed with a higher concentration in the upper half of the channel due to buoyancy.
- In plug flow (also known as elongated bubble flow), the gas bubbles are not dispersed but coalesce together into relatively few large elongated bubbles. Their diameter is smaller than the tube's, and the liquid below them is continuous. Buoyancy forces are dominant, and the elongated bubbles travel near the top of the channel.

- In stratified flow, the two phases are completely separated by an undisturbed interface, with the gas and liquid occupying the upper and lower regions of the channel respectively.
- In stratified-wavy flow, the two phases are separated, but the interface becomes disturbed by waves at a frequency that depends on the relative velocities of the phases. The crests of the waves do not reach the top of the channel, but climb up the sides of the tube, leaving a thin liquid film on the tube's side as they fall back.
- In slug flow the crest of the waves reach the top of the channel, separating the gas into distinct elongated bubbles.
- In annular flow, the liquid forms a continuous annular film around the pipe's perimeter, while the gas flows within the core. In horizontal flow, the liquid film near the bottom of the pipe is in most cases significantly thicker than the liquid film at the top. The interface between the liquid and gas is wavy and disturbed.
- Misty-annular flow is very similar to annular flow, but in this regime the liquid is stripped from the wall forming small droplets, which become entrained in the gas in the pipe's core.

In view of the previous definition of the interfacial velocity, which requires the presence of a clear, discernible interface between the liquid and the gas, it is noted that the interfacial velocity can be measured unambiguously in the bubbly, plug and slug flow regimes, in which liquid and gas alternately pass through a probe. However, in stratified and annular flow regimes, the interface is nearly parallel to the axis of the pipe, and the probe would likely detect waves or other disturbances on the surface of the interface. Care must therefore be taken when interpreting interfacial velocity measurements, as they may not always represent the average gas velocity.

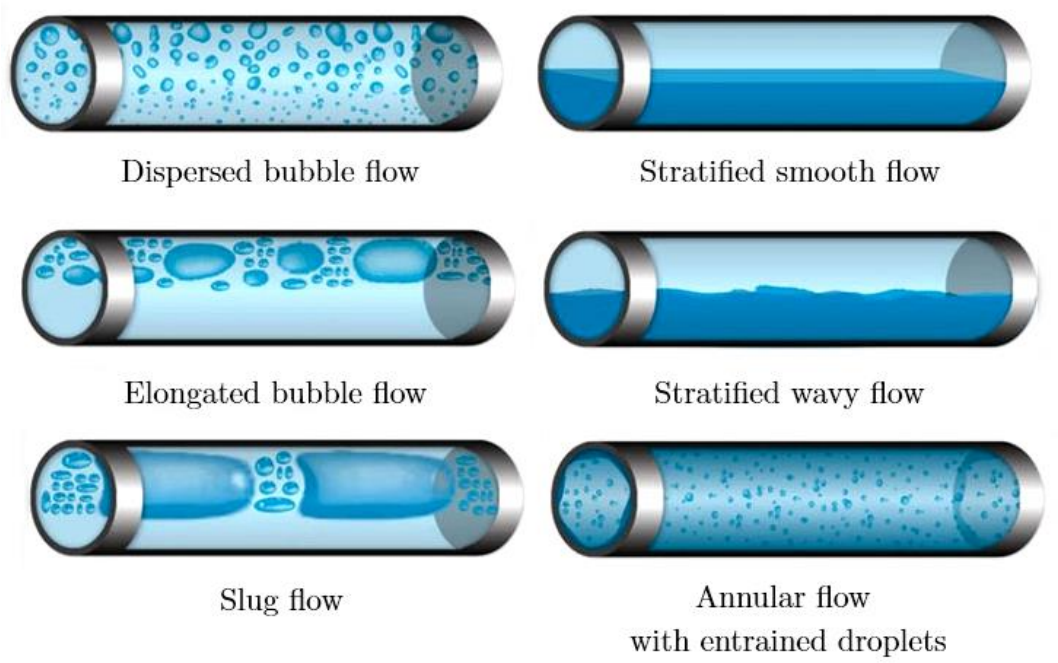

Figure 4: Horizontal gas-liquid flow patterns (from www.drbratland.com)

In two-phase flows in which boiling (evaporation) and/or condensation occur along the pipe, several or even all of these flow patterns may be observed at some location along the pipe, as shown in Figure 5. In Figure 5a, evaporation occurs, and the cross-sectional void fraction increases as the flow travels to the right. In Figure 5b, the steam condenses and the void fraction decreases along the pipe. In Figure 5c, the steam condenses but the average flow velocity is relatively low, resulting in stratified phases rather than distinct large bubbles (slug and plug flow).

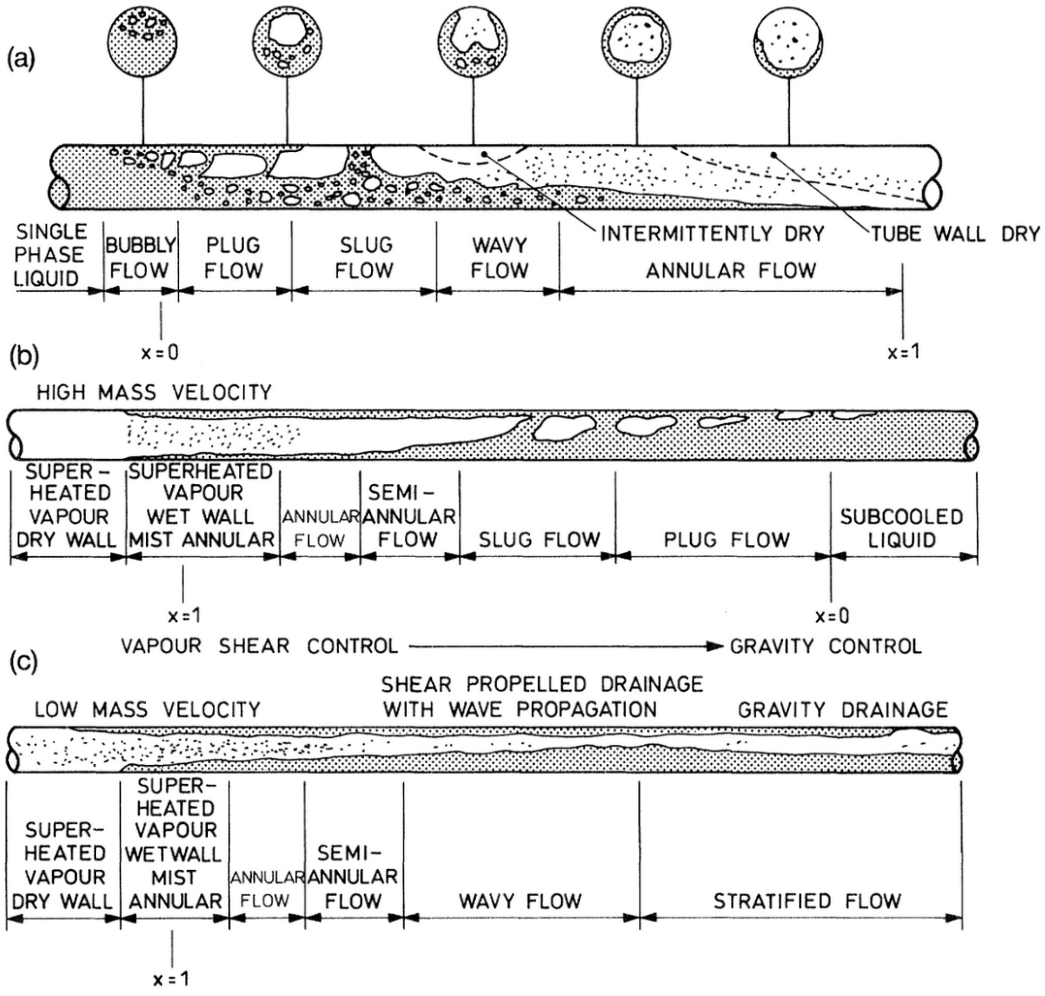

Figure 5: Two-phase horizontal flow patterns with a) evaporation; b) condensation (high flow rate); c) condensation (low flow rate) (Collier, 1994)

2.3 Flow regime map

A common approach for classifying the regimes in two-phase flows is to present flow regime maps, plotted in axes showing the mass fluxes or the superficial velocities of the liquid and gas. Other flow parameters, such as pipe diameter, temperature and pressure are maintained constant for a given flow regime map. In fact, it has been shown that the effect of pipe diameter on the flow regime is negligible for pipe diameters larger than 25 mm (1 in) (Mandhane et al., 1974).

Figure 6 illustrates the flow regime map for horizontal flow presented by Baker in 1954 (Collier, 1994). The vertical axis represents the air's mass flux G_g and the horizontal axis represents the water's mass flux G_l. Note that the regimes were identified by qualitative observation. The boundaries between these regimes are not sharp, as there are transitional regimes separating them.

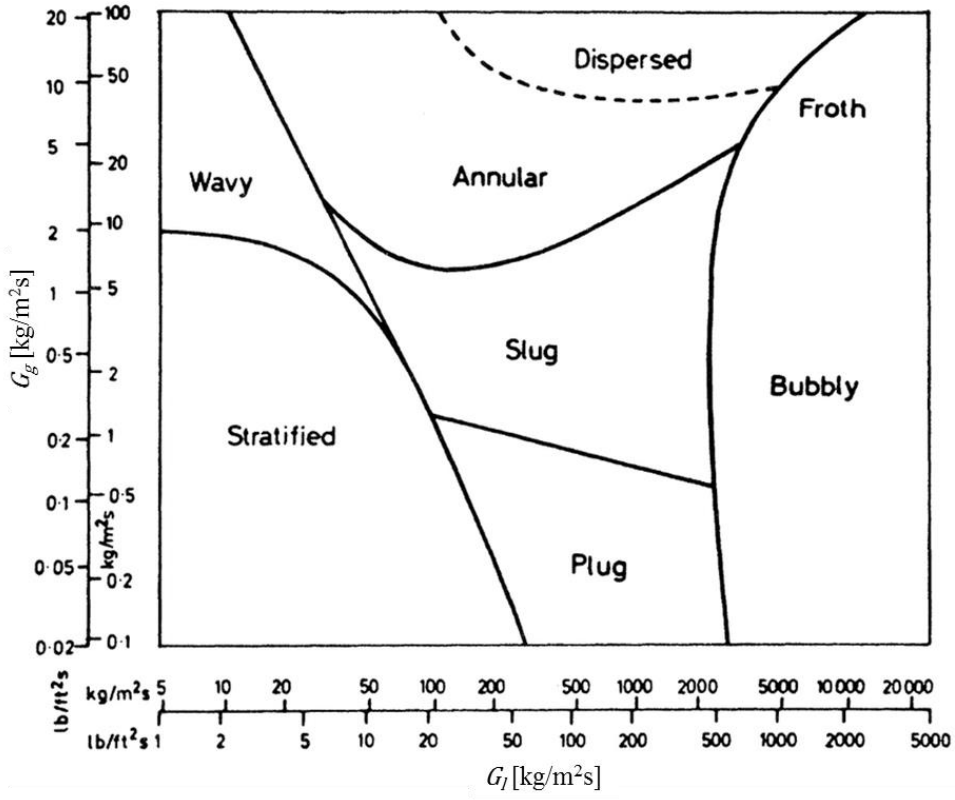

Figure 6: Horizontal pipe flow regime map by Baker (Collier, 1994)

Mandhane et al. (1974) proposed a revised flow pattern map, based upon the observations previously collected in the University of Calgary's Multiphase Pipe Flow Data Bank, and compared these results to those by other researchers, including Baker. Mandhane favoured the use of plots in axes on the superficial velocities of the liquid j_l and the gas j_g, as these proved to discriminate among regimes in a more consistent fashion. The resulting flow regime correlation has shown better agreement with the 1178 experimental data sets that were analyzed than any other correlation previously proposed.

For example, for air-water flows, the average agreement of the flow regimes to those in the Mandhane map was 81.8%, whereas Baker's map only produced a 61.3% agreement. A plot of the Mandhane map is shown in Figure 7; this includes grey borders indicating the areas where transitional regimes were observed.

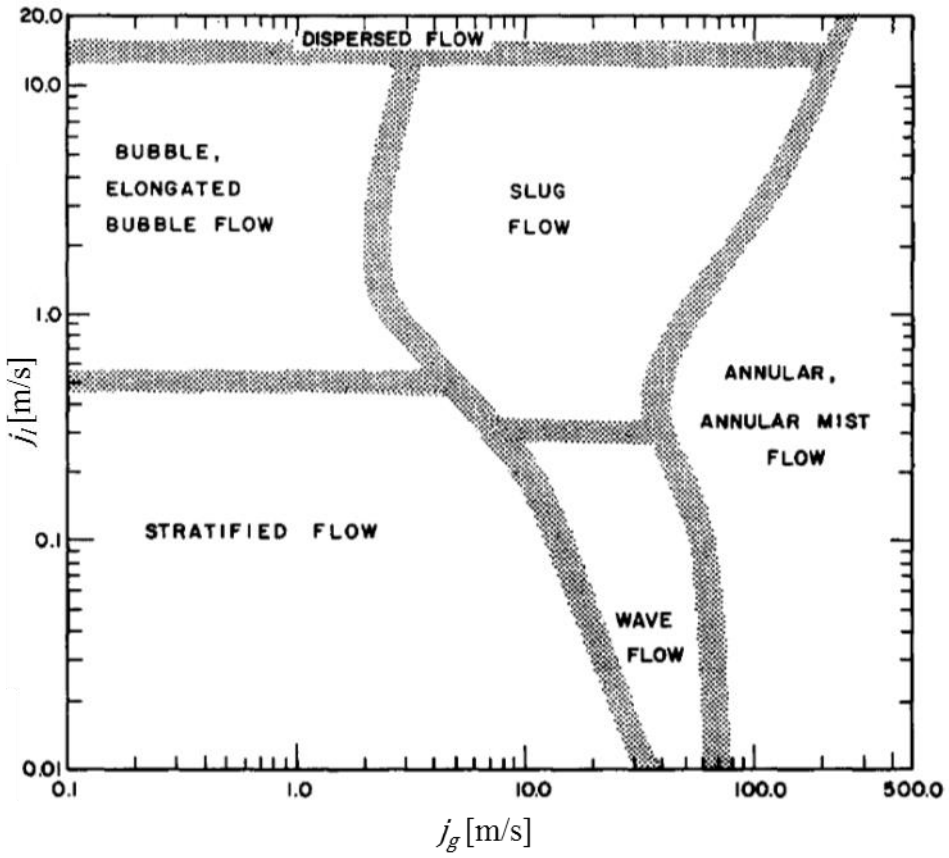

Figure 7: Horizontal pipe flow regime map (Mandhane et al., 1974)

2.4 Drift-flux models

The use of drift-flux models is a simplified approach to the study of two-phase flows. These models consider the fluid mixture as a whole rather than two separate phases. This technique has been proven to be useful in many engineering applications.

The void fraction may not be simply obtained from the ratio of the gas and total volumetric flow rates, nor from the ratio of the gas and total superficial velocities. The non-uniformities of the velocity and void fraction distributions and the slip between the

two phases are the main sources of complexity to the prediction and measurement of void fraction. The drift-flux model was first developed to account empirically for these effects (Zuber and Findlay, 1965).

The drift-flux model expresses the void fraction in terms of the gas superficial velocity j_g and the total superficial velocity j as

$$\varepsilon = \frac{j_g}{c_0\, j + v_{gj}} \tag{7}$$

where c_0 and v_{gj} are empirical parameters, referred to as the distribution parameter and the slip velocity, respectively. c_0 is a correction factor that accounts for the velocity and void concentration non-uniformities across the channel, which may vary independently of one another. v_{gj} represents the difference between the gas and liquid velocities; it is proportional to the volumetric flow rate at which gas passes through a plane moving with the mixture at the total superficial velocity j.

The model proposed by França and Lahey (França and Lahey, 1992) has been developed from a set of two hundred air-water data points in horizontal pipe flow. The test section had an inner diameter of 19 mm, preceded by a development section 187 diameters long. The resulting drift flux parameters derived from these experiments are summarized in Table 1.

Table 1: Drift-flux model parameters for horizontal pipe flow (França and Lahey, 1992)

Flow Regime	c_0	v_{gj} **[m/s]**
Plug	≈ 1.0	0.16
Slug	≈ 1.2	- 0.20
Wavy-Stratified and Annular	≈ 1.0	from 0.2 (j_l = 0.005 m/s) to 2.7 (j_l = 0.27 m/s)

2.5 Void fraction measurement techniques

The quick-closing valve method is one of the most common techniques for void fraction measurement. It requires a set of quick-closing valves, one at each end of the test section. They are triggered simultaneously, isolating the test section from the rest of the loop, while the flow is redirected through a bypass branch. From the known volume of the test section and the measured liquid volume drained, the void fraction can be determined. Despite its accuracy, the main drawback of this technique lies in the repeated sudden interruption of the flow, which may be problematic in some systems.

Electrical conductivity methods, including the WMS method described in more details below, require the insertion of electrodes within the flow to measure the local electrical conductivity. The electrical conductivity of a two-phase mixture is a function of void fraction and phase distribution. The large difference between the electrical conductivity and permittivity of the two phases is exploited to measure void fraction and obtain flow regime characteristics.

Other techniques for void fraction measurements include sampling methods, thermal methods such as hot-film anemometers, optical methods, acoustical methods and radiation methods (Tavoularis, 2005).

2.6 WMS principles of operation

The WMS used in this study is the WMS200 model manufactured by Teletronic Rossendorf (Teletronic, 2009). This device is described below.

2.6.1 Wire-mesh sensors

A description of the original wire-mesh sensor and its operation has been provided by the team that developed it (Prasser et al., 1998). Various modifications and improvements have been made during the following years, including an increase of its data acquisition rate by an order of magnitude, up to 10 kHz (Prasser et al., 2000), so that the WMS can be used in flows with higher velocities or smaller gas particle sizes. A representative WMS is shown in Figure 8. It consists of two grids of parallel wires (electrodes), perpendicular to each other and to the flow direction.

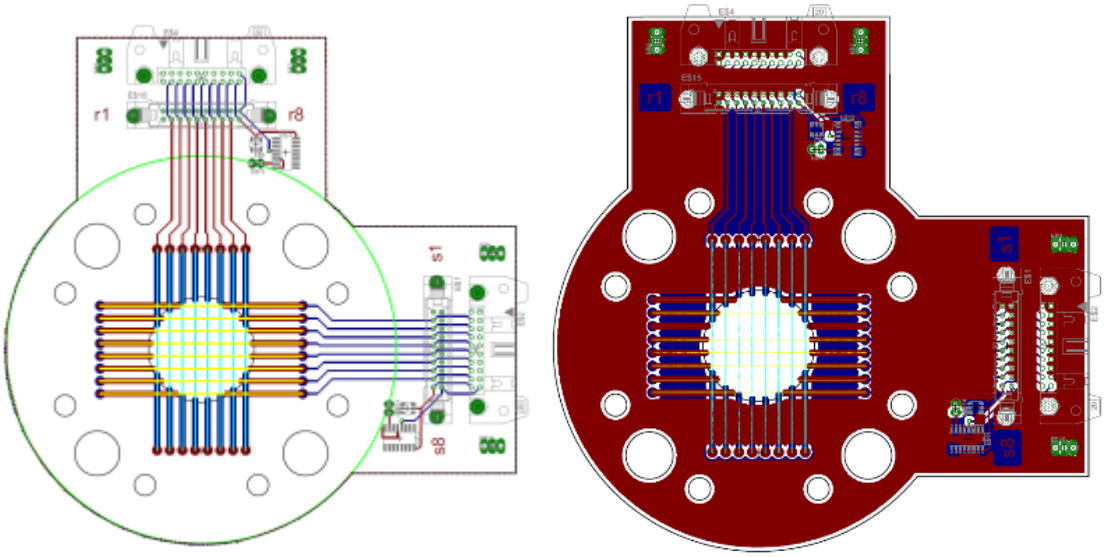

Figure 8: Schematics of an 8x8 wire-mesh sensor (Yang, 2013)

Each grid is positioned on a separate plane and the two planes are separated stream-wise by a short distance of roughly 2 mm. This device measures the local instantaneous conductivity of the flowing mixture at the nodes of the mesh formed by the

two grids. An electronic control system sends electric current pulses sequentially through each of the electrodes of the upstream grid and a data acquisition system with a multiplexer measures the electric potential differences between each pair of perpendicular wires in the two grids. At nodes at which air occupies some or all of the space between the two wires, the conductivity of the material between the two wires would be lower than that of water and so the gas phase would be detected at that node. The phase detection at all nodes is completed at a rate of 10 kHz, so that the output of the system would be essentially instantaneous phase maps in a cross section of the flow. The addition of a second WMS slightly downstream of the first one makes it possible to measure the convection speed of the interface between the two phases.

Wire-mesh sensors are constructed in various shapes and sizes to accommodate the channels within which they are designed to operate. They are made in circular shapes for studies of pipe flows, but they have also been constructed to fit in a rectangular frame. In all cases, the two arrays of electrodes are always perpendicular to each other. Therefore, a WMS with a circular frame may have some “dead” nodes near its corners where they would intersect outside of the area of interest. An area correction for each node is then required as part of the post-processing of the data collected to account for this (discussed in further details in the Procedures chapter). For example, Figure 9 illustrates a particularly large WMS, with 32 electrodes in each direction.

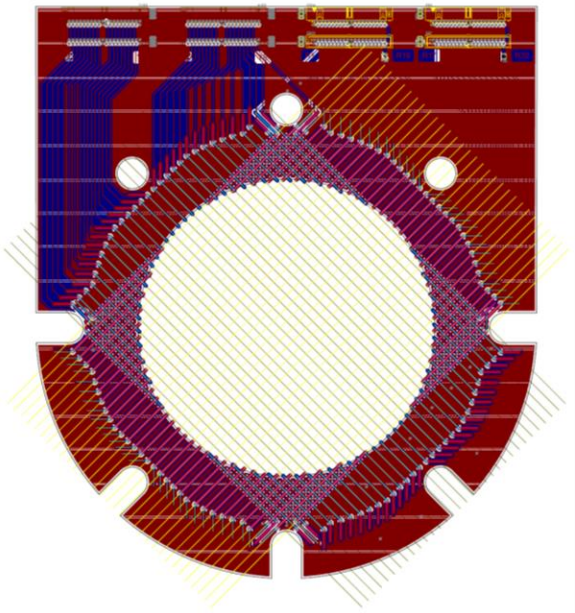

Figure 9: A 32x32 WMS of 203mm I.D. (Yang, 2013)

2.6.2 Measurement principle

The mechanism by which the WMS provides flow measurements is based on the electrical conductivity of the fluid flowing through the grid. Current pulses with an amplitude of ± 70 mA are applied sequentially to the transmitter wires of different nodes. Each node is defined as the intersection of the projections of two wires that are perpendicular to each other and separated axially by a short distance. When a transmitter wire is triggered, a measurement will be taken at the corresponding perpendicular receiver wire. The current arriving at the receiver wire is transformed into voltages by operational amplifiers (Prasser et al., 2010). This measured voltage is then amplified by a default amplitude factor of 255; manual adjustments are possible to slightly change this gain value in order to optimize the measurements' range. It is recommended by the manufacturer that the maximum output of any measurement point should be at most 90% of the maximum signal that can be captured by the sensor (Teletronic, 2010, p.24). Finally each signal is sampled by individual sample/hold circuits (Figure 10).

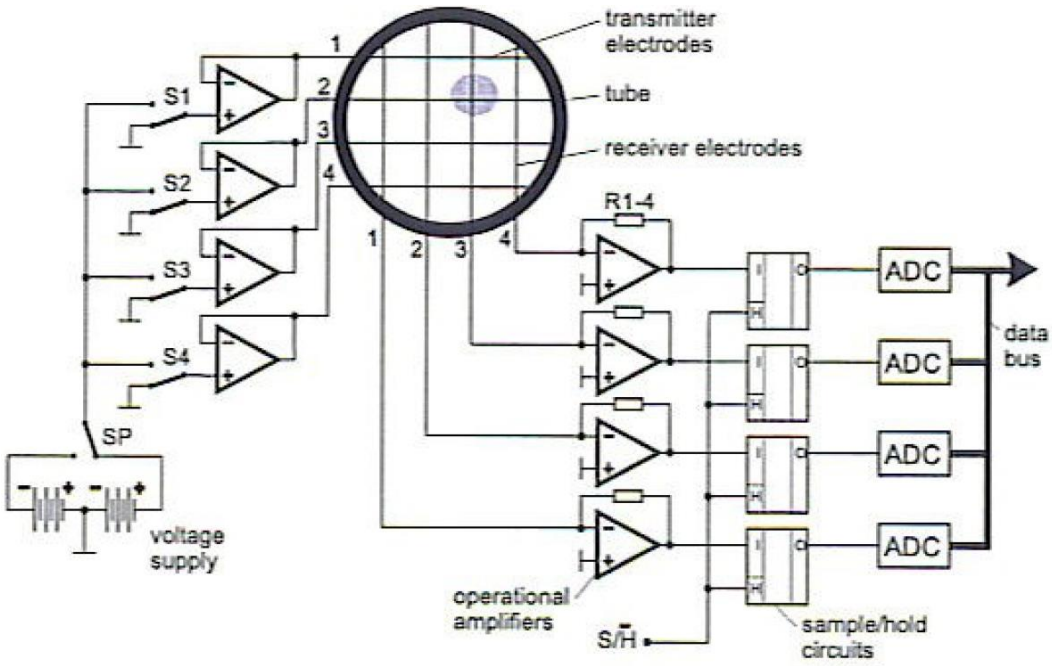

Figure 10: Simplified schematic diagram of a WMS signal acquisition system (Prasser et al., 2000)

The voltage signal is then converted from analog to digital and recorded. The WMS transfers the signals it measures to a PC computer by means of a transmitter and receiver circuit (Figure 11) connected to the signal acquisition system.

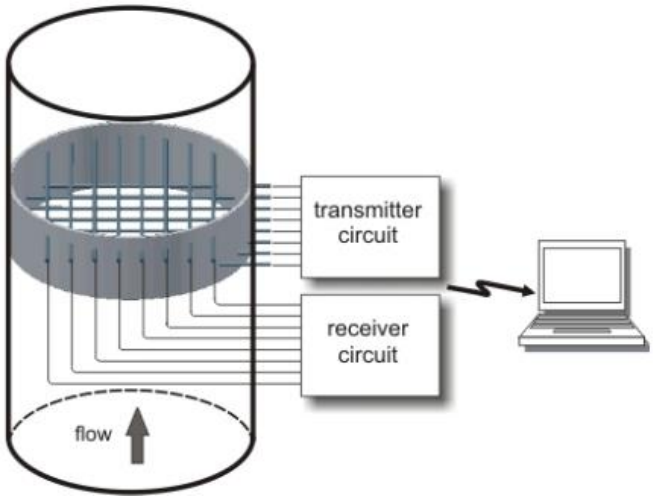

Figure 11: Circuit connecting a WMS and a PC (from www.hzdr.de)

The process is then repeated for each of the other nodes. Figure 12 provides a visual example of the process for a 5×5 WMS (note that this was different from the 8×8 WMS used in this study), and the resulting cross-sectional electrical conductivity map displayed by the software. On the top left, a simplified diagram shows a representative air bubble crossing the 5×5 grid, while on the right is the corresponding digital grid provided by the WMS software. A sample cycle will be presented. When a pulse is applied on the transmitter wire C, wire 1 triggers a measurement of the voltage at node C1, which is then converted through the analog-to-digital circuit to provide a high voltage measurement (shown in dark blue on the right). Wire 2, whose intersection with wire C is located near the air bubble interface, triggers next, while the transmitter wire is still C, and provides a low voltage displayed in light blue at node C2. The node C3, located inside the air bubble, will display a very low voltage as the air entirely surrounding it acts as an electric insulator, and therefore is displayed as almost white on the right plot. A similar procedure is repeated for the wires 4 and 5. The current is then applied on the next transmitter wire (D in this case), until each transmitter wire has been triggered for every receiver wire, hence completing the cycle and providing a digital "frame" of the voltage distribution as shown on the right.

As each node is fired one after the other, their measurements for a single frame are not simultaneous, but, because the measurement frequency is so high and the flow velocity in most water flow loops is relatively low, they can be approximated as instantaneous. It is also noteworthy to point out that the resulting digital frame shown on the right is not void fraction but voltage. The procedures to extract void fraction from these measurement will be explained later in section 4.4.

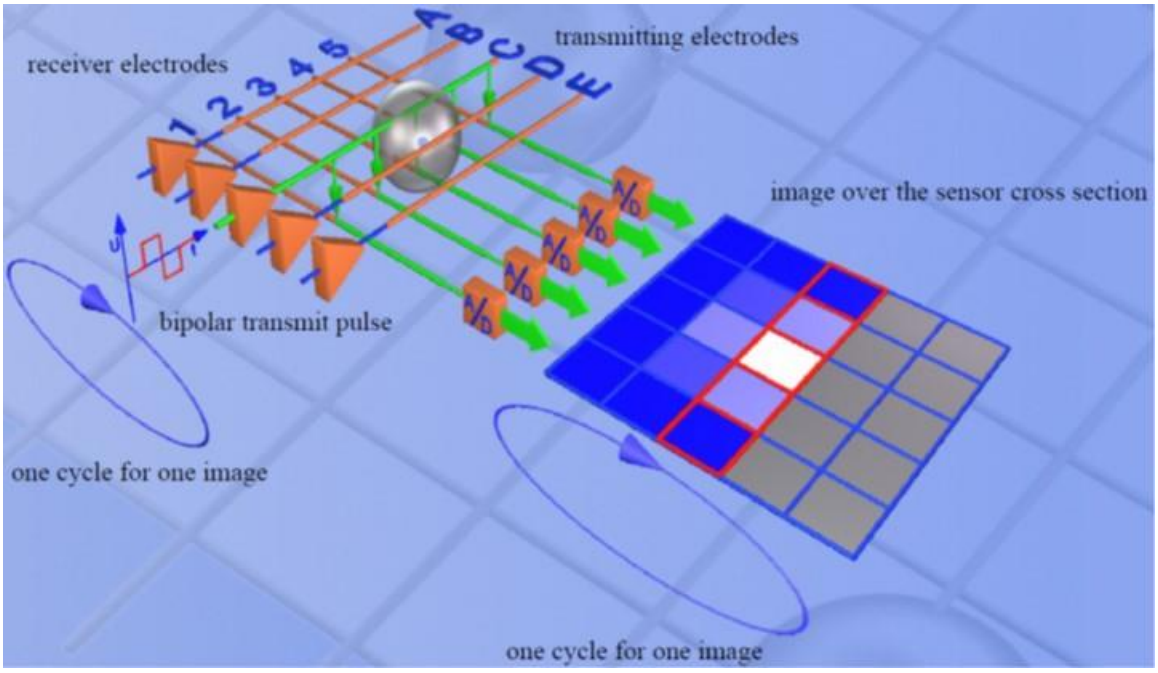

Figure 12: WMS principle of operation (Teletronic, 2008)

2.6.3 Applications

This section outlines some previous work of relevance that was performed with WMS. The WMS has previously been used for bubble size measurement in a rectangular channel (Prasser et al., 2001a). They used a 16×16 WMS with a 51.2 mm I.D. and recorded the flow appearance with a high-speed camera. The wire pitch was 3.12 mm, the distance between the two planes of electrodes of the sensor was 1.50 mm, and the wire diameter was 0.12 mm. This study first focused closely on the effects of the wire on the bubbles crossing the sensor. Figure 13 illustrates a bubble moving upwards towards a single WMS, whose lower plane of electrodes has wires with axes normal to the page, and its upper plane of electrodes has wires with axes parallel to the page. The study has shown that the bubbles are first segmented into slices by the first array of wires, and then further segmented perpendicularly by the second array of wires, resulting in a cloud of small bubbles. Despite the fact that the small fragments tend to recombine, the bubble is disturbed significantly by the sensor.

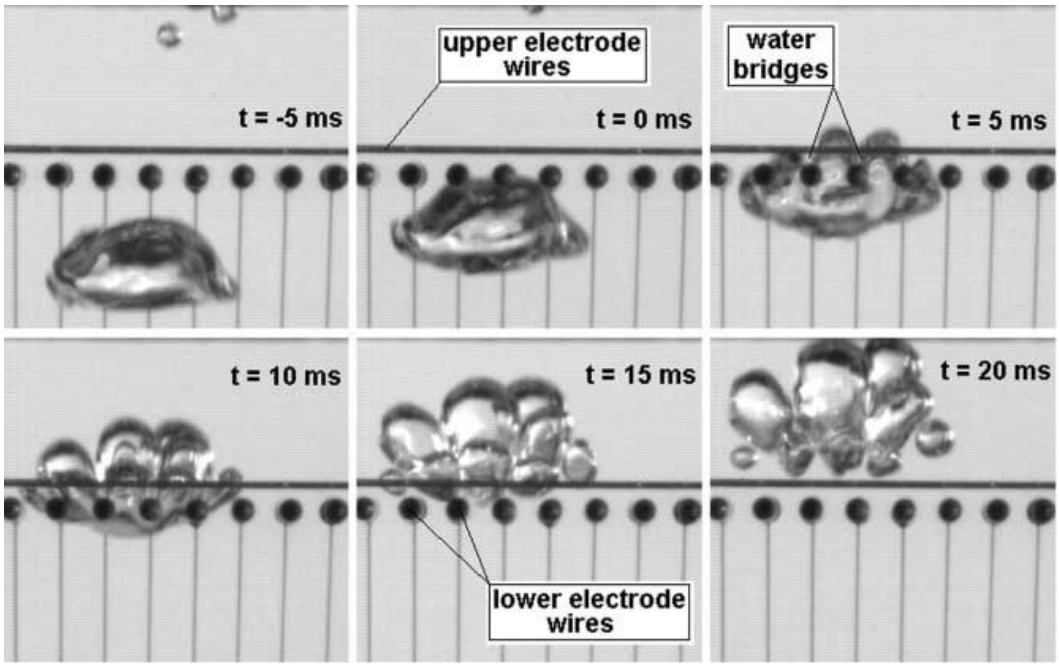

Figure 13: Bubble fragmentation across a WMS (Prasser et al., 2001a)

High–speed snapshots of the side view of the test section were compared to the corresponding frames measured by the WMS (Figure 14). It is of interest to note that the breakdown of the bubbles across the wires cannot be detected by the WMS.

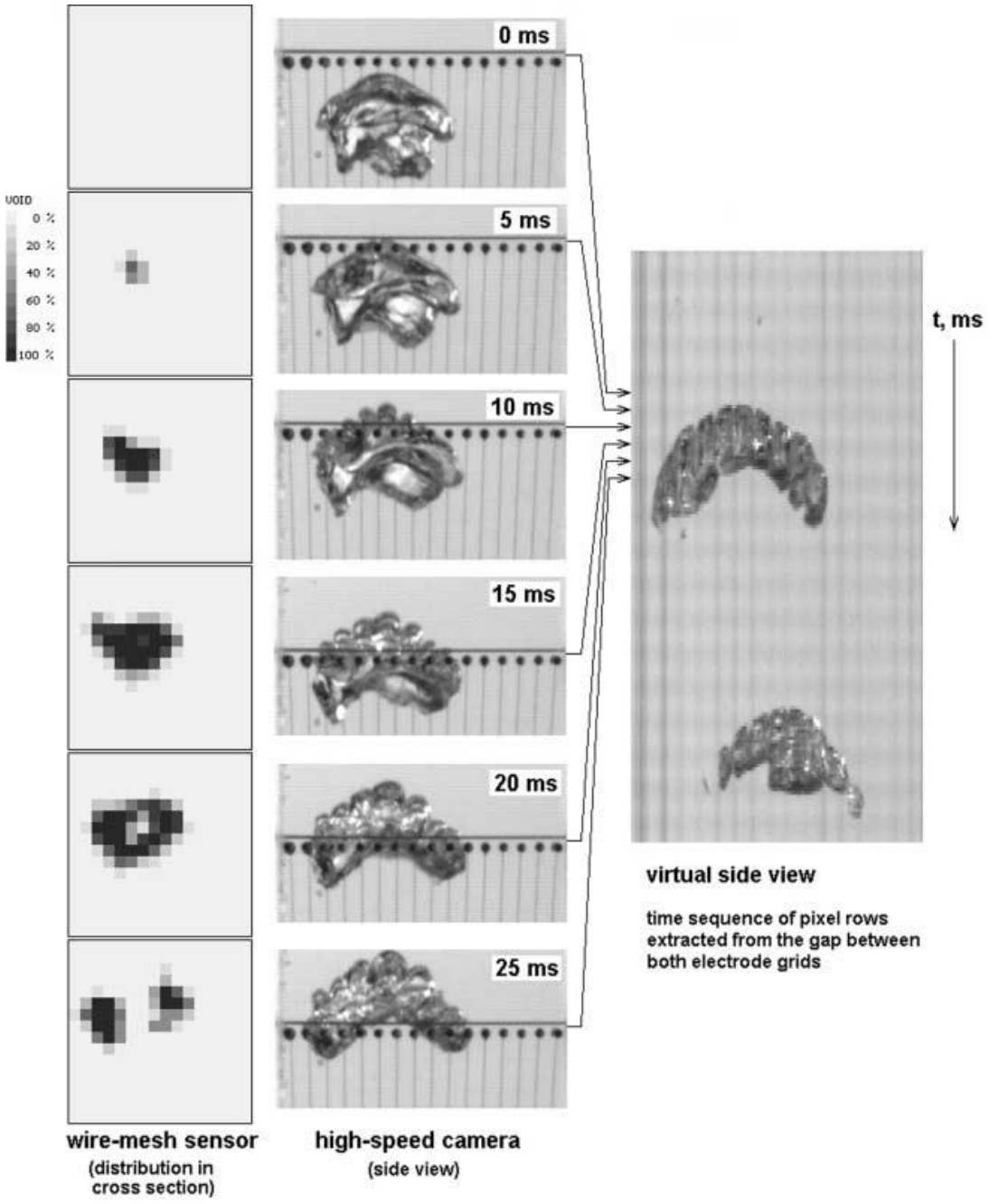

Figure 14: WMS signal and corresponding side view snapshots (Prasser et al., 2001a)

In another study, the WMS has been tested under high pressure and temperature environments (Pietruske and Prasser, 2007). Two high resolution WMS were used, a 52.3 mm I.D. 16×16 sensor, and a 195 mm I.D. 64×64 sensor, operated at up to pressures of 7

MPa and temperatures of 286 °C in a 9 m long vertical pipe. This project aimed at observing scaling effects based on temperature and pressure and at the qualitative effects of these parameters. Some results of some virtual side projections and section views under various pressures are shown in Figure 15 (j_l=1 m/s, j_g≈ 0.84 m/s, D= 195.3 mm).

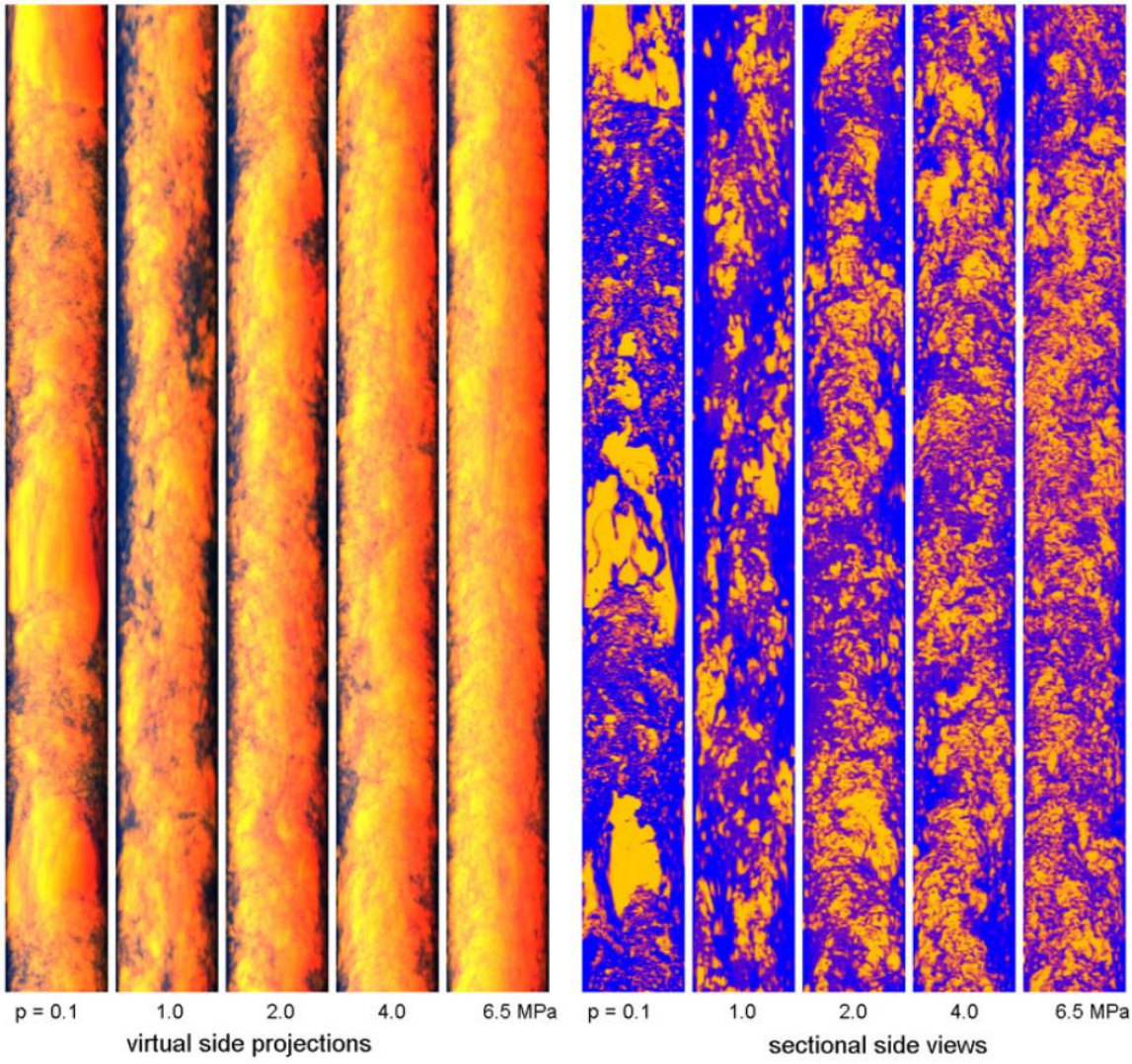

Figure 15: Flow visualization of WMS data (Pietruske and Prasser, 2007)

The two-phase flow void fraction measurements of the WMS were compared to gamma densitometry measurements (Sharaf et al., 2011). A single 16×16 WMS was used in a 50 mm I.D. pipe, for high spatial resolution. The void fraction measured in the central part of the pipe with both instruments produced results in agreement within ±10%.

However, measurements taken near the pipe walls showed significant discrepancies, which were attributed to the limitations of the two measurement techniques. In Figure 16, the percentage differences between the gamma densitometry and WMS results are presented for twelve different combinations of two superficial liquid velocities (0.2 m/s and 0.7 m/s) and six superficial gas velocities (from 0.05 m/s to 1.4 m/s). Positions 1 and 16 correspond to nodes of the WMS located near the wall of the pipe, while positions 5 and 12 are located near the core of the pipe.

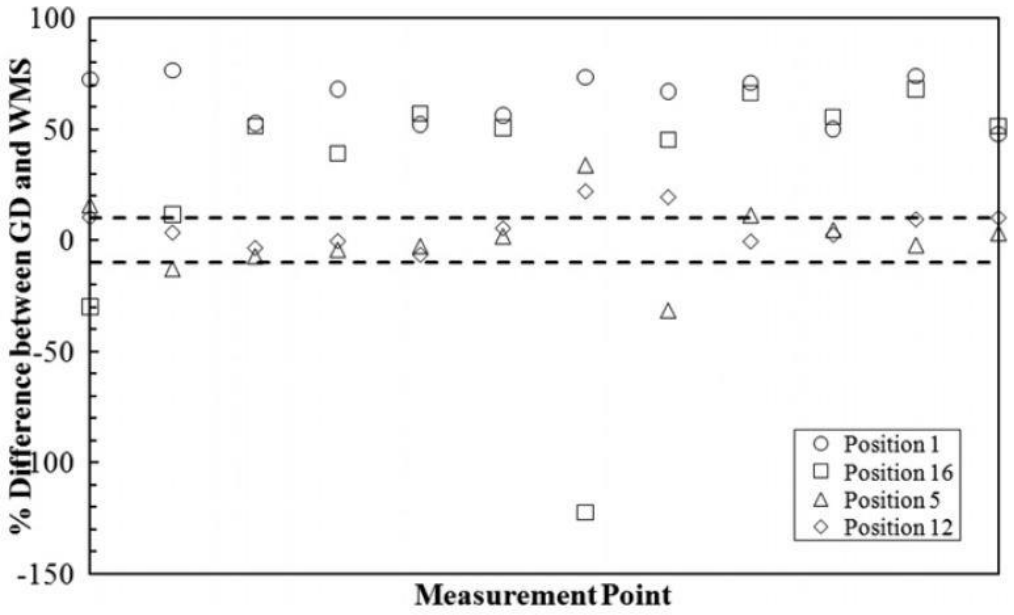

Figure 16: Percentage difference between void fraction values measured by gamma densitometry and WMS (Sharaf et al., 2011)

Chapter 3 Experimental facilities and instrumentation

This chapter provides an overview of the facility and equipment that were used for these experiments, and presents their main features and specifications.

3.1 Layout of the loop

The main dimensions and specifications of the air-water flow loop are presented in Table 2.

Table 2: Flow loop general specifications

Head tank height from test section	4.47 m
Test section I.D.	D = 31.75 mm (1.25 in)
Development section length	3.15 m (= 97 D)
Test section length	0.38 m (= 12 D)
Exit section length	0.44 m (= 14 D)
Containment tank volume	225 liters (60 US gal)
Water operating temperature	T = 22 ± 2 °C
Maximum water superficial velocity	$j_l \approx$ 3 m/s
Maximum air superficial velocity	$j_g \approx$ 15 m/s

A schematic diagram of the recirculating flow loop is shown in Figure 17. Water stored in the containment tank is first pumped to the head tank, located roughly 4.5 m above the test section.

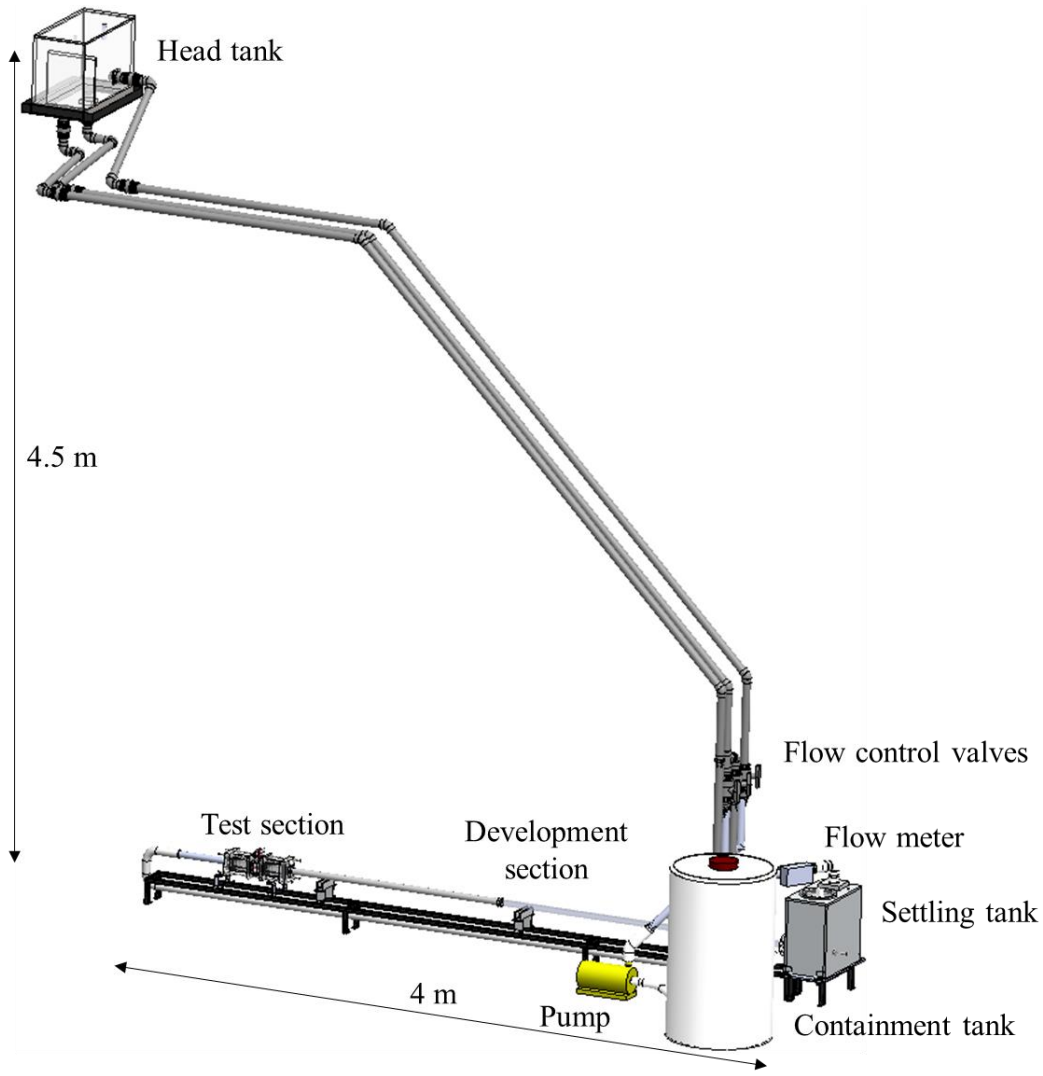

Figure 17: Recirculating flow loop

The head tank (Figure 18) is divided into two sections, separated by a dividing wall which acts as an overflow and maintains a constant head to the test section, whereas excess water is redirected back to the containment tank. The head tank also has both an air vent and a float switch, for safety purposes. Note that maximum superficial water velocity in the test section is limited by the height of the head tank and the pressure losses incurred throughout the loop due to friction.

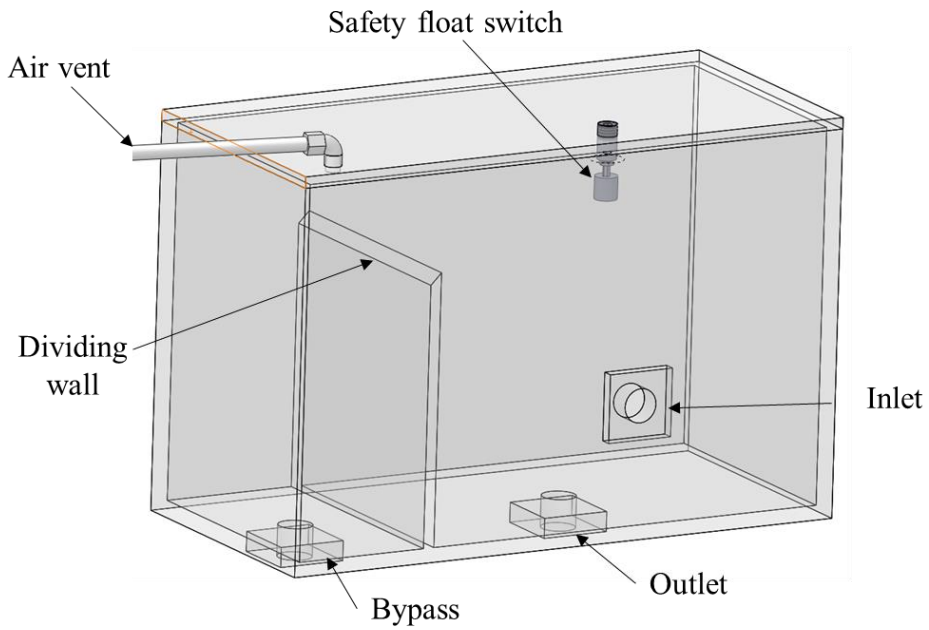

Figure 18: Head tank

The water that is not bypassed at the head tank flows back towards the settling tank. A pair of manual ball valves downstream of a junction allows the user to adjust the flow rate. One valve restricts the flow to the settling tank, while the other leads back to the containment tank.

A straight pipe section leading to the settling tank (Figure 19) includes an ultrasonic water flowmeter for liquid volume flow rate measurement (see Chapter 3.7.1). Once the settling tank is reached, any air that was entrained is evacuated through an air vent at the top of the tank. This procedure is only required during the start-up of the loop. The air injection port at the back of the settling tank leads to the nozzle centered at the pipe inlet on the other side of the tank.

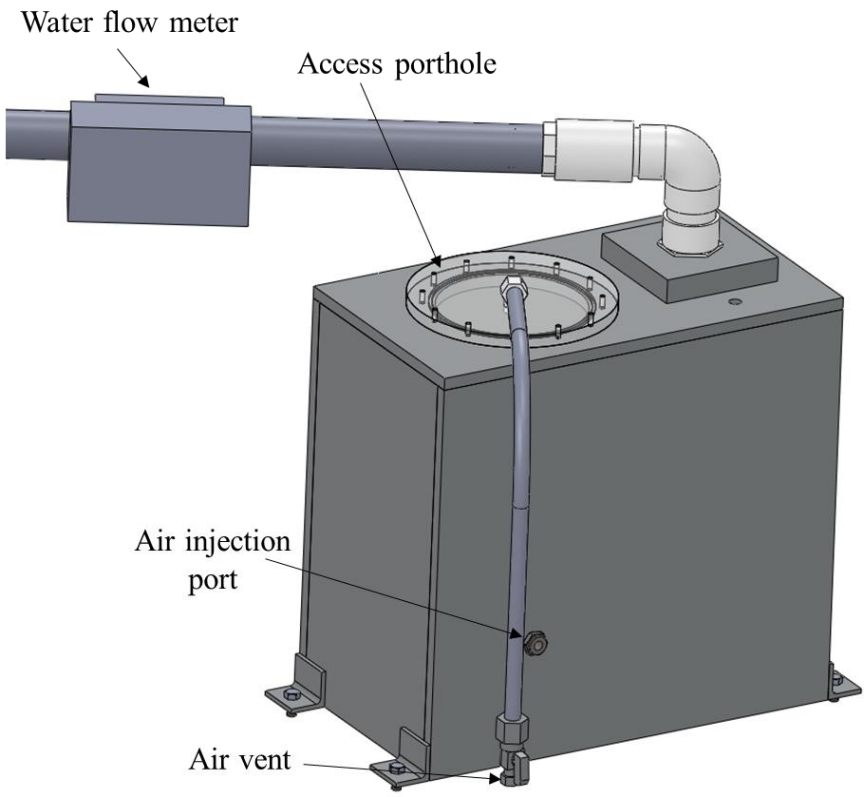

Figure 19: Settling tank (back view)

Water enters the development section upstream of the test section, following mixing with compressed air injected just downstream of the test section inlet. The air volumetric flow rate is measured by a rotameter. After the test section, the water is looped back towards the containment tank, where the cycle repeats. The water and air flow rates are controlled separately to allow the generation of different two-phase flow regimes, including bubbly, slug and annular flows as well as transitional regimes.

3.2 Air injection

Features of the flow that can be captured by the WMS greatly depend on the relative size of the bubbles or air slugs with respect to the grid spacing of the sensors. A custom injector nozzle has been designed, which has three rows of holes on its sides, all spaced by 60°, to provide a dispersed and uniformly distributed air injection at the inlet

of the development section. It should be noted that bubbles of small diameter, namely of diameter smaller than the wire spacing of the WMS, are expected to take a path of least hindrance as they travel through the sensors and slip between the nodes without being recorded by the sensor. This is an inherent limitation of the device that can only be improved by a tighter grid spacing.

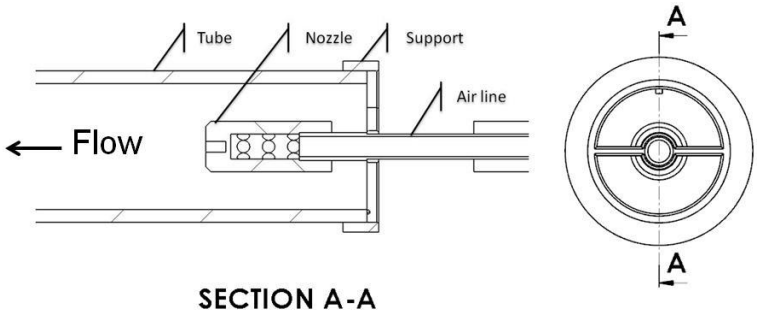

Figure 20: Air injector assembly cross-section (left) and axial profile (right)

Additional illustrations of the nozzle and its assembly can be found in the Appendix.

3.3 Wire-mesh sensor

Two identical wire-mesh sensors were used. Their main specifications are as follows. Details on the WMS operation are covered in Chapter 0. The length Δx is the axial distance between the mid-electrode planes of the two sensors (Figure 21).

Table 3 Wire-mesh sensor specifications (Teletronic, 2009)

Manufacturer	Teletronic Rossendorf
Model	WMS200
Maximum operation temperature	180 °C
Maximum operation pressure	7 MPa

Wire diameter	0.24 ± 0.02 mm
Wire spacing (centre-to-centre)	S = 3.84 ± 0.04 mm
Measurement frequency	f_{meas}= 10 kHz
Inner diameter of sensor	31.9 ± 0.2 mm
Total cross-sectional area (neglecting wire intrusion)	A_{cs}= 8.0 ± 0.1 × 10^{-4} m^2
Cross-sectional area (considering wire intrusion)	7.5 ± 0.1 × 10^{-4} m^2
Cross-sectional area decrease due to wire intrusion	6.3 %
Axial distance between the two measurement planes	Δx= 22.7 ± 0.3 mm
Liquid electrical conductivity range	0.01 to 1000 µS/cm
Transmitting pulse voltage	± 3 V
Maximum transmitting pulse current	± 70 mA
Transmitting pulse timing (short)	~ 6 µs

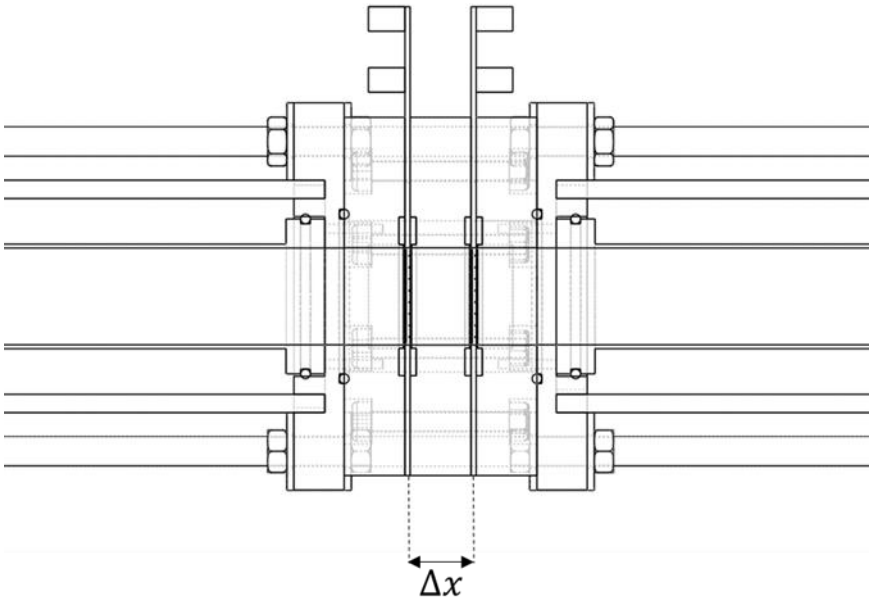

Figure 21: Axial distance between the WMS electrode mid-planes

3.4 Ancillary equipment

The master card of the basic device controls the communication with the PC over a USB 2.0 connection. The WMS multiplexer system housed within the basic device (Figure 22) has been upgraded over the last years (Prasser et al., 2000), the most notable upgrade to the device being the maximum measurement frequency having been increased from 1,200 frames per second to 10,000 frames per second.

Figure 22: WMS 200 basic device (Teletronic, 2010)

The transmitter module (Figure 23) serves as a link between the basic device's master card and the WMS. The receiver module (Figure 23) includes a pre-amplifier, a main amplifier, an analog-to-digital converter and a control unit. It also houses a 255 step potentiometer for manual output gain adjustments.

Figure 23: Transmitter (left) and receiver (right) units (Teletronic, 2010)

3.5 PC software and user interface

In order to visualize the data collected in real-time and adjust various parameters for the operation of the WMS, a basic software named WMS 200 v1.4.12.0 was used. It provides a user interface as shown in Figure 24. The main features of this software include gain adjustments for the output voltage, real-time flow visualization, measurement frequency settings, measurement duration adjustments and basic statistical analysis of the signal at any node. The output files of this software are ".mes" files, which must then be processed by the program WMS-Data-Converter.

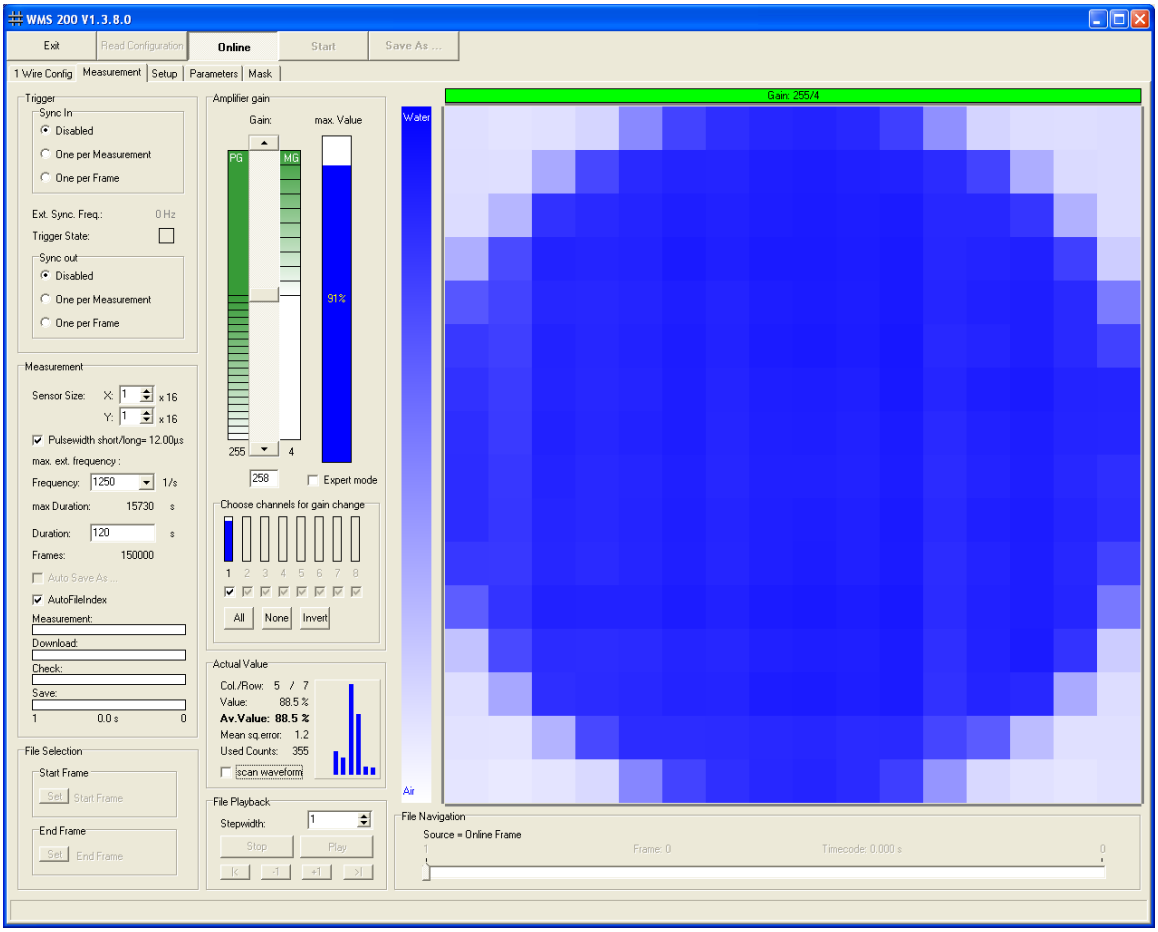

Figure 24: WMS200 main screen (Teletronic, 2010)

WMS-Data-Converter 4.10.0.0 allows the export of ".mes" files into decoded ".dat" files, which can then be imported and read by the programming code. It also allows either type of files to be visualized with playback functions, with adjustable speeds. It is important to note that the data contained in these files do not correspond to void fraction or any other flow property, but are proportional to the measured voltage at these nodes. Further processing is required to extract flow properties from this information (WMS signal post-processing on page 44).

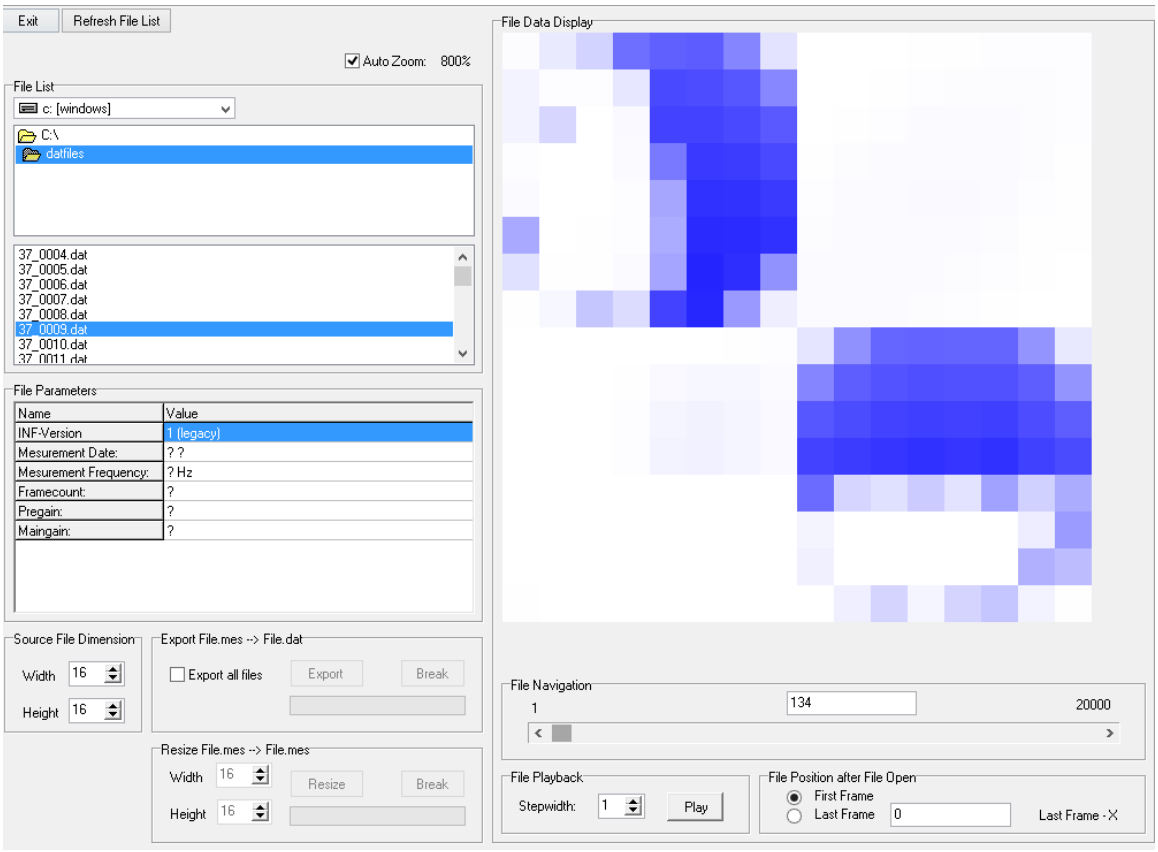

Figure 25: WMS data converter main screen

3.6 Test section

The WMS are installed in the test section of the flow loop. They are shown in red in Figure 26. The test section is not only designed to be supporting the sensors, but also as a location of undistorted optical access for high-speed photography purposes upstream and downstream of the sensors.

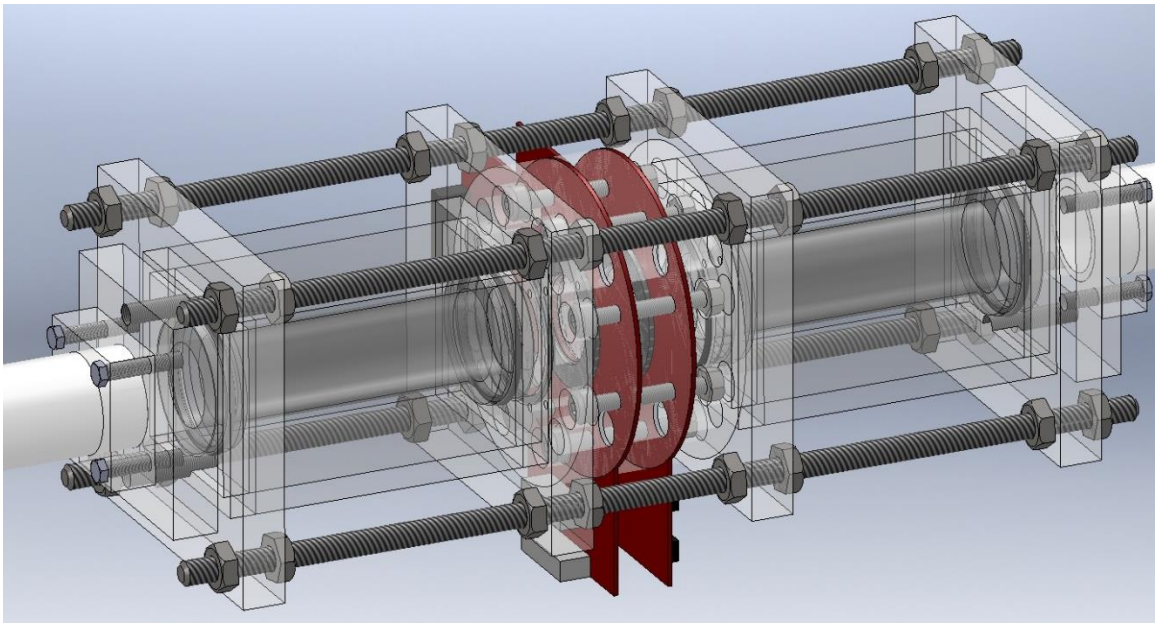

Figure 26: Test section

Figure 27 illustrates the cross-section of the test section. This section is positioned downstream of a long pipe (1), which allows full development of the air-water flow. The central piece is a pair of WMS (2) mounted on a special flange (3). On either side of this assembly, there are two short pipe sections (4) with 0.7 mm thick walls made of fluorinated ethylene propylene (FEP, known under the trade name Teflon), having a refractive index that closely matches that of water, thus allowing undistorted optical access. These sections are immersed in square viewing tanks with glass walls (5) and containing still water (6).

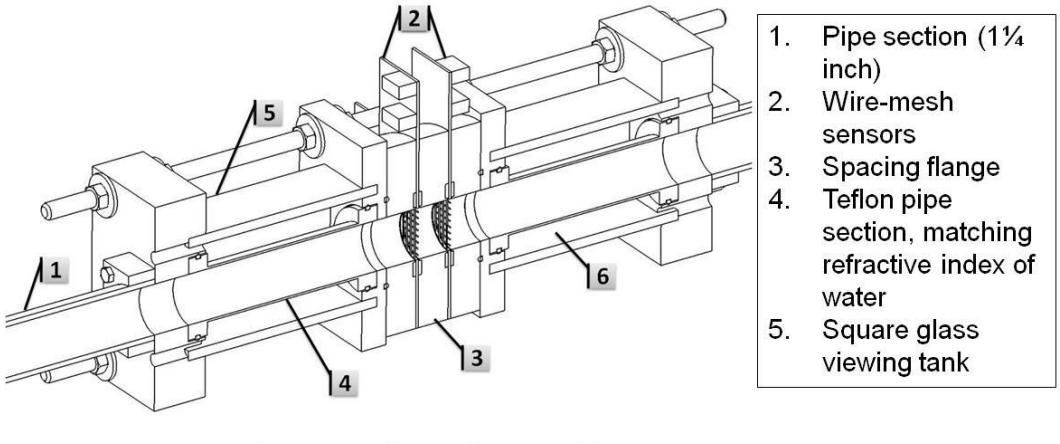

Figure 27: Cross-section view of the test section and its main components

The Teflon pipe section becomes almost transparent when immersed in water, although it is opaque in air. A business card, placed behind the viewing tank in Figure 28, illustrates how effectively light passes through the pipe section under normal lighting conditions.

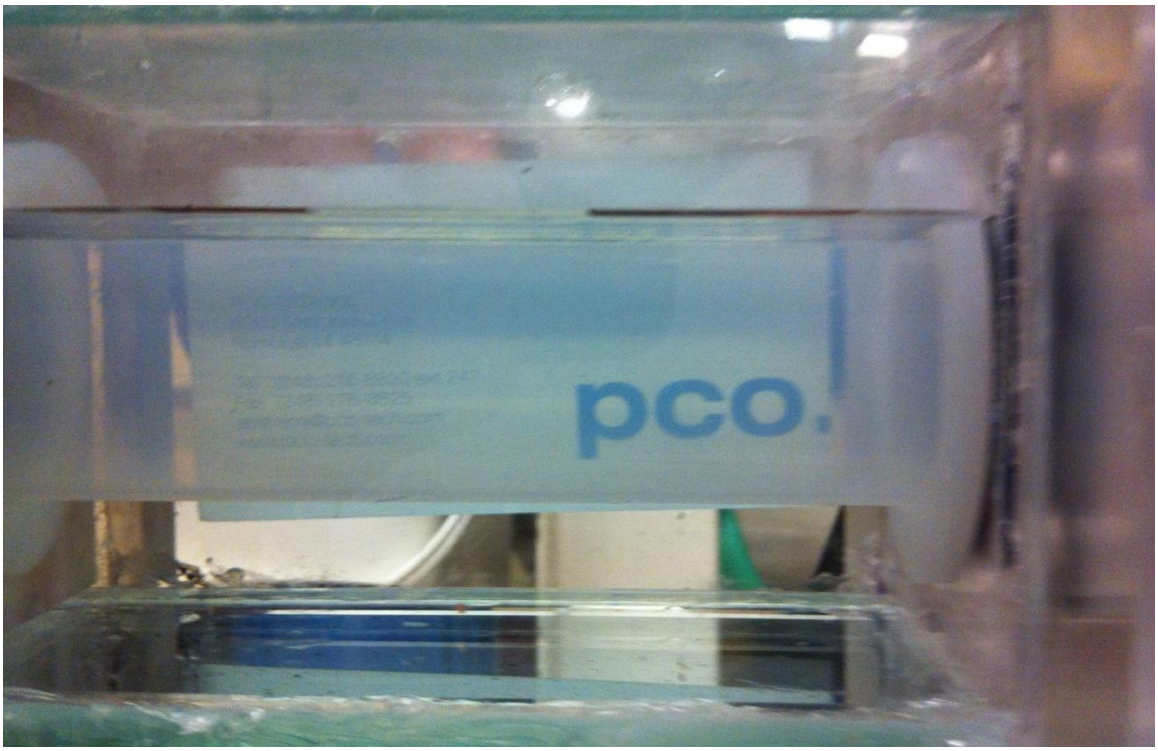

Figure 28: Undistorted view of a business card through the Teflon pipe section

3.7 Flowmeters

3.7.1 Ultrasonic water flowmeter

A transit time ultrasonic flowmeter (FDT-33, Omega Canada) was used for water volume flow rate measurement. This flowmeter had sufficient accuracy within the entire flow rate range of the loop. By comparison to rotameters, this ultrasonic flowmeter introduced a much lower obstruction to the flow, as it only required a pipe contraction from 38.1 mm (1.5 in) I.D. in schedule 40 to 25.4 mm (1 in) I.D. in schedule 40, and so permitted the loop to operate at higher flow rates. The procedure for the calibration of this flowmeter has been described in Appendix A.

Figure 29: Time-transit ultrasonic water flowmeter (Omega Canada)

Table 4: Water flowmeter specifications

Supplier	Omega Canada
Model	Series FDT-33-T
Accuracy	± 1 % above 0.3 m/s
Volume flow rate range	0.000126 to 0.00631 m^3/s
Plastic pipe inner diameter at flowmeter location	25.4 mm (1 in) in SCH 40
Repeatability	± 0.5 %
Velocity range	0.03 to 12.4 m/s

3.7.2 Air rotameter

A rotameter (Series 7510, King Instrument Company, Garden Grove, USA) was used for air volumetric air flow rate measurements (Figure 30). The main specifications of the rotameter are summarized in Table 5. The procedure for the calibration of the air flowmeter has been described in Appendix A.

Figure 30: Air rotameter (King Instrument Company)

Table 5: Air rotameter specifications

Supplier	King Instruments
Distributor	McMaster-Carr
Model	Series 7510
Accuracy	± 3% of full scale
Volume flow rate range (standard conditions)	0.00038 to 0.0039 m^3/s

3.8 High-speed photography

Figure 31: High-speed camera (PCO, 2011)

For interfacial velocity measurements, a high-speed camera (PCO.edge, PCO-Tech Inc., Romulus, USA) was used as a standard to which the WMS interfacial velocity would be compared. The main specifications of the instrumentation used for this purpose is found in Table 6.

Table 6: High-speed camera specifications (PCO, 2011)

Model	PCO.edge
Maximum resolution	2560x2160 pixels
Frame rate (variable depending on resolution)	100 frames/second @ 2560x2160 893 frames/second @ 320x240
Shutter modes	Rolling and global (snapshot)
Lens	Nikon Nikkor 50 mm f/1.4D AF

Chapter 4 Measurement procedures and accuracies

This chapter summarizes the mathematical procedures that were used to determine the void fraction and gas velocity from the WMS signals. These were based on and adapted from those suggested by the sensor manufacturer.

4.1 WMS signal acquisition

For each set of measurements, corresponding to specified air and water flow rates, the recorded WMS signals consisted of a three-dimensional matrix with height $N_i = 8$, width $N_j = 8$ and variable depth N_k. The height and width correspond to the number of rows and columns of wires, respectively, on each array of the sensor, and the depth corresponds to the number of successive recorded frames. Each data set consisted of 50,000 or 100,000 frames per sensor, sampled at a rate of 10,000 frames/s over a time interval of 5 or 10 s, respectively. The reported values of local void fraction $\varepsilon_{i,j,k}$ correspond to node i,j and frame k, whereas ε_k would be the cross-sectional void fraction at frame k, and ε would be the volumetric void fraction.

The data sets of the WMS were collected as follows. A given water flow rate was set, and a calibration file was recorded for time-averaged calibration purposes (more details of this procedure will be presented in a following section). Then the air injection valve was opened, in order to allow a sparse trickle of air bubbles (sparse bubbly flow pattern), for high-speed photography velocity measurement comparisons. A recording was once again taken, and the flow pattern observed was recorded for each set.

While the water flow rate was kept constant, the air flow rate was raised stepwise from a value corresponding to the lowest reading of the air rotameter to one corresponding to the highest reading, or the maximum attainable in the system. WMS data and the observed flow pattern were recorded. The air was then shut off, the water flow rate was changed to another value, and the procedure was repeated.

During these measurements, the flow was observed by the user through the transparent pipe section. The flow regime, identified according to the characteristic flow patterns that were explained in Chapter 2.2, was noted, together with the measured gas and liquid volume flow rates.

The output of the WMS consists of encrypted files. Each "frame" of a single sensor is represented by an 8×8 data matrix, in which each node contains a 12-bit digitised output voltage signal, corresponding to the voltage recorded at a node multiplied by a constant gain. For example, a measurement of 1 s duration, containing the data of both sensors, would be composed of 1.28 million distinct data points.

4.2 Area weight coefficient

To calculate cross-sectional averages, one assumes that the measured value at each node of the WMS is the average value over the surrounding portion of the cross-sectional area, which depends on the location of the node. To account for differences in areas surrounding each node, the measurements are weighted by area weight coefficients before averaging (Prasser et al., 2001b). The area weight coefficient $a_{i,j}$ at a node i,j is defined as the ratio of the area around the node and the total cross-sectional area A_{cs} of the sensor. Figure 32 shows a quadrant of the pipe's cross-section, with superposed wires shown in black, and identifies the areas surrounding each node that are used for calculating the weight coefficients. One may distinguish three types of nodes: a) inner nodes, b) near-border nodes, which are adjacent to the border of the pipe, and c) corner nodes, which are outside the pipe and whose signal is disregarded in the analysis. The part of the area surrounding corner nodes is assigned to the closest border node.

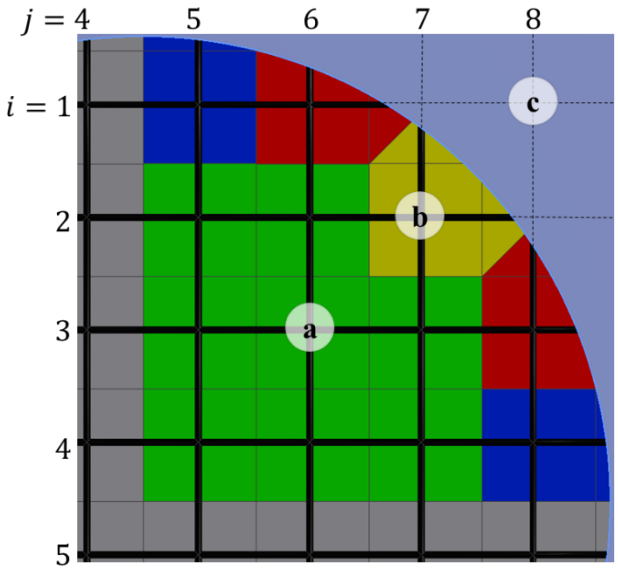

Figure 32: Examples of a) inner node, b) near-border node, c) corner node for one quadrant of the WMS

All inner nodes are assigned an area weight coefficient $a_{inner\ node}$ that is equal to the ratio of the mesh area, found from the wire spacing S, and the total cross-sectional area of the tube as

$$a_{inner\ node} = \frac{S^2}{A_{cs}} = 0.0186 \tag{8}$$

The weight coefficients of near-border nodes could be larger or smaller than those of inner nodes, whereas the weight coefficients of corner nodes are equal to zero. Table 7 lists the area weight coefficient values corresponding to the nodes located in the top right quadrant of the sensor. The area weight coefficients of all nodes are shown in Figure 32.

Table 7: Area weight coefficients for nodes in the top right quadrant of a sensor

		i			
		5	**6**	**7**	**8**
j	**1**	0.0204	0.0183	0	0
	2	0.0186	0.0186	0.0237	0
	3	0.0186	0.0186	0.0186	0.0183
	4	0.0186	0.0186	0.0186	0.0204

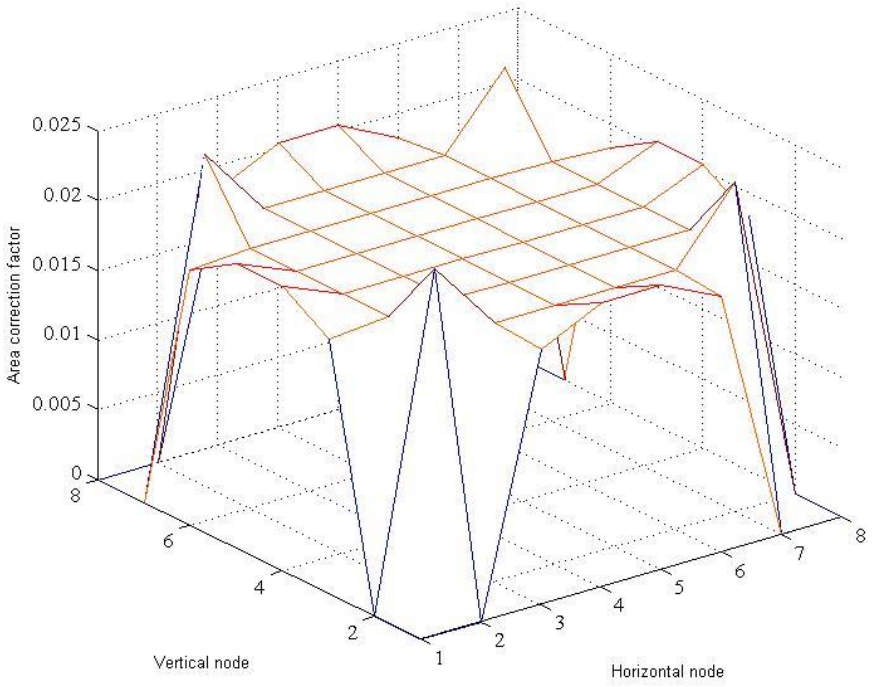

Figure 33: Area weight coefficients

The cross-section-averaged void fraction ε_k for a particular frame k was computed as

$$\varepsilon_k = \sum_i \sum_j a_{i,j} \varepsilon_{i,j,k} \tag{9}$$

4.3 WMS signal post-processing

A computer program was developed to process the WMS data (Appendix B). It is composed of several steps, which are summarized below in order of appearance within the code.

1. Memory purge and initialization of constants
2. Importing of .dat file of the measurement file

3. Data filtering of the measurement file (discarding of the corner nodes) and orientation correction of the sensors (required to account for their back-to-back installation in the test section, as shown in Figure 26)
4. Importing of .dat file of the calibration file
5. Data filtering of the calibration file following the same procedures as step 3
6. Time-average calibration
7. Histogram calibration
8. Instantaneous void fraction calculation
9. Average void fraction calculation
10. Average interfacial velocity calculation
11. Individual interface velocity calculation
12. Exporting and saving of results

4.4 Void fraction calculation

The output signal of the WMS is a digitised voltage signal. In order to express this information in terms of volumetric void fraction, some calibration procedure must first be performed.

Two methods of calibration are possible, and each has its own advantages and disadvantages. These are the time-average calibration procedure and the histogram calibration procedure. Both techniques were used when analyzing the data, and in the majority of cases both produced essentially identical results. A breakdown of the time-average void fraction for each data set and each sensor based on both calibration methods can be found in Appendix D.

Time-average calibration requires that a calibration measurement file be taken in full liquid at some time prior to or following the air-water measurement. The shorter the temporal shift between these measurements is, the more accurate the measurement would be, since the conductivity of the fluid might change over time due to the temperature variations in the fluid caused by the pump. The instantaneous volumetric void fraction

$\varepsilon_{i,j,k}$ at any given node i,j and frame k is calculated from the voltage signal $V_{ij,k}$ during measurement and the voltage signal V_l during calibration in water, as

$$\varepsilon_{i,j,k} = 1 - V_{i,j,k}/V_l \tag{10}$$

The calibration voltage V_l is found by time-averaging the voltage signal at each node. It is worth noting that it is important to record each node separately to account for possible variations of the sensitivity of each node.

Histogram calibration requires a histogram of the frequency of occurrence for the voltage signal of every node of each sensor. Histogram calibration is preferable in most cases except for high void fraction flows. Its greatest advantage is that it does not require a separate calibration measurement (which would be taken at a different time), but can be conducted using the measurement itself. Figure 34 shows a sample node histogram during a water flow and an air-water flow. In the former case, a single peak is found, with all data lying close to the average voltage signal. In the latter case, two distinct peaks are clearly distinguishable and are largely spaced out; they indicate the values that occur most often, which correspond to pure gas (left peak, low voltage) and pure liquid (right peak, high voltage). Any values located in-between are caused by small bubbles remaining attached to the wire, inherent measurement uncertainty of the apparatus, or signal noise. To perform the histogram calibration, the voltage V_l corresponding to the high peak is found. Again, note that it is important to record each node separately. The void fraction can then be found following equation (10).

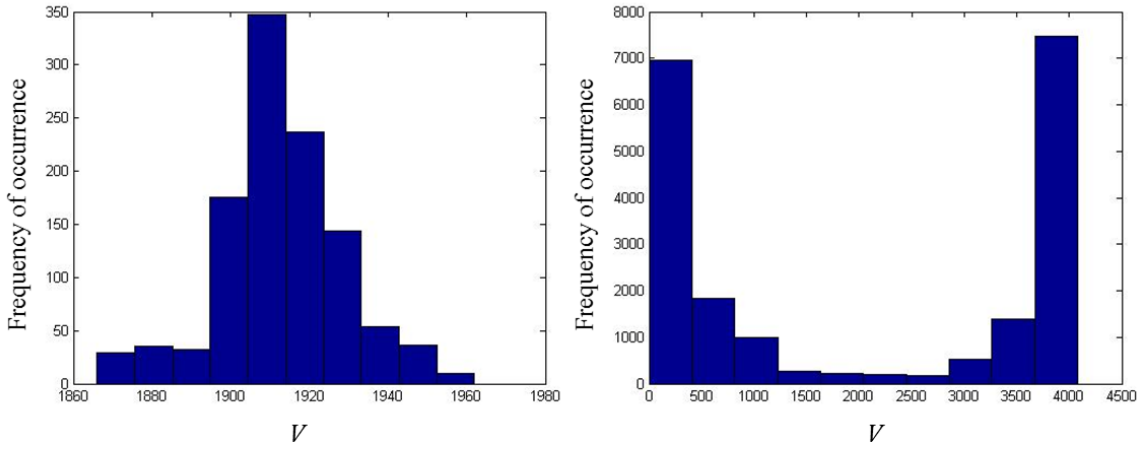

Figure 34: Histogram calibration typical signals for pure water (left) and water-air (right) flows

4.5 Interfacial velocity measurement

The interfacial velocity $\mathcal{U}$ of gas bubbles within a liquid flow is determined from the signals of two WMS, one downstream of the other, where the measurement plane of one sensor is separated from the other's by a distance Δx = 22.7 mm. If one determines the time Δt it takes the air-water interface to travel the distance Δx between the two WMS, the interfacial velocity can be found as

$$\mathcal{U} = \Delta x/\Delta t \tag{11}$$

Figure 35 shows the simultaneous signals of corresponding nodes of two WMS and the corresponding histograms of the frequency of occurrence of the signals. By comparing visually the signals of the two sensors, it is possible to see that they can be made to collapse approximately on each other by shifting one of them by a number of frames Δk_s. The time shift Δt_s it took the interface to travel the distance between the two WMS can be found as

$$\Delta t_s = \Delta k_s/f_{meas} \tag{12}$$

where $f_{meas}$is the sampling frequency. Considering that the signal within an air bubble is essentially zero, the number of frames over which the signal is low is proportional to the

length of the bubble that crossed that particular node of the sensor. However, calculating Δt by visual comparisons of the signals is impractical and so an automated procedure, developed by the sensor manufacturer, was applied instead. This procedure is outlined in the following paragraphs.

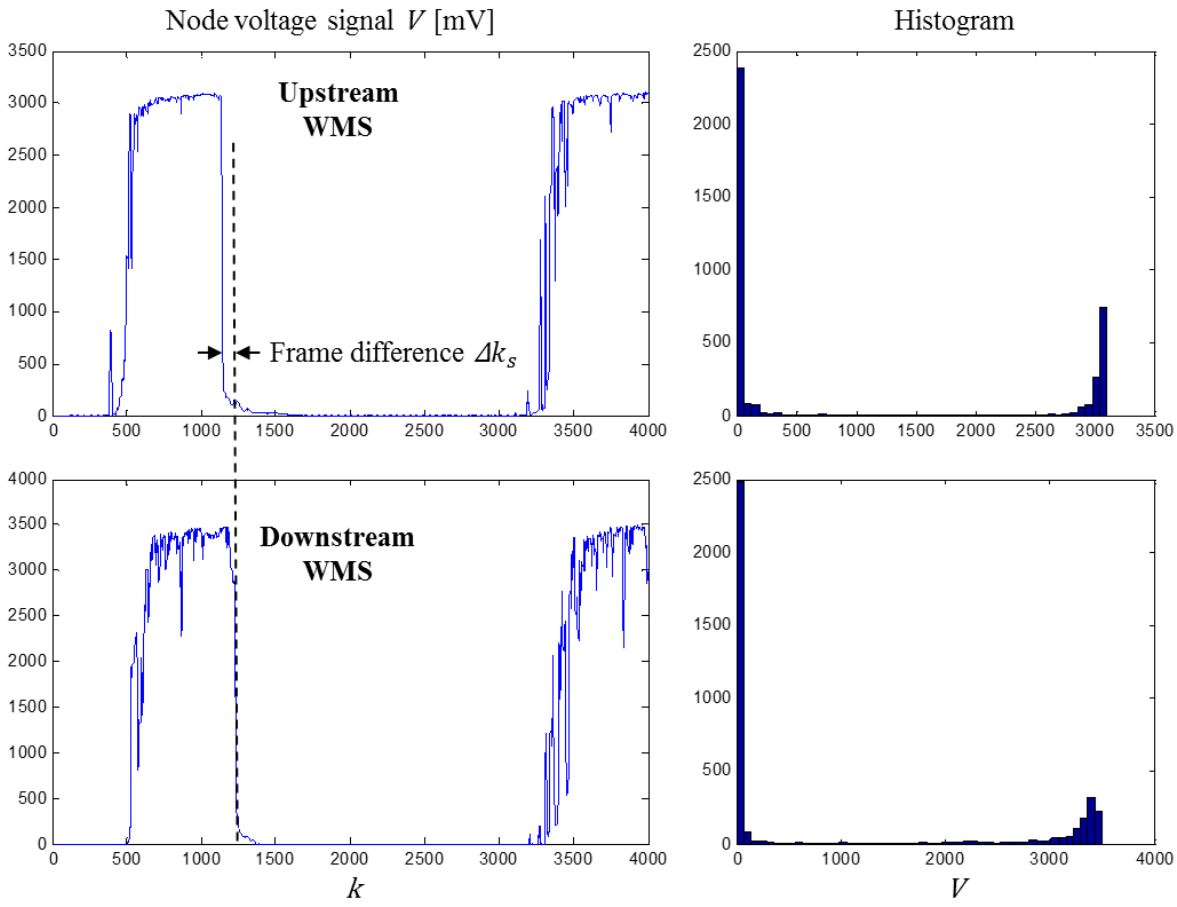

Figure 35: Representative signals (left) of corresponding nodes of two WMS in an air-water flow and their histograms (right)

The time-averaged void fraction $\overline{\varepsilon}_{i,j}$ at each node of each sensor is first calculated as

$$\overline{\varepsilon}_{i,j} = \frac{1}{K}\sum_{k=1}^{K} \varepsilon_{i,j,k} \tag{13}$$

Then, the mean-free fluctuation of the void fraction is determined as

$$\varepsilon'_{i,j,k} = \varepsilon_{i,j,k} - \overline{\varepsilon}_{i,j}\,, \qquad k = 1,2,\dots,K \tag{14}$$

The cross-correlation coefficient F_{i,j,dk_s} for a frame shift Δk_s is then calculated from the fluctuation components of the upstream (subscript 1) and downstream (subscript 2) sensors as

$$F_{i,j,\Delta k_s} = \frac{\sum_k^{K-\Delta k_s} \varepsilon'_{1,i,j,k}\varepsilon'_{2,i,j,k+\Delta k_s}}{\sqrt{\sum_k^K \varepsilon'^2_{1,i,j,k}}\sqrt{\sum_k^K \varepsilon'^2_{2,i,j,k}}} \tag{15}$$

The cross-correlation coefficient $F_{i,j,\Delta k_s}$ can be interpreted as the level at which two signals from corresponding nodes (i.e., nodes facing each other in the streamwise direction) would coincide when the downstream signal is shifted back by Δk_s frames. A cross-correlation coefficient of 1 (or 100%) would represent a perfect signal match.

The variations of $F_{i,j,\Delta k_s}$ for all 52 in-flow nodes of a sensor have been plotted against the frame difference Δk_s in Figure 36 for a representative case. The smooth lines in the plot correspond to nodes which were crossed by both air and water, while the oscillating lines (which also have much lower correlation levels) typically correspond to nodes where only air or water was present. The measured correlation fluctuations in single phase flow are attributed to noise. It can be seen that for the majority of the nodes (each represented by a different line in the plot), the frame difference Δk_s which shows the greatest level of correlation between the two sensors is approximately 100 frames. This frame shift corresponds to the frame shift between the upstream and downstream sensor signals that was observed in Figure 35.

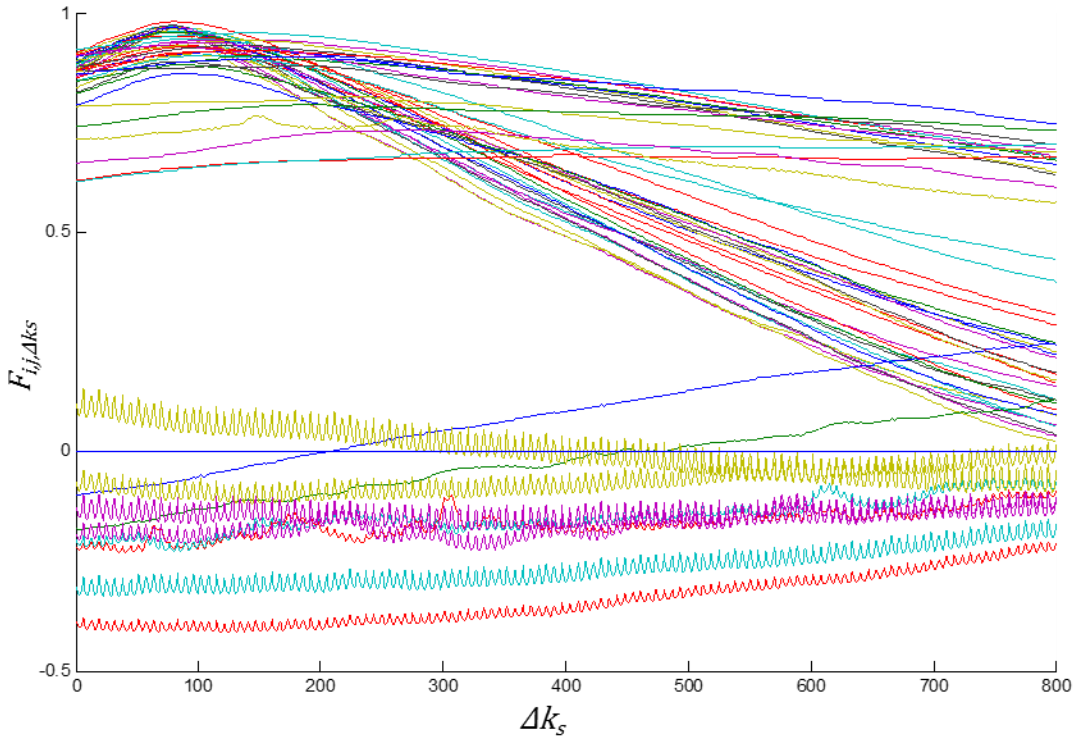

Figure 36: Cross-correlation coefficient of all nodes for various frame shifts

The interest in this work is to determine an average interfacial velocity over the pipe cross-section, rather than nodal values. For that reason, it is necessary to average the nodal measurements of the correlation coefficients. As seen in Figure 36, however, some nodes would not be crossed by the interface sufficiently (or not at all) to provide a meaningful measurement of its velocity. To exclude such nodes from the averaging process, a filtering procedure must then be performed in order to differentiate the nodes with relevant signals, and those that must be discarded when no air-water or water-air interfaces are detected. For each node of the sensor, the histogram of the instantaneous void fraction is analysed. Any node that did not measure instantaneous void fractions both above and below 50% are irrelevant to this analysis and are discarded for interfacial velocity measurement purposes. After the removal of these nodes, the cross-correlation coefficients based on various frame shifts Δk_s for each node that measured at least one interface is plotted, as shown for this representative case in Figure 37.

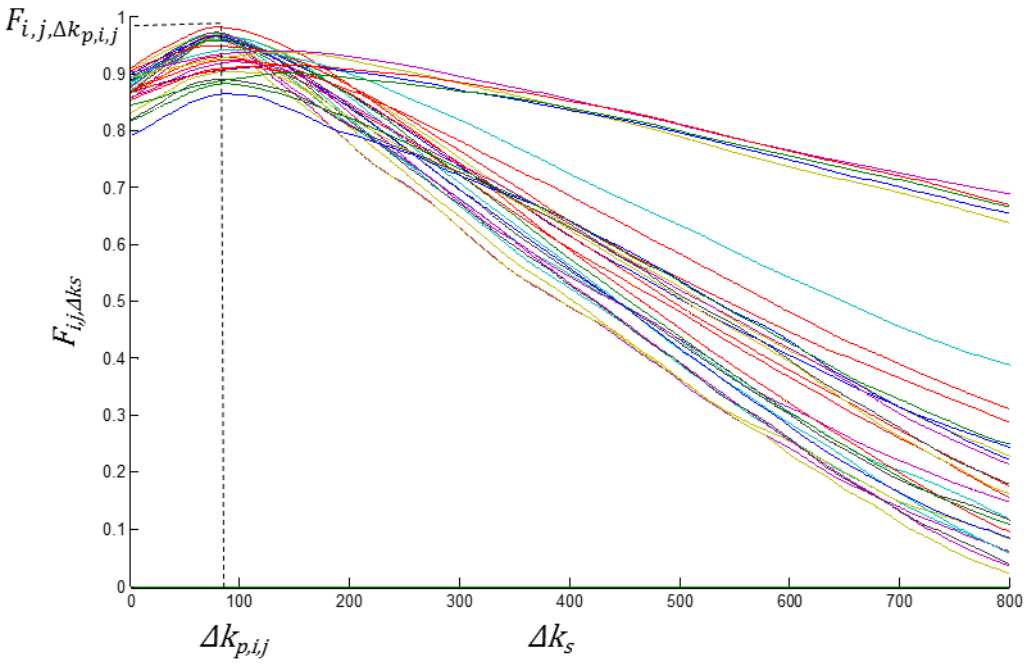

Figure 37: Cross-correlation coefficients of nodes where interfaces were detected, for various frame shifts, showing the peak frame shift for a sample node *i, j*

From this plot, it is then possible to calculate the average interfacial velocity $\overline{u}_{i,j}$ for each node i,j from the frame shift $\Delta k_{p,i,j}$ at the peak cross-correlation coefficient value

$$\overline{u}_{i,j} = \frac{\Delta x \, f_{meas}}{\Delta k_{p,i,j}} \tag{16}$$

The cross-sectional average cross-correlation coefficient $F_{\Delta k_s}$, which depends on the frame shift Δk_s, is calculated as

$$F_{\Delta k_s} = \frac{\sum_{i=1}^{8} \sum_{j=1}^{8} \beta_{i,j} a_{i,j} F_{i,j,\Delta k_{s,i,j}}}{\sum_{i=1}^{8} \sum_{j=1}^{8} \beta_{i,j}} \tag{17}$$

where $\beta_{i,j}$ is a factor equal to 0 if no interface were detected at node i,j, and equal to 1 if at least one interface was detected.

A sample plot of the average cross-correlation coefficient $F_{\Delta k_s}$ for various frame shifts Δk_s is shown in Figure 38. The frame shift Δk_p at peak correlation will be used to determine the average interfacial velocity $\overline{u}$ as

$$\overline{u} = \frac{\Delta x \, f_{meas}}{\Delta k_p} \tag{18}$$

where Δx is the axial distance separating the measurement planes of the sensors. When interfaces are detected at all in-flow nodes of the sensor, this procedure provides an estimate of the time-averaged interfacial velocity across the total cross-section of the pipe. Otherwise, the time-averaged interfacial velocity would be averaged over the cross-section of the pipe over which interfaces have been detected. This would be the case in stratified flow, for example, or at very high or very low void fractions.

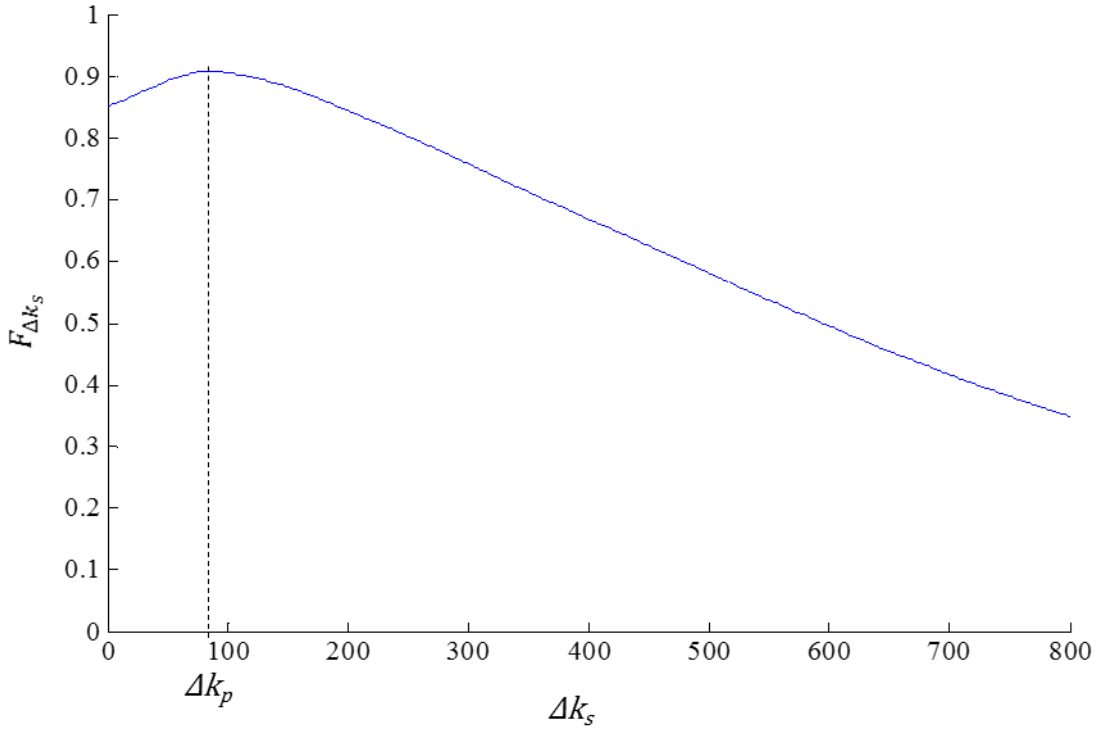

Figure 38: Cross-correlation coefficient $F_{\Delta k}$ for various time shifts Δk_s

It is of interest to also calculate the velocity of individual interfaces within the flow, and to compare the velocity of the gas-liquid interfaces to the velocity of the liquid-gas interfaces. From the instantaneous void fraction maps $\varepsilon_{1,i,j,k}$ and $\varepsilon_{2,i,j,k}$ of the upstream and downstream sensors, respectively, interface maps $\Psi_{1,i,j,k}$ and $\Psi_{2,i,j,k}$ are calculated for each sensor as, for example,

$$\Psi_{1,i,j,k} = \left[\varepsilon_{1,i,j,k+1}\right] - \left[\varepsilon_{1,i,j,k}\right], \quad k = 1 \ldots K-1 \tag{19}$$

where [ ] denotes the rounding of the void fraction to the nearest integer. As a result, $\Psi_{1,i,j,k}$ will indicate liquid to gas interfaces whenever $\Psi_{1,i,j,k} = 1$, gas to liquid interfaces whenever $\Psi_{1,i,j,k} = -1$, and otherwise $\Psi_{1,i,j,k} = 0$. The time-averaged interfacial velocity $\overline{U}_{i,j}$ of node *i,j* (and its associated peak frame shift $\Delta k_{p,i,j}$) will be used as a baseline for these measurements. Starting at the first frame k=1, the program (details in Appendix B) will first search for the first $\Psi_{1,i,j,k1}$ equal to 1 at the frame $k1$, thus selecting only interfaces from liquid to gas towards upstream. For each of these interfaces, it then tries to identify the same interface as it crosses the downstream sensor. The algorithm identifies all cases for which $\Psi_{2,i,j,k2} = 1$ in the range $22 < k2 - k1 < 800$, which corresponds to interfacial velocities between 0.3 and 10 m/s. When several interfaces are detected on the downstream sensor within these parameters, the one with $k2 - k1$ that is closest to the peak frame shift $\Delta k_{p,i,j}$ of that particular node is selected. If no match is found, the interface is discarded. The resulting interfacial velocity $U_{lg,i,j,k}$ of that individual liquid-gas interface is

$$U_{lg,i,j,k1} = \frac{\Delta x \, f_{meas}}{k2 - k1} \tag{20}$$

This procedure is repeated over all frames of the upstream sensor. In a similar fashion, gas-liquid interfaces are detected by searching corresponding signals in the interface map equal to -1.

One source of error in interfacial velocity measurements is the false matching of interfaces by the two sensors, which may happen whenever bubbles coalesce or separate

during the crossing of the sensors. The signal at these instances may be considered as an outlier, which must be discarded. As a first step, the Chauvenet criterion was used, which is a statistical technique for outlier removal and is applicable to processes that have normal distributions. Let $\overline{A}$ and σ_A be the average and standard deviation, respectively, of N samples $A_i, i = 1,2, \dots, N$. A particular sample A_i is considered to be an outlier by the Chauvenet criterion, if $A_i < \overline{A} - \tau\sigma_A$ or $A_i > \overline{A} + \tau\sigma_A$, where the factor τ, shown in Table 8, increases with the number of samples.

Table 8: Chauvenet criterion factor

N	5	6	7	10	15	25	50	100	300	500	1000
τ	1.65	1.73	1.80	1.96	2.13	2.33	2.57	2.81	3.14	3.29	3.48

The Chauvenet criterion may not be used directly on the interfacial velocity measurements, because this velocity is bounded by zero on the low side but is unbounded on the upper side. This is due to the fact that the interfacial velocity is inversely proportional to the measured frame shift: when the latter approaches zero the former tends to infinity, but when the latter becomes exceedingly large the former tends to zero and cannot decrease further. Therefore, a symmetric application of this criterion on both sides of the average could be effective at eliminating outliers at high interfacial velocities, but not necessarily at low interfacial velocities. A more balanced approach is to apply the Chauvenet criterion on the logarithm (base 10) of the interfacial velocity, as described in the following.

Assume that N distinct liquid-gas interfaces were identified, each providing a measurement of the interfacial velocity $\mathcal{U}_{lg}$ and its logarithm $log(\mathcal{U}_{lg})$. The average $\overline{log(\mathcal{U}_{lg})}$ and the standard deviation $\sigma_{log(\mathcal{U}_{lg})}$ are calculated, the factor τ is determined from Table 8, and the Chauvenet criterion is applied on $log(\mathcal{U}_{lg})$. As an example, consider the histogram of a set of 50 measurements of $log(\mathcal{U}_{lg})$, shown in Figure 39. In this case, $N = 50$ and $\tau = 2.57$. The Chauvenet boundaries, as well as the

boundaries corresponding to $\tau = 1$ have been also drawn in this figure for comparisons. It may be seen that four samples were lower than the lower Chauvenet boundary, whereas one sample was higher than the upper Chauvenet boundary. These five samples were discarded as outliers and updated values for the average $\overline{u}_{lg}$ and the standard deviation $\sigma_{u_{lg}}$ of the liquid-gas interfacial velocity were calculated from the remaining population of interfacial velocities. A similar procedure provided the average $\overline{u}_{gl}$ and standard deviation $\sigma_{u_{gl}}$ of the gas-liquid interfacial velocity.

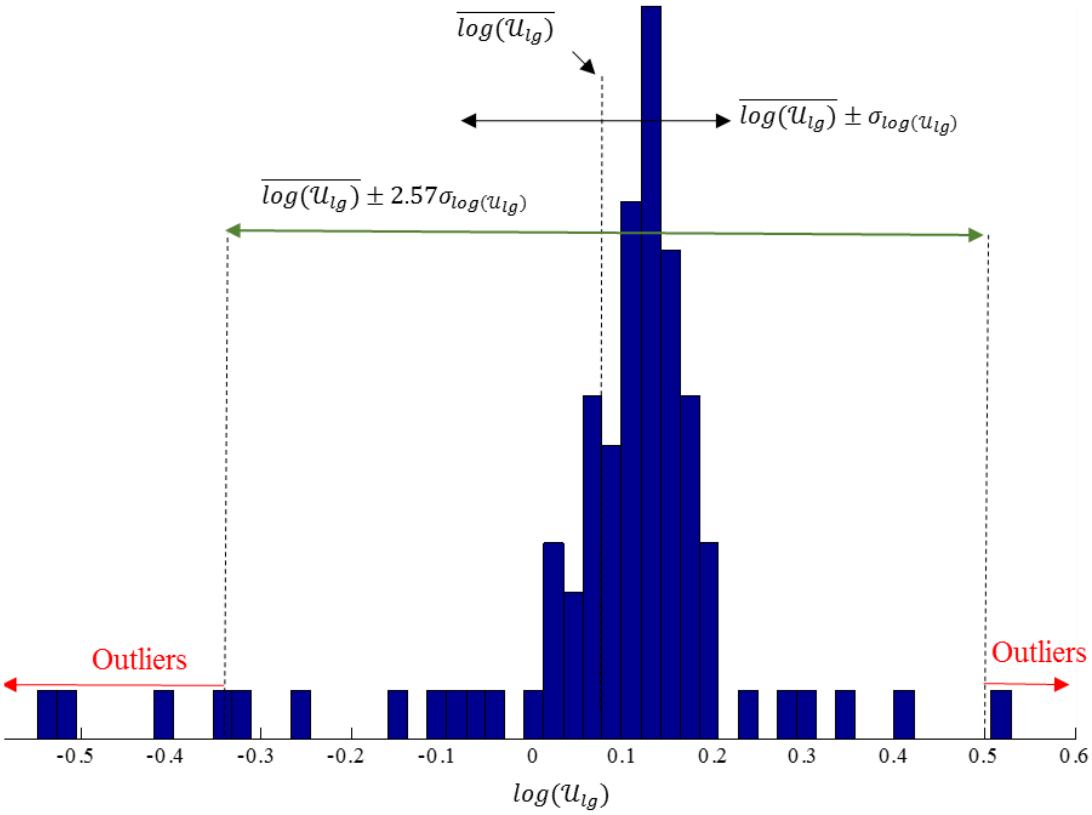

Figure 39: Histogram of the logarithm of the interfacial velocity, and outlier removal range

The Chauvenet criterion is a standard statistical method for removing outliers, but its accuracy for the present results cannot be taken for granted and needs to be examined. This was done for a small number of cases by comparing the sensor measurements of interfacial velocity with values obtained by a visual observation of

the interface maps $\Psi_{1,i,j,k}$ and $\Psi_{2,i,j,k}$, identification of each individual interface and determination of the time each interface takes to travel the distance from the upstream sensor to the downstream sensor. This was a time-consuming process, because a fairly large population of measurements had to be collected for a meaningful comparison. Figure 40 shows a representative example of an interface map for the upstream (top plot) and downstream (bottom plot) sensors for a node located at i=1 and j=4, for a range of 15000 frames, which is equivalent to a time interval of 1.5 s. Corresponding interfaces between the two sensors were identified and their frame shifts were noted. This procedure was repeated for other nodes where interfaces are frequently found, which are typically near the top of the channel in this representative example.

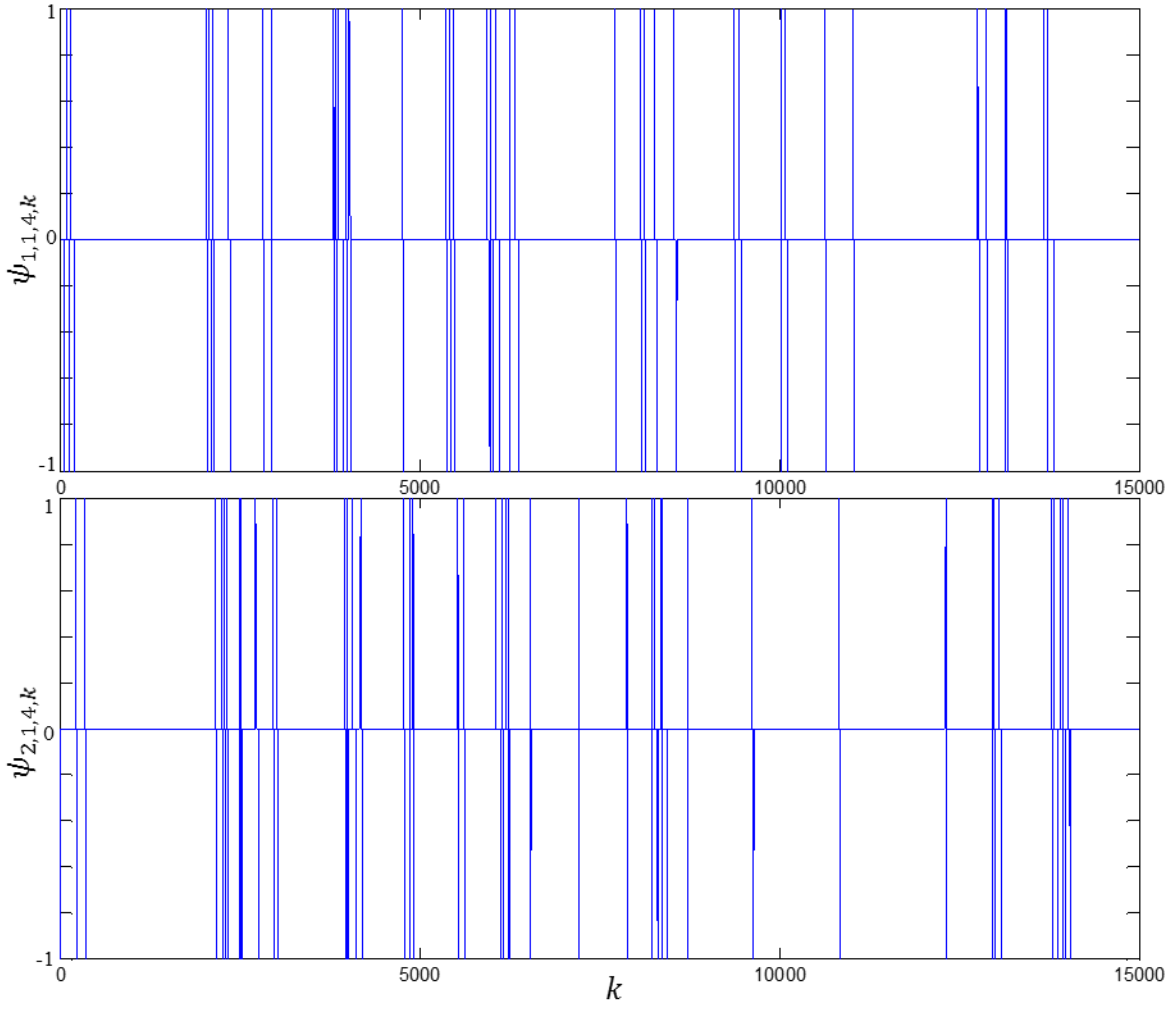

Figure 40: Representative interface maps provided by the upstream (top) and downstream (bottom) sensors at a particular node

A number of interfaces (typically 50 to 100) were identified across the total cross-section of the pipe and then the histogram of the visually obtained velocities was plotted together with the histogram from the WMS measurements, as shown in Figure 41. In the range of velocities surrounding the average, the visual and WMS measurements are in fair agreement. However, it is immediately noticeable that visual measurements do not extend far below or far above the average, whereas several WMS measurements have remote values on either side of the average. In this particular example, the boundaries of the range in which both methods provided measurements are approximately 0.6 and 1.5 m/s. The corresponding Chauvenet boundaries are 0.47 m/s and 3.2 m/s. Therefore, direct comparison has shown that application of the Chauvenet criterion, even on the logarithm of the measured interfacial velocity, would allow many outliers to evade the outlier test. It seems reasonable to assume that WMS measurements of interfacial velocity that have no corresponding visual measurements are erroneous and must be removed.

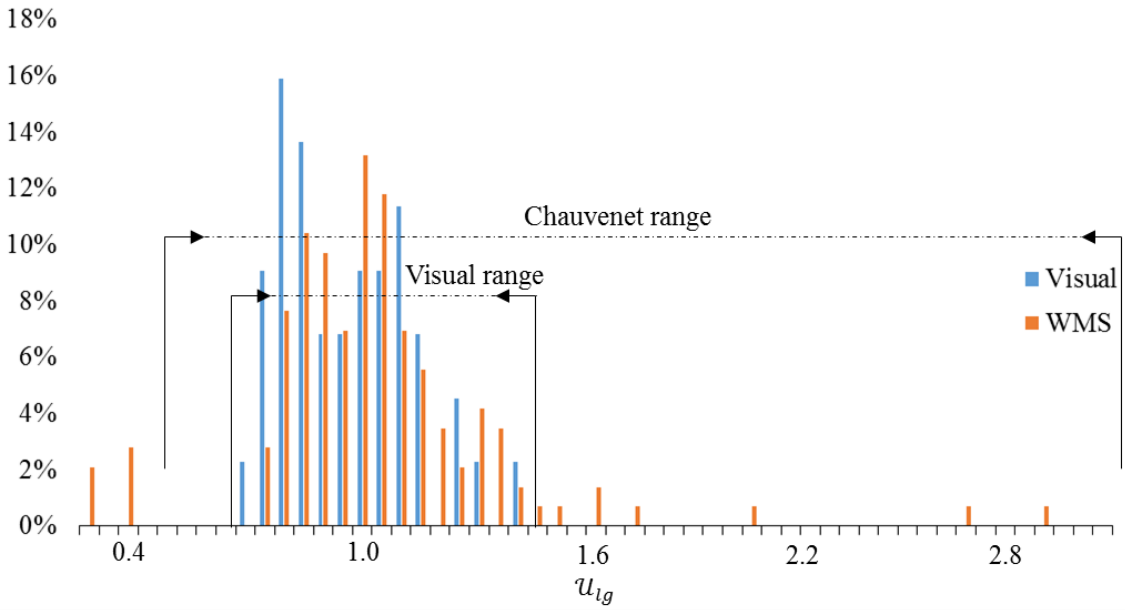

Figure 41: Histogram comparing the liquid-gas interfacial velocities measured visually to those measured by the WMS across the total cross-section

In Figure 42, the WMS measurements were instead selected to be in the same measurement plane of the fourth column of wires (j=4). In both cases, interfaces were

essentially only present in the first row of the sensor ($i = 1$). Although the number of interfaces detected was reduced to around 30, a much closer agreement with the visual measurements was found. Moreover, the Chauvenet criterion boundaries were significantly less wide (0.57 m/s and 1.7 m/s) than previously found in Figure 41, even though that in this particular case a few suspected outliers with values near 1.6 m/s still remained. This suggests that the Chauvenet criterion should be applied on a node-to-node basis rather than to the total population of interfaces across the pipe's cross-section.

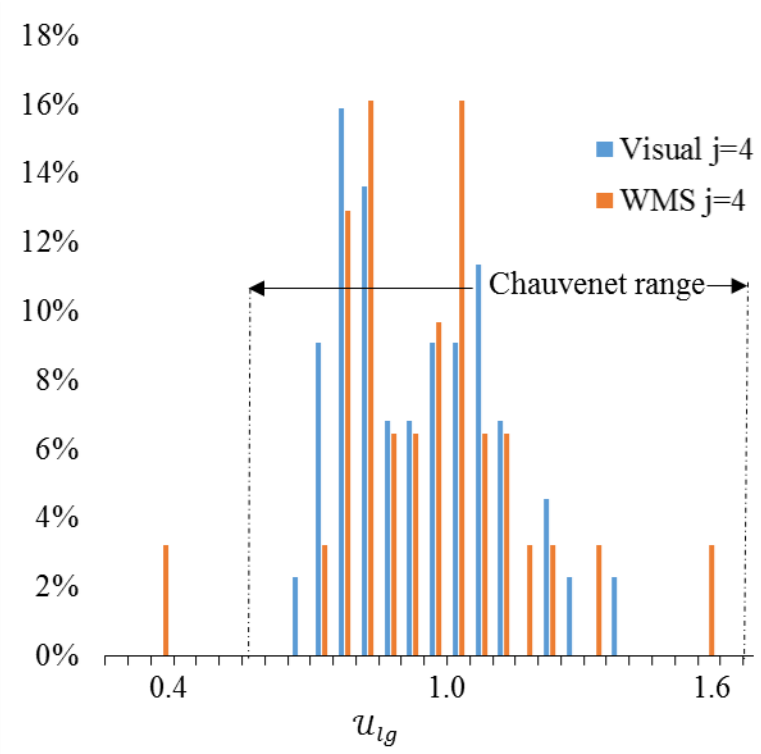

Figure 42: Histogram comparing the liquid-gas interfacial velocities measured visually to those measured by the WMS across a vertical plane (*j*=4)

4.6 Interfacial velocity measurement from high-speed photography

Measurements of interfacial velocity with the use of high-speed photography were used as a standard to which the interfacial velocity measured by the WMS was compared. High-speed photography measurements were only performed for bubbly flows, in which

individual bubbles were separated sufficiently to be visually distinguishable from each other, and not to coalesce or undergo significant deformations. The interfacial velocity of the gas is determined by tracking individual bubbles over many frames and averaging the observations. It relies on several dimensions as shown in Figure 43.

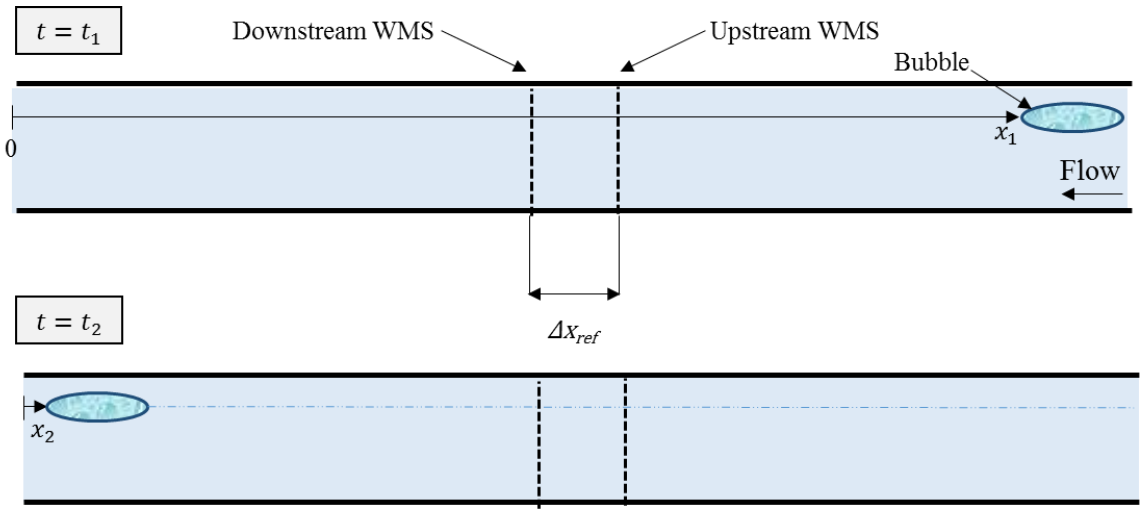

Figure 43: Cross-section view of the test section showing the reference distances for interfacial velocity measurements

The reference distance Δx_{ref} is the distance between points of the two sensors that are furthest away from each other. It is equal to the sum of the distance Δx between the mid-electrode planes of the sensors and the thickness of a single sensor. This reference distance is used to convert the distance travelled by the bubble on the photographs from pixels to units of meters.

Once a bubble enters a frame from the right-hand side of the photograph at time t_1, its downstream interface location x_1 (measured from the left-hand side of the photograph) is noted, along with the frame's time-stamp t_1. This bubble is tracked frame by frame until the second last frame before its downstream interface location leaves the frame, and once again its location x_2 and time stamp t_2 are noted. The distance $x_1 - x_2$

corresponds to the axial distance (measured in meters) travelled by the bubble within the boundaries of the photographs.

The absolute average interfacial velocity $\mathcal{U}_{hsp}$ of a given bubble travelling from a location x_1 to a location x_2 over a period of time $t_2 - t_1$ is found as

$$\mathcal{U}_{hsp} = \frac{x_1 - x_2}{t_2 - t_1} \tag{21}$$

This procedure was repeated many times for a series of bubbles under the same flow conditions and the speeds of individual bubbles were averaged. The raw data of this analysis can be found in Appendix E.

4.7 Uncertainty analysis

The uncertainty in the measurements that were performed in these experiments is the result of the uncertainty of the experimental conditions, the uncertainty of the measuring equipment, and the uncertainty of the data processing procedures. The effects of some sources of uncertainty cannot be accurately quantified and the amount by which they contribute to the overall uncertainty of this analysis is indeterminate. In some cases, these effects can be plausibly considered to be negligible. Deformation due to drag and oscillations due to disturbances in the loop were not visible on the wires of the WMS and so can be safely neglected. Electronic noise in the electronic components was removed by low-pass filtering the signals. Variations in the electric conductivity of water due to temperature variations were also negligible, as the water temperature during the flow loop's operation remained relatively constant (T = 22 ± 2 °C).

4.7.1 Liquid superficial velocity

The relative uncertainty u_{jl}/j_l of the liquid superficial velocity j_l is essentially equal to the relative uncertainty u_{Ql}/Q_l of the water volume flow rate, measured with the ultrasonic flowmeter. The uncertainty is found from the measured volume V and the

elapsed time Δt during the calibration tests, along with their respective uncertainties, which were estimated to be u_V= 0.25 L and u_t= 1 s, as

$$\frac{u_{Ql}}{Q_l} = \sqrt{\left(\frac{u_V}{V}\right)^2 + \left(\frac{u_t}{\Delta t}\right)^2} \tag{22}$$

Based on the calibration tests 8 to 27 (details in Appendix A), the relative uncertainty u_{Ql}/Q_l of the water volume flow rate increased with increasing volume flow rate. Typical values of this relative uncertainty were 0.6% for 0.20 L/s, 0.9% for 0.43 L/s, and 1.8% for 1.8 L/s.

4.7.2 Gas superficial velocity

The relative uncertainty u_{jg}/j_g of the gas superficial velocity j_g is essentially equal to the relative uncertainty u_{Qg}/Q_g of the air volume flow rate, measured with the rotameter**.** It is noted that the air rotameter was calibrated by the manufacturer at the reference temperature $T_r = 21.1$ °C and reference pressure $p_r = 101.3$ kPa. First, the air volume flow rate $Q_{g,r}$ indicated by the rotameter was corrected by considering that during the measurement the air temperature and pressure at the inlet of the rotameter were T_{rot} and p_{rot}, respectively, and not necessarily equal to the reference values. The air volume flow rate through the test section was then calculated from the corrected rotameter reading by considering that the air mass flow rate was constant along the loop, but the air density changed due to change in to the value *p*, measured at the highest point of the test section. In this analysis it has been assumed that surface tension effects on pressure are negligible, so that the pressure inside air bubbles is essentially the same as the pressure of the surrounding water. The temperature difference of the air between the rotameter location and the test section was negligible. Then, the perfect gas law implies that

$$p_{rot} Q_{g,rot} = p Q_g \tag{23}$$

where $Q_{g,rot}$ is the air volume flow rate at the rotameter and Q_g is the air volume flow rate in the test section. Applying the corrections for pressure and temperature (Key Instruments) with respect to the reference calibrations values p_r and T_r respectively, yields

$$Q_{g,rot} = Q_{g,r}\sqrt{\frac{p_{rot}T_r}{p_r T_{rot}}} \tag{24}$$

where all pressures are expressed as absolute pressures and temperatures are expressed in Kelvin. Substituting equation (24) in equation (23) and isolating Q_g yields

$$Q_g = Q_{g,r}\frac{p_{rot}}{p}\sqrt{\frac{p_{rot}T_r}{p_r T_{rot}}} \tag{25}$$

The relative uncertainty u_{Qg} of the gas volume flow rate is

$$\frac{u_{Qg}}{Q_g} = \sqrt{\left(\frac{u_{Qg,r}}{Q_{g,r}}\right)^2 + \left(\frac{3}{2}\frac{u_{p_{rot}}}{p_{rot}}\right)^2 + \left(\frac{u_p}{p}\right)^2 + \left(\frac{1}{2}\frac{u_{T_{rot}}}{T_{rot}}\right)^2} \tag{26}$$

where $u_{Qg,r}/Q_{g,r} = 0.113\ L/s/Q_{g,r}$ is the relative uncertainty of the rotameter (Table 5), $u_{p_{rot}}$= 0.7 kPa and u_p= 0.7 kPa are the uncertainties of p_{rot} and p respectively, and $u_{T_{rot}}$= 2 K is the uncertainty of the temperature at the rotameter. The relative uncertainty of the air volume flow rate varies depending on both the liquid and gas volume flow rates. Generally, the uncertainty decreases as the air volume flow rate increases. In theory, it would also decrease as the water volume flow rate increased, but the latter has a negligible effect on the gas flow rate uncertainty. In Figure 44 and Figure 45, the relative uncertainties of the gas volume flow rate are plotted for different combinations of liquid and gas volume flow rates, for gas backpressures of 203 kPa and 405 kPa, respectively. They are found to collapse on a single line, regardless of the water flow rate, starting at roughly 30% at the lowest water flow rates down to roughly 5% at the highest water flow rates. The backpressure does not show any effect on this trend.

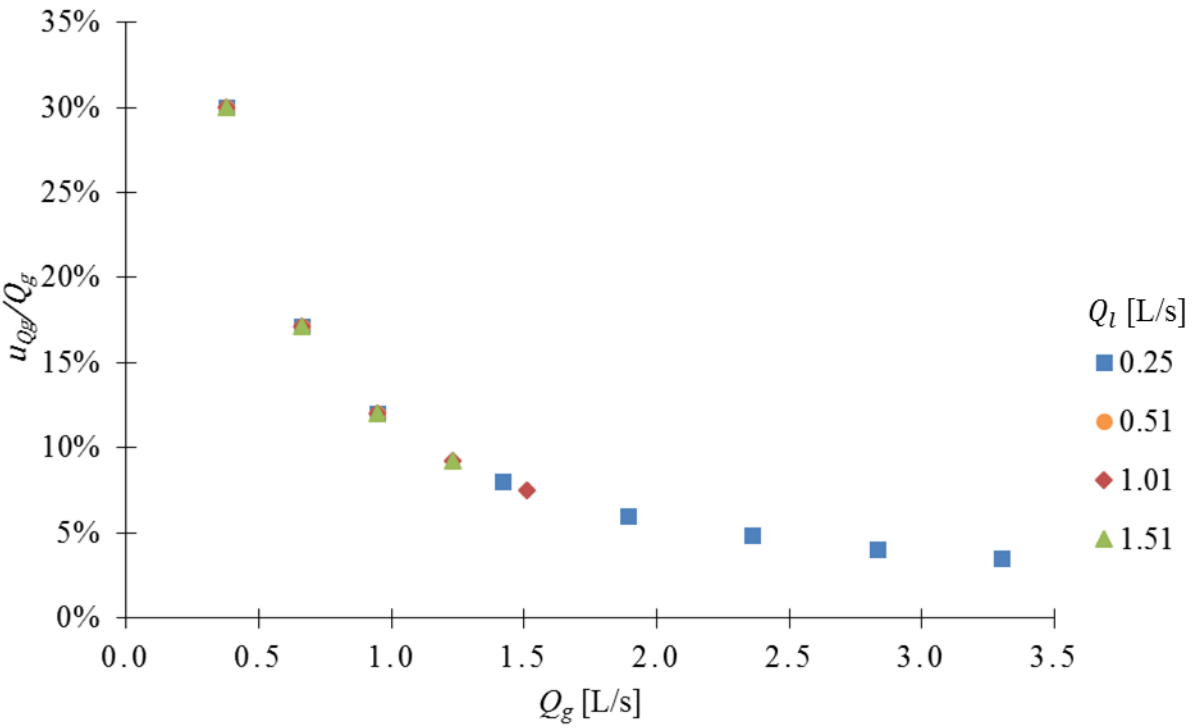

Figure 44: Air volume flow rate uncertainty (203 kPa backpressure)

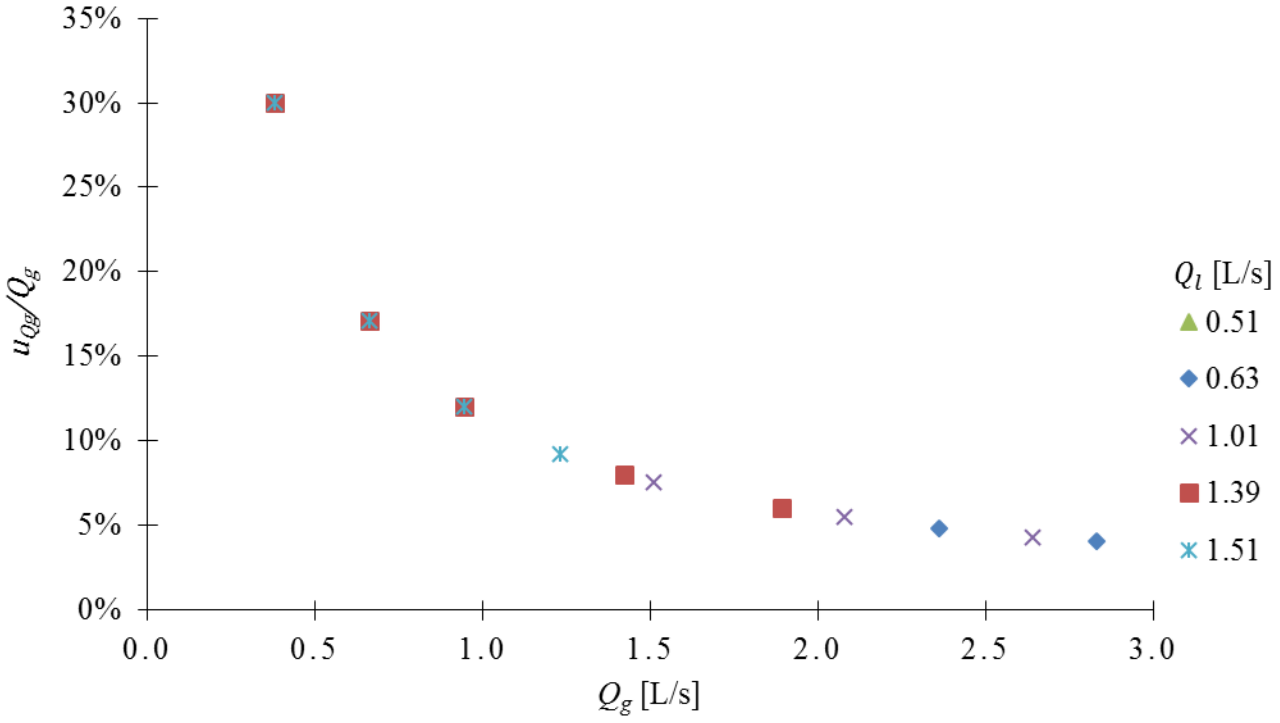

Figure 45: Air volume flow rate uncertainty (405 kPa backpressure)

4.7.3 Void fraction

As there was no alternative means of measuring void fraction in this setup, it is not possible to determine directly the uncertainty of the WMS void fraction measurements. It is evident, however, that the uncertainty $u_{\overline{\varepsilon}}$ of the average void fraction $\overline{\varepsilon}$ needs to be determined separately for each flow regime. Some rather extreme examples of conditions that would introduce large errors in void fraction measurements are shown in Figure 46.

On the left, an air bubble of diameter S, which is equal to or smaller than the wire spacing, crosses the sensor without being in contact with any of the wires. In this circumstance, the WMS would measure a void fraction of 0, while the actual void fraction would be 0.015, if S were equal to the wire spacing, or smaller otherwise. Next, consider an ideally undisturbed stratified flow, as shown in the middle image, where the interface is located just under the third row of horizontal wires; in this case, the WMS would measure a void fraction of 0.35, while the actual void fraction would be 0.29. Finally, consider another stratified flow whose interface is located just above the first row of horizontal wires; in this case, the WMS would measure a void fraction of 0 instead of the correct value of 0.035. These examples illustrate that in some cases the uncertainty of void fraction could be substantial. These are, however, instantaneous results and the degree by which they contribute to the uncertainty of the average void fraction cannot be easily quantified for a wide range of conditions.

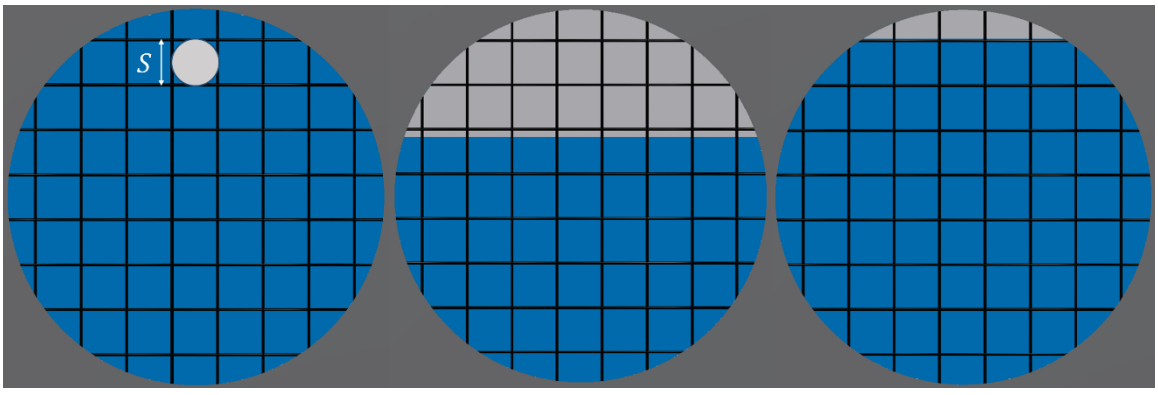

Figure 46: Examples of a sparse bubbly flow (left), and stratified flows (middle and right), which would be subject to large errors in void fraction measurement

4.7.4 Interfacial velocity estimated by photography

The uncertainty $u_{\mathcal{U}_{hsp}}$ of the interfacial velocity $\mathcal{U}_{hsp}$ measured by high-speed photography depends on the uncertainties u_x of the axial distance $x_1 - x_2$ travelled by the bubble and the time difference $t_2 - t_1$ during which that distance was travelled.

The bubble displacement $x_1 - x_2$ was determined from the difference between the pixel numbers corresponding to the interface of the bubble at the two instances, scaled by the difference between the pixel numbers marking the reference distance, which was given as Δx_{ref} =24.7 ± 0.2 mm. The uncertainty of each pixel number is taken to be 1 pixel. The bubble location was traced over the length of the image, which was 2560 pixels and the reference distance corresponded to 308 pixels. Therefore, the relative uncertainty of the bubble displacement was estimated as

$$\frac{u_x}{x_1 - x_2} = \sqrt{\left(\frac{2}{2560}\right)^2 + \left(\frac{2}{308}\right)^2 + \left(\frac{0.2\ mm}{24.7\ mm}\right)^2} = 1\% \tag{27}$$

The uncertainty u_t of the time difference is estimated from the frequency $f_{meas,hsp}$ of the camera as

$$u_t = \frac{2}{f_{meas,hsp}} = 9\ ms \tag{28}$$

The relative uncertainty of the interfacial velocity is

$$\frac{u_{\mathcal{U}_{hsp}}}{\mathcal{U}_{hsp}} = \sqrt{\left(\frac{u_x}{x_1 - x_2}\right)^2 + \left(\frac{u_t}{t_2 - t_1}\right)^2} \tag{29}$$

And so it depends on the flow conditions. At low flow rates, this relative uncertainty was typically around 2%, and increased up to 11% at the highest flow rates.

4.7.5 Interfacial velocity measured by WMS

The spacing between the measurement planes of the sensors was Δx = 22.7 mm and its uncertainty was estimated to be $u_{\Delta x}$ = 0.3 mm. In view of the high sampling rate of the sensor, it may be assumed that the uncertainty of the time measurement based on the sensor's frame shift was negligible.

The uncertainty $u_{\Delta k_{p,i,j}}$ of the peak frame shift $\Delta k_{p,i,j}$ of each node i,j is determined as follows. For each node i,j of the sensor that detected some interfaces ($\beta_{i,j}$=1), a low bound frame shift $\Delta k_{lb}$and a high bound frame shift Δk_{hb} were determined as the shifts on the cross-correlation plot (Figure 47) that corresponded to cross-correlation coefficients $F_{i,j,\Delta k_s}$ that were 2% lower than the peak cross-correlation coefficient $F_{i,j,\Delta k_p}$.

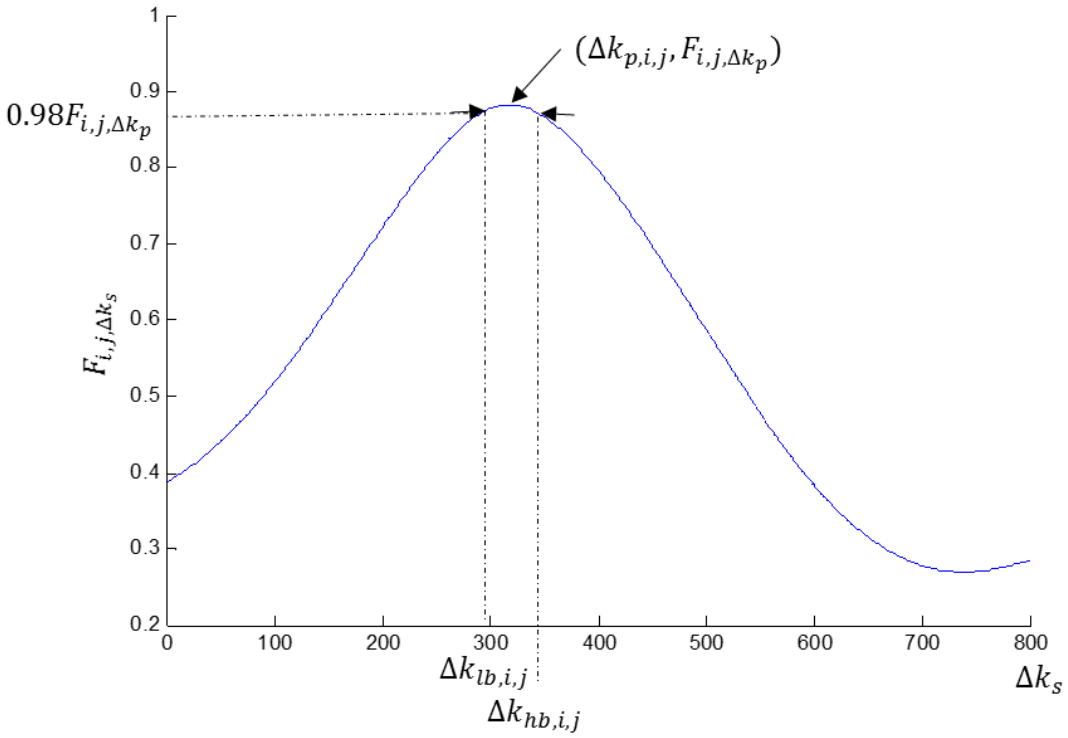

Figure 47: Procedure to calculate the uncertainty of the peak frame shift

The relative uncertainty $u_{\mathcal{U}_{i,j}}/\mathcal{U}_{i,j}$ at any node i,j is

$$\frac{u_{\mathcal{U}_{i,j}}}{\mathcal{U}_{i,j}} = \sqrt{\left(\frac{u_{\Delta x}}{\Delta x}\right)^2 + \left(\frac{u_{\Delta k_{i,j}}}{\Delta k_{i,j}}\right)^2} \tag{30}$$

where

$$\frac{u_{\Delta k_{i,j}}}{\Delta k_{i,j}} = \sqrt{\frac{1}{2}\left(\frac{\Delta k_{lb,i,j} - \Delta k_{p,i,j}}{\Delta k_{p,i,j}}\right)^2 + \frac{1}{2}\left(\frac{\Delta k_{hb,i,j} - \Delta k_{p,i,j}}{\Delta k_{p,i,j}}\right)^2}\Bigg|_{i,j} \tag{31}$$

The cross-section averaged uncertainty $u_{\overline{\mathcal{U}}}/\overline{\mathcal{U}}$, averaged over all nodes which detected some interfaces, is

$$\frac{u_{\overline{\mathcal{U}}}}{\overline{\mathcal{U}}} = \sqrt{\frac{\sum_{i=1}^{8}\sum_{j=1}^{8}\beta_{i,j}\left(\frac{u_{\mathcal{U}_{i,j}}}{\mathcal{U}_{i,j}}\right)^2}{\sum_{i=1}^{8}\sum_{j=1}^{8}\beta_{i,j}}} \tag{32}$$

The average interfacial velocity uncertainty for each measurement is included in Appendix D. This uncertainty varies from roughly 25% at low liquid flow rates, 20% at medium liquid flow rates and 10 % at high liquid flow rates.

The uncertainty $u_{\mathcal{U}}$ of the interfacial velocity of a single interface is

$$\frac{u_{\mathcal{U}}}{\mathcal{U}} = \sqrt{\left(\frac{u_{\Delta x}}{\Delta x}\right)^2 + \left(\frac{u_{\Delta k_s}}{\Delta k_s}\right)^2} \tag{33}$$

where $u_{\Delta k_s}$= 2, resulting in a interfacial velocity uncertainty of 1.3% at 0.5 m/s, 1.6% at 1 m/s and 2.2% at 2 m/s.

4.8 Flow distortion

The WMS is an intrusive device, reducing the effective cross-sectional area of the pipe by roughly 7% as well as introducing some permanent pressure loss. More importantly, gas bubbles and plugs may be intersected, often multiply, by the sensor wires, which may have an effect on their size, shape and speed. As a result, several flow distortion features were observed, some of which only apply to specific flow regimes.

In most circumstances, the gas-liquid interfacial velocity was found to be greater than the liquid-gas interfacial velocity, indicating that, for a given bubble, its downstream extremity will tend to be slower in the region between the sensors than its upstream extremity, which would result in bubble deformation.

In plug flow regimes, where the bubbles carried by the flow are larger than the mesh size of the WMS, breakdown and/or deformation have been observed. Most notably, a plug of air tends to be slowed down as its downstream edge comes into contact with the wires. This causes a bubble with an elongated outline (marked by 1 in Figure 48) to deform towards a spherical shape after it crosses the sensor wires (marked by 2 in Figure 48).

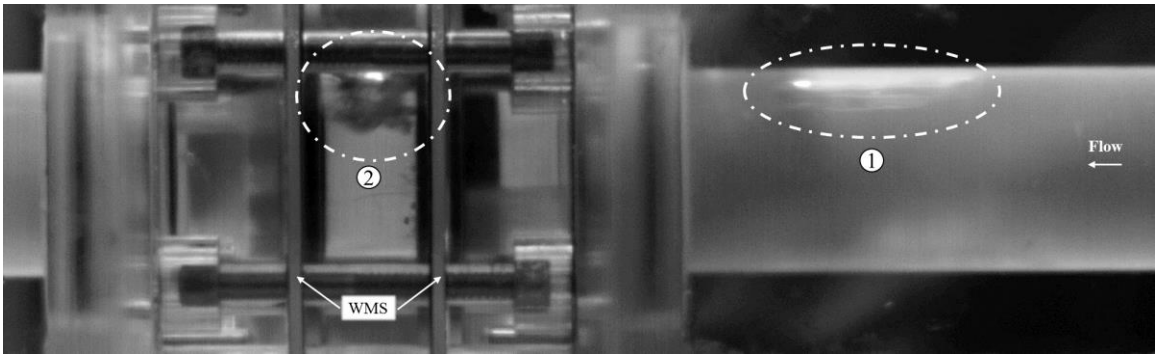

Figure 48: Air plug deformation

Chapter 5 Results

This chapter describes the results of the experiments. First, an overview of the flow regimes that were successfully generated by the air-water flow loop is presented. A flow pattern map illustrates the 315 data sets which were recorded. The measurement results for the void fraction and interfacial velocity are presented. The void fraction measurement discrepancies between the two sensors and the two calibration techniques are shown, followed by the drift-flux parameters that were obtained from these measurements. A qualitative description of the flow distortion and effects inherent to the intrusion of the device are finally discussed.

5.1 Flow regime maps

The flow loop was designed to operate over wide ranges of air and water flow rates. By adjusting one independently of the other, various flow regimes were produced. Figure 49 shows six photographs taken in the refractive-index matching section upstream of the WMS, as representative images of different flow patterns. The flow regime to which they correspond is determined visually based on the distinctive features of each regime, as described in section 2.2. The bubbly flow regime contains small (with a diameter that is smaller by an order of magnitude than the pipe diameter) dispersed bubbles. In plug flow, the bubbles are very long. Slug flow occurs when the pipe is roughly filled equally with air and water, but when the waves at the surface have such an amplitude that they reach the top of the channel, breaking down the air into long (several diameters in length) separate air pockets. Stratified flow can be distinguished by a fairly smooth water-air interface, while stratified-wavy flow has a disturbed interface (recognizable on the photographs by the darker tone). Misty-annular flow contains an eccentric air core, while the water tends to stick to the pipe's walls. The thickness of the water is larger at the bottom than the top due to gravitational forces.

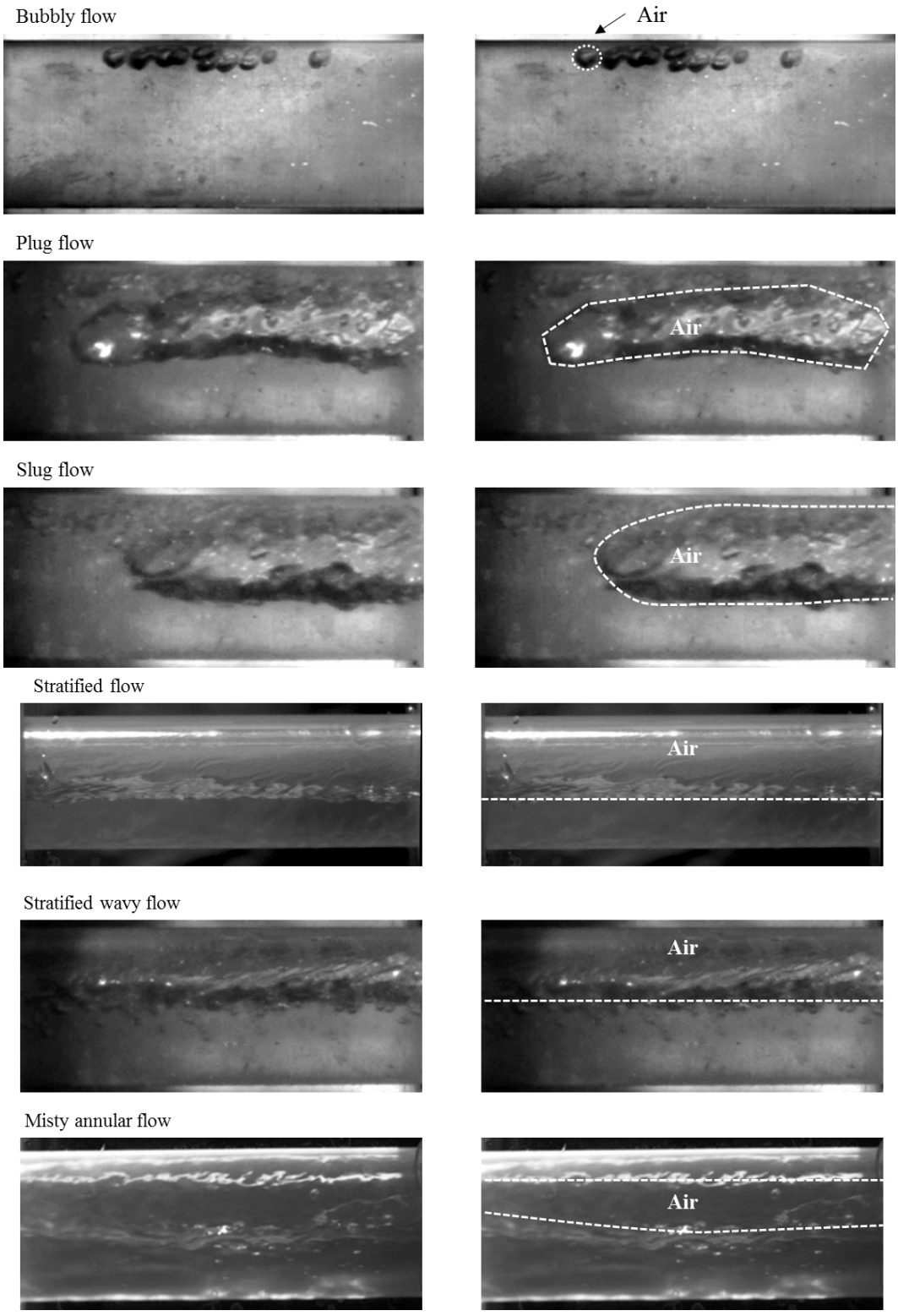

Figure 49: Representative images of flows in different regimes (flow direction from right to left); the column on the right contains the same images but with the water-air interfaces sketched by hand

A photograph of an air slug followed by dispersed bubbles is shown in Figure 50. This image is distorted by refraction of light in the acrylic pipe wall through which it was taken.

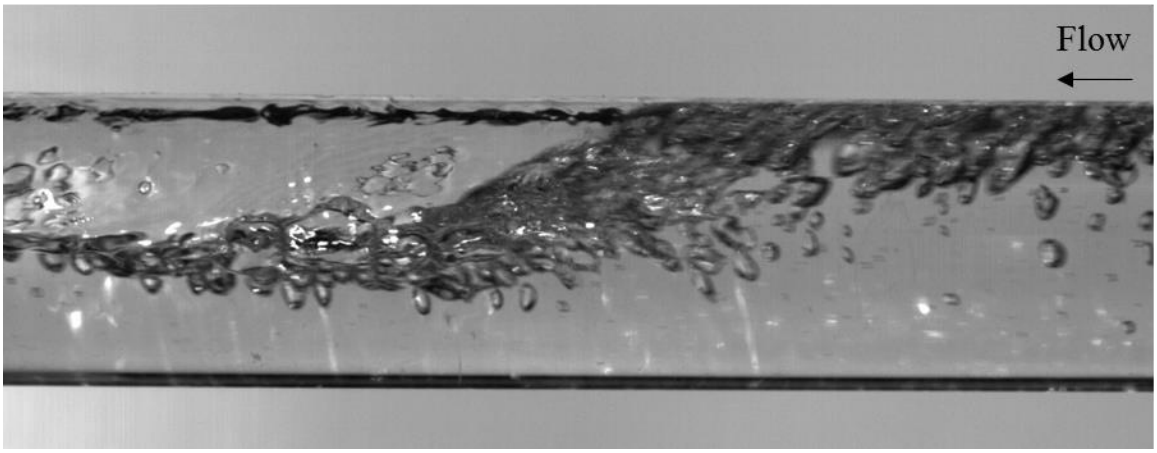

Figure 50: Image of an air slug followed by a stream of small dispersed bubbles

Flow regime maps of the cases studied are shown in Figure 51 and Figure 52, in logarithmic and linear scales, respectively. Areas covering conditions under which each flow regime was observed have been marked by different colours. The boundaries of these flood maps are approximate, and do not necessarily overlap at any particular location. As a result, the white areas in between neighbouring regimes correspond to transitional states.

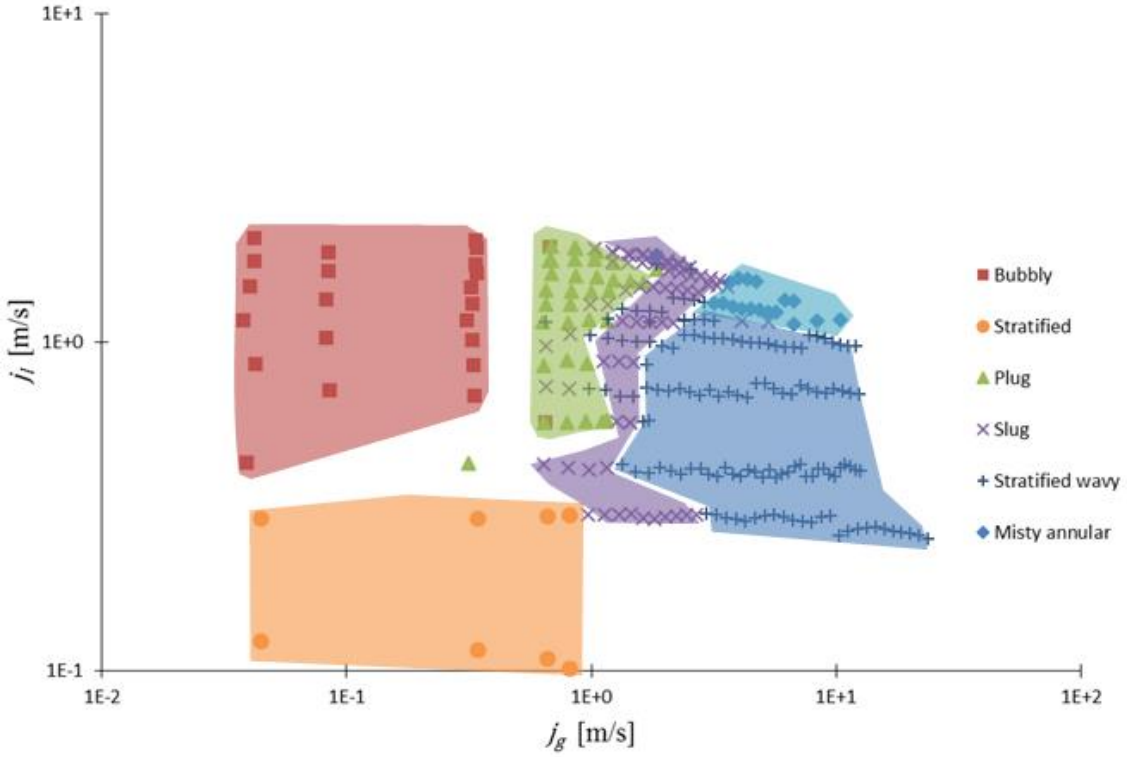

Figure 51: Flow regime map in logarithmic axes

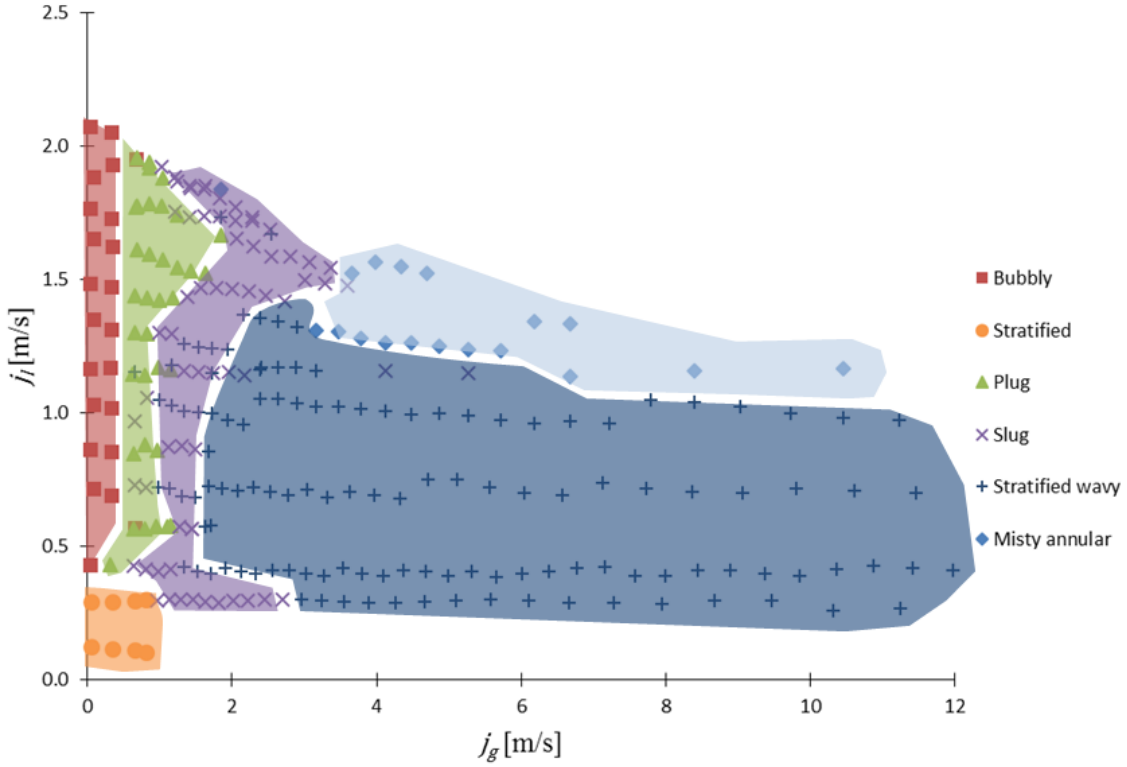

Figure 52: Flow regime map in linear axes

5.2 Void fraction measurements

5.2.1 Calibration method effect

Two different calibration methods for void fraction measurement by WMS sensors were considered, as discussed in Chapter 4.4: histogram calibration and time-averaged calibration. Figure 53 shows the difference between the average void fractions $\overline{\varepsilon}_{hc}$ and $\overline{\varepsilon}_{tac}$ measured by the upstream sensor calibrated by the histogram and time-averaged methods, respectively, vs. $\overline{\varepsilon}_{tac}$. At low void fractions (bubbly flow regime), both techniques yield comparable results. As the void fraction increases, however, it is clear that $\overline{\varepsilon}_{hc} - \overline{\varepsilon}_{tac}$ becomes increasingly more negative. In misty-annular flow in particular, this difference becomes significant, reaching values of about -0.035. When all cases were considered, $\overline{\varepsilon}_{hc}$ was lower than $\overline{\varepsilon}_{tac}$ by about 0.010. Figure 54 shows the same difference for void fraction measurements obtained by both the upstream and downstream sensors. This figure shows clearly that the difference was larger for the downstream sensor than for the upstream one. With all cases considered, the difference for the downstream sensor was -0.018.

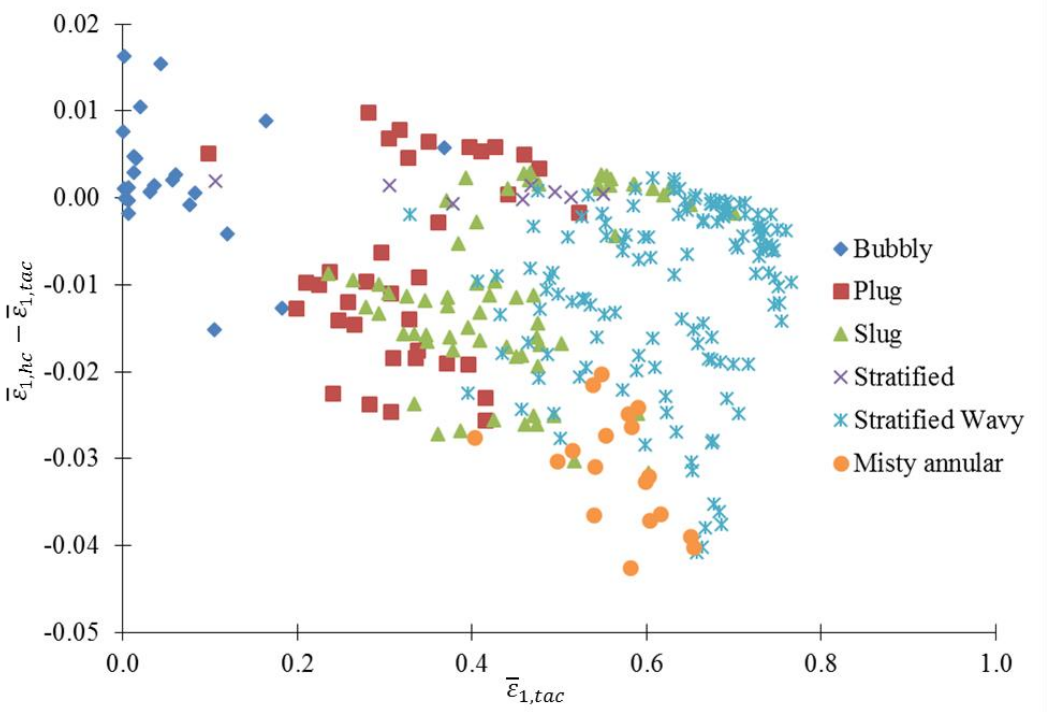

Figure 53: Difference between void fraction measurements by the upstream sensor, obtained by using two different calibration methods

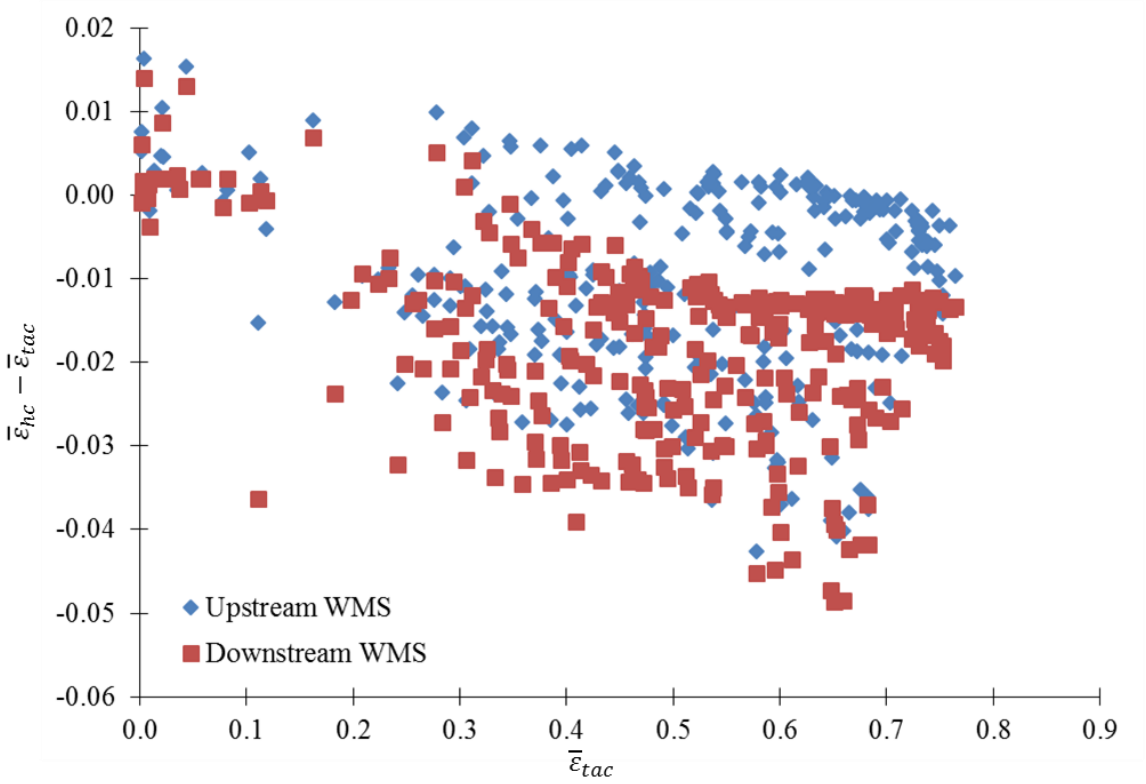

Figure 54: Difference between void fraction measurements by the upstream and downstream sensors, obtained by using two different calibration methods

The main advantage of the histogram calibration method is that it does not rely on two distinct measurements made at different times. However, this method requires the presence of sufficient quantities of both air and water during the measurement at every node in order to produce reliable results, which is not the case for stratified and annular flow. Due to these restrictions, the time-averaged calibration method is preferable in circumstances where a variety of flow regimes is expected to be encountered. All void fraction results presented in the remainder of this report are based on time-averaged calibration.

5.2.2 Void fraction maps

The output of each WMS is a set of frames containing the instantaneous void fraction at each node. Averaging these values for each node over the duration of the measurement yields the time-averaged void fraction at each node. Plots of these properties illustrate the instantaneous and average shapes of the air-water interface on cross-sections of the pipe normal to its axis. It is also possible to visualize the approximate instantaneous shapes of axial cross-sections of the air-water interface by plotting the time history of void fraction values along a single row or column of WMS nodes against the frame number, which is proportional to time. Examples of these plots are shown in Figure 55. Note that the spacing of void fraction measurements in the axial direction is much finer than that in the normal plane, which is equal to the spacing of the parallel wires of the WMS.

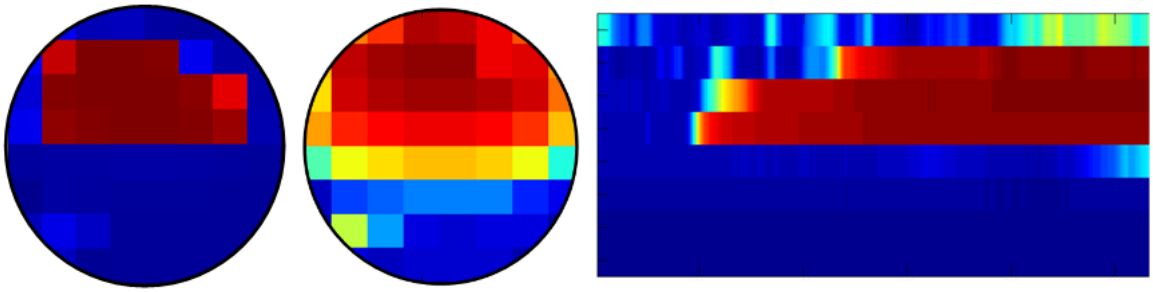

Figure 55: a) Instantaneous void fraction map on a normal plane; b) time-averaged void fraction map on a normal plane; c) instantaneous void fraction map on a vertical axial plane; red colour corresponds to air and blue colour to water

5.2.3 Comparison of measurements by the upstream and downstream sensors

In Figure 56, a representative example of a side view of the flow is shown. It corresponds to the void fraction maps of the upstream and downstream sensors on the vertical axial plane. The resolution in the axial direction is much greater than in the vertical direction, due to the high measurement frequency. In this plot it is easy to identify the corresponding interfaces detected by the two sensors and the frame shift between them.

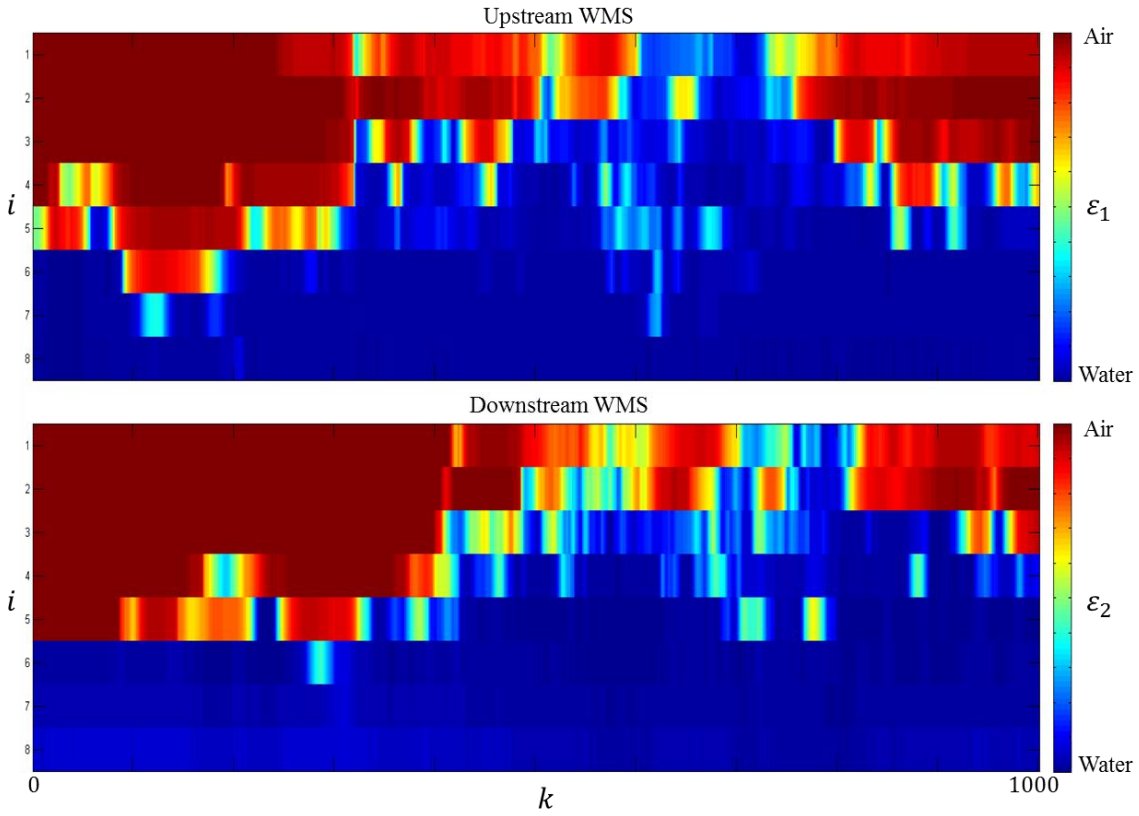

Figure 56: Example of instantaneous void fraction maps on a vertical axial plane of the upstream and downstream WMS; red colour corresponds to air and blue colour to water

The comparison of the time-averaged void fractions of the upstream and downstream sensors provides some insight into the effect of flow disturbance by the wires of the WMS. Figure 57 shows the difference between the average void fraction measured by the upstream and downstream sensors plotted against the water superficial velocity.

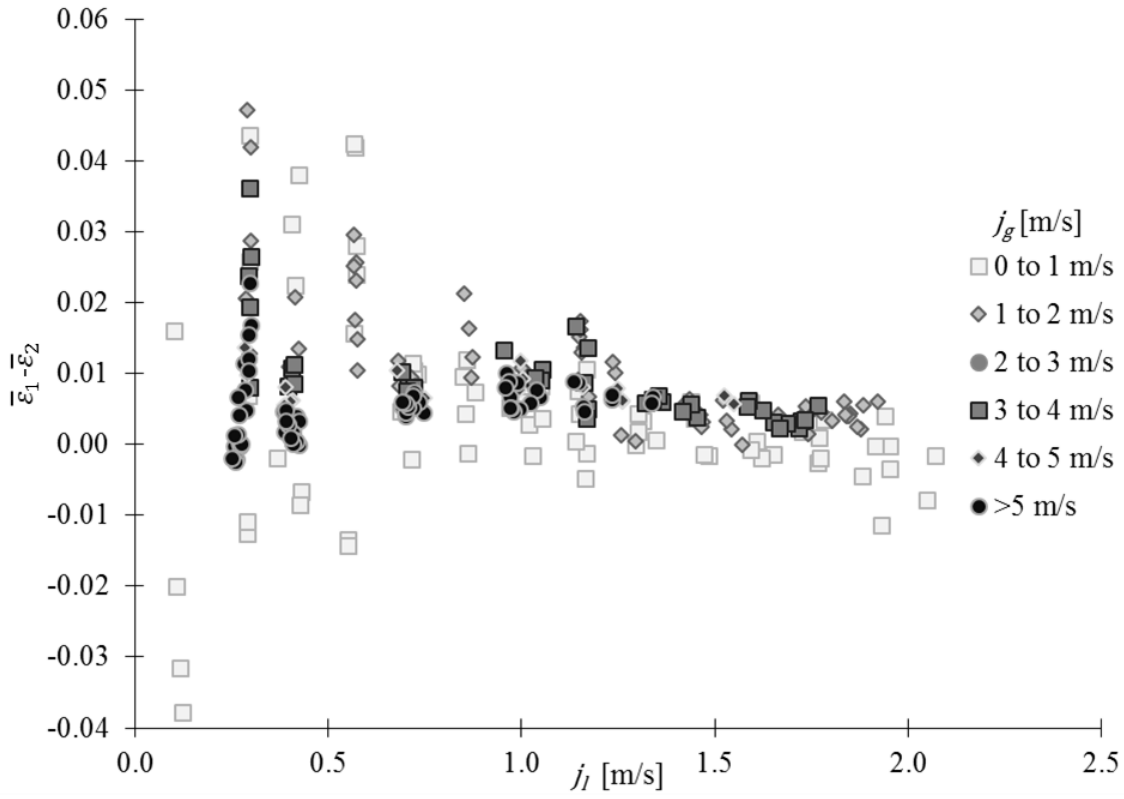

Figure 57: Difference between average void fraction measured by upstream and downstream sensors

In most cases the upstream sensor measured a larger void fraction than the downstream one. Larger deviations occurred at superficial water velocities lower than 1 m/s. The measurement difference tends to decrease with increasing liquid superficial velocity. These large discrepancies also correspond to the lowest air superficial velocities (bubbly flow), for which the gas is less likely to cross the aligned nodes of both sensors in a consistent fashion. Because the upstream sensor encounters a flow which is less affected by the intrusiveness of the device than the downstream sensor is, its void fraction measurements are expected to be more representative of the flow upstream of the test section. From here onwards, all void fraction measurements presented were taken from the upstream sensor only.

5.2.4 Measurements in different flow regimes

Contours of the time-averaged volumetric void fraction $\overline{\varepsilon}$ have been plotted on the flow regime map in Figure 58. It is worth noting that very high void fractions are only reached at the lowest liquid superficial velocities, corresponding to the wavy flow regime. The same results are plotted in Figure 59 as void fraction vs. water superficial velocity. Following a horizontal line at constant j_l, we note that the void fraction increases more rapidly at low gas flow rates than at higher ones. The flow regimes transition from one to the next in a fairly consistent fashion, from bubbly to plug, slug and finally to either stratified wavy or misty annular. It is noteworthy to also mention that the boundaries separating many of the regimes roughly follow the same path as the lines showing the constant void fractions, which suggests that the flow regime and void fraction are strongly correlated.

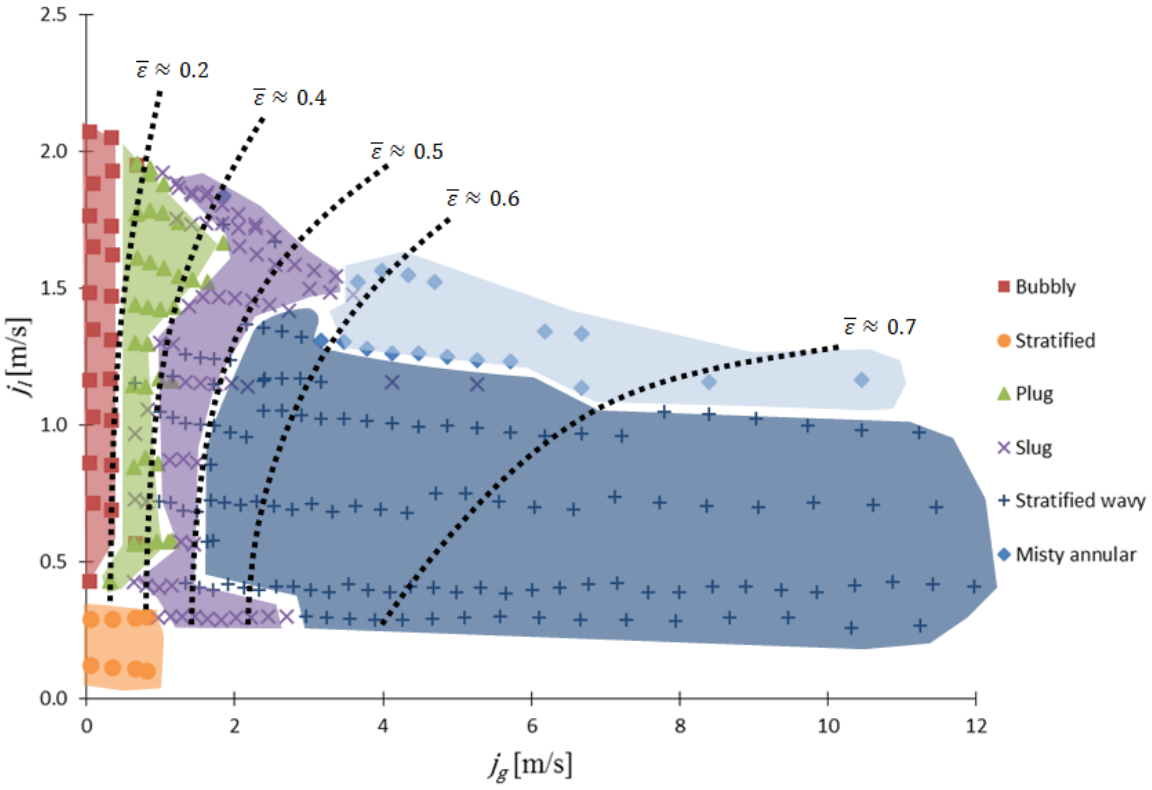

Figure 58: Average volumetric void fraction contours in the flow regime map

When plotting the void fraction with respect to the liquid superficial velocity, the vast majority of the data are found to gather at the top of the plot, and be sparser near the bottom where the void fraction is lower and more sensitive to the gas flow rate.

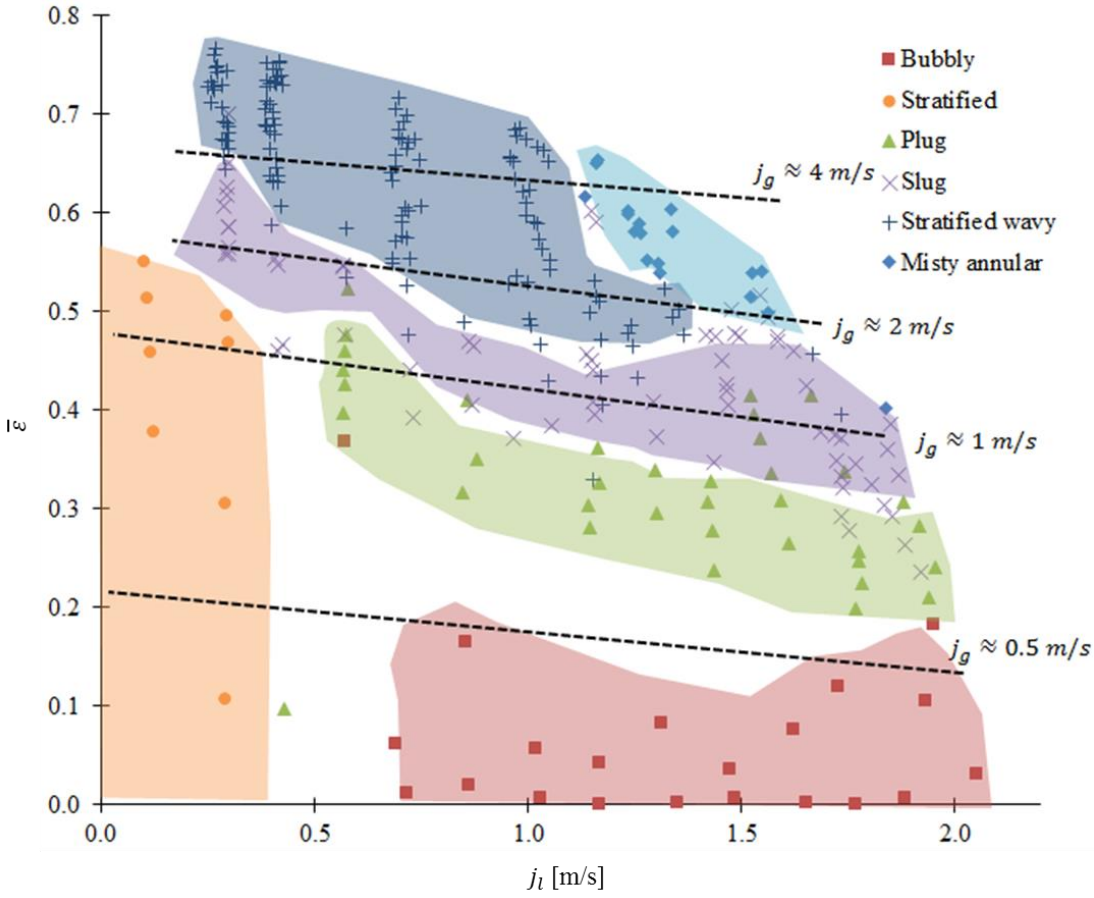

Figure 59: Void fraction vs. water superficial velocity in different flow regimes

5.3 Interfacial velocity measurements

5.3.1 Comparison of WMS measurements with photographic results

Independent measurements of the interfacial velocity were made by tracking the air-water interface on successive images recorded with the high-speed camera. This was only done for sparse bubbly flows, for which it was possible to track photographically individual bubbles and determine their average velocity between an upstream and downstream location of the test section, as described in Chapter 4.6. A comparison of a

selection of WMS measurements of the average liquid-gas interfacial velocity and corresponding photographic results in bubbly flows is shown in Figure 60. The straight black dotted line represents the condition for which the liquid superficial velocity and interfacial velocity would be equal. The results for both measurement techniques are shown together with the corresponding uncertainty bars at 95% confidence level, i.e., twice their standard deviation. A fairly good agreement between the two measurement techniques is observed, over all ranges of liquid superficial velocities. The uncertainty from the WMS is higher than the one from high speed camera. This is attributed to two sources. The number of distinct interfaces measured is at least ten times higher, resulting in a larger statistical scatter, and the WMS measurement took into consideration all bubbles detected, including the very small ones, which were difficult to track by high-speed photography. It is also important to point out that the WMS measured the average interfacial velocity over the distance between the two sensors (roughly 20 mm), while the high speed camera measured it over the distance from the upstream and downstream end of the test section (roughly 180 mm).

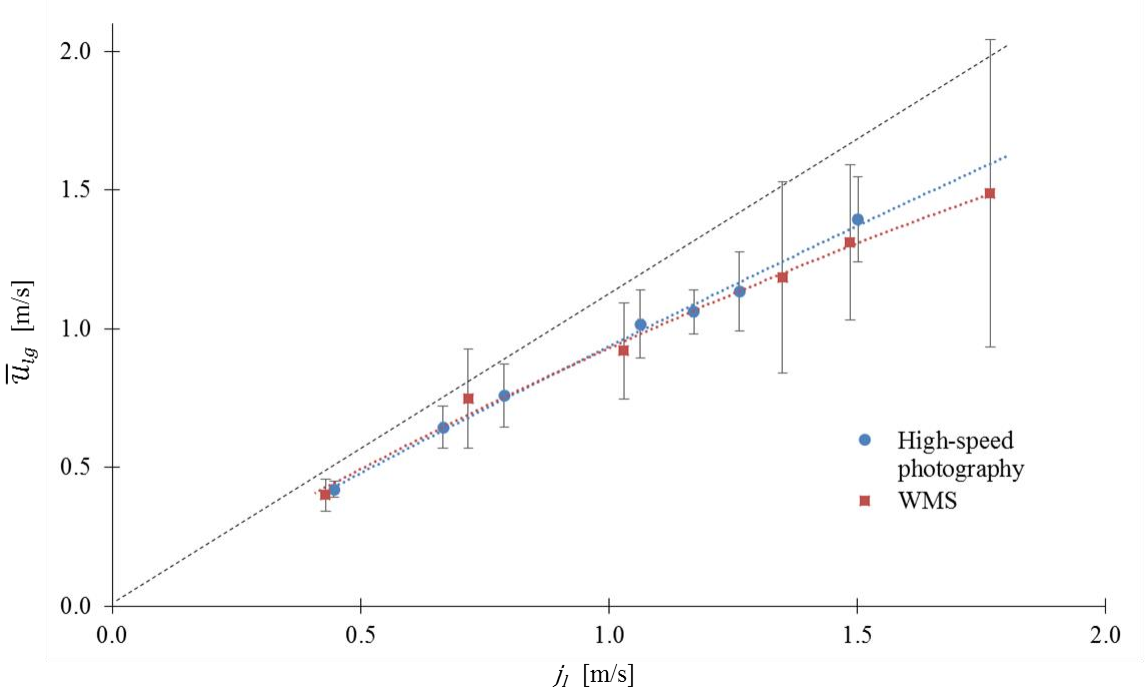

Figure 60: Interfacial velocities measured by high-speed photography vs. WMS measurements in bubbly flow; bars indicate estimated uncertainties

To quantify the differences, second-order polynomials passing through the origin of the axes were fitted to the two sets of measurements (Figure 60). The WMS data were fitted by

$$\overline{u_{lg}}\big|_{wms} \approx -0.115\, j_l^2 + 1.04\, j_l \tag{34}$$

whereas the high-speed photography data were fitted by

$$\overline{u_{lg}}\big|_{hsp} \approx -0.044\, j_l^2 + 0.98\, j_l \tag{35}$$

The relative difference between the two fitted curves

$$e\left(\overline{u_{lg}}\right) = 100\,\frac{\overline{u_{lg}}\big|_{wms} - \overline{u_{lg}}\big|_{hsp}}{\overline{u_{lg}}\big|_{hsp}}\,\% \tag{36}$$

(Figure 61) is slightly positive for small j_l and becomes increasingly negative at larger speeds within the range 0.4 m/s $\leq j_l \leq$ 1.8 m/s.

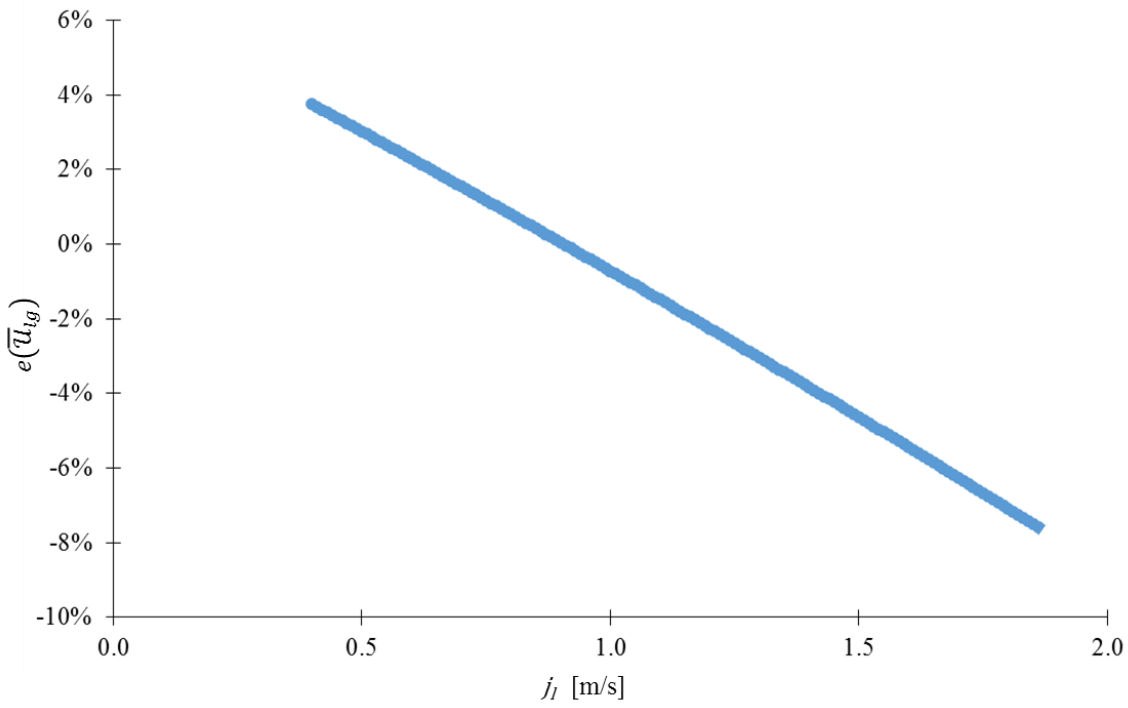

Figure 61: Relative difference between the interfacial velocity measurements by the WMS and high-speed photography

Table 9 and Table 10, respectively, list the average liquid-gas interfacial velocity $\overline{u}_{lg}$, its uncertainty $2\sigma_{\overline{u}_{lg}}$ and the number of distinct interfaces detected, measured by photography and the WMS in the bubbly flow regime. For each set of experiments, the superficial liquid velocity j_l was kept constant.

Table 9: Photographic measurements of interfacial velocity in the bubbly regime

j_l [m/s]	$\overline{u}_{lg}$ [m/s]	$2\sigma_{\overline{u}_{lg}}$ [m/s]	Number of interfaces
0.45	0.420	0.03	6
0.67	0.644	0.08	10
0.79	0.759	0.11	12
1.06	1.016	0.12	27
1.17	1.061	0.08	9
1.26	1.134	0.14	9
1.50	1.42	0.15	8

Table 10: WMS measurements of interfacial velocity in the bubbly regime

j_l [m/s]	$\overline{u}_{lg}$ [m/s]	$2\sigma_{\overline{u}_{lg}}$ [m/s]	Number of interfaces detected
0.43	0.40	0.06	57
0.72	0.75	0.18	151
1.03	0.92	0.17	218
1.35	1.18	0.34	104
1.49	1.31	0.28	100
1.77	1.49	0.56	72

5.3.2 Precision uncertainty

The relative uncertainty $u_{\mathcal{U}}/\mathcal{U}$ of the average interfacial velocity measurements, as estimated in Chapter 4.7.5, is plotted in Figure 62 against the liquid superficial velocity j_l, for various ranges of gas superficial velocities j_g. As a general observation, the relative uncertainty lessens as the liquid or gas superficial velocities increase. For example when $j_l \approx 0.25$ m/s and at low j_g, the uncertainty is around 45%, and decreases as j_g increases. It is important to note that the technique by which these interfacial velocities were measured are expected to become more accurate at moderate and high void fractions, which may further explain the high uncertainty trend. When j_g becomes above 5 m/s, the uncertainty has fallen below 10%. At higher j_l, the spread of the uncertainty lessens and becomes more consistent over the range of j_g over which the measurements were taken.

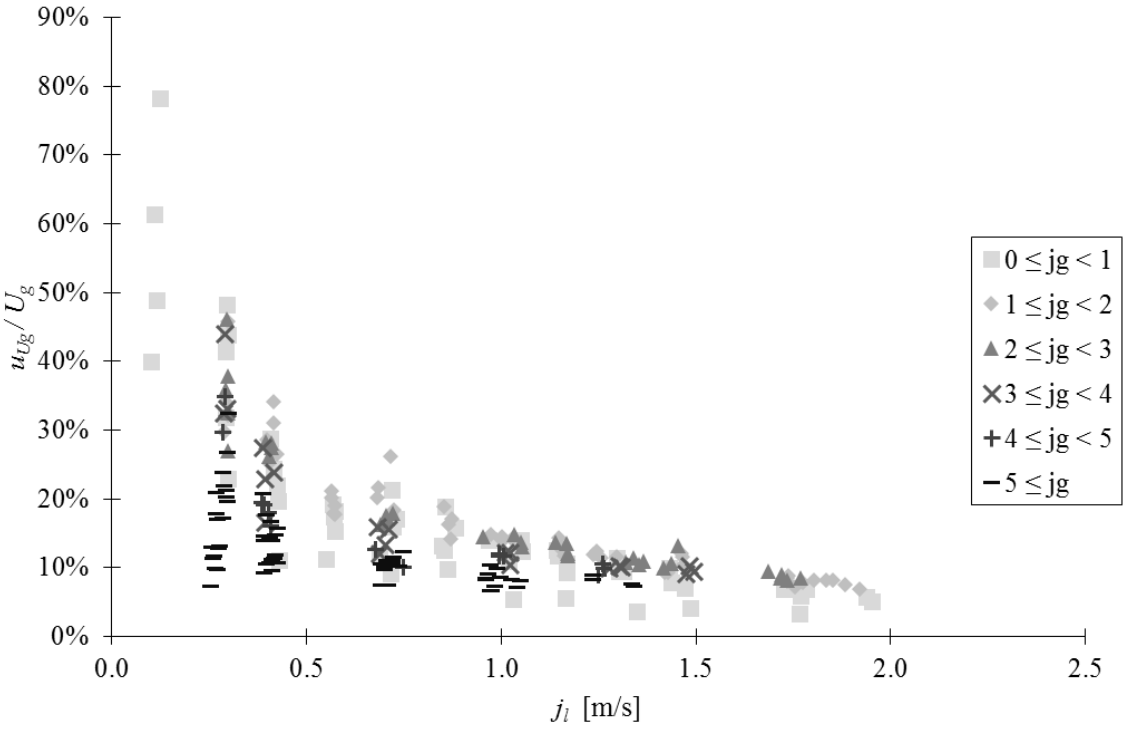

Figure 62: Interfacial velocity relative uncertainty

5.3.3 Variation with superficial velocity

Figure 63 illustrates the dependence of the average interfacial velocity $\mathcal{U}$ from the WMS measurements upon the gas and liquid superficial velocities. At a low total superficial velocity j, the interfacial velocity increases in a linear fashion with the total superficial velocity. This trend is consistent over the entire range of liquid superficial velocities. However, as the gas superficial velocity increases, a notable change occurs, where $\mathcal{U}$ no longer increases at a comparable rate. This is caused by the wavy flow pattern present at these high gas velocities. The WMS measures the interfacial velocity of the flow, but in wavy and stratified flow, the only interface that can be detected becomes the waves at the surface of liquid. Under these circumstances, the WMS no longer measures the average gas velocity.

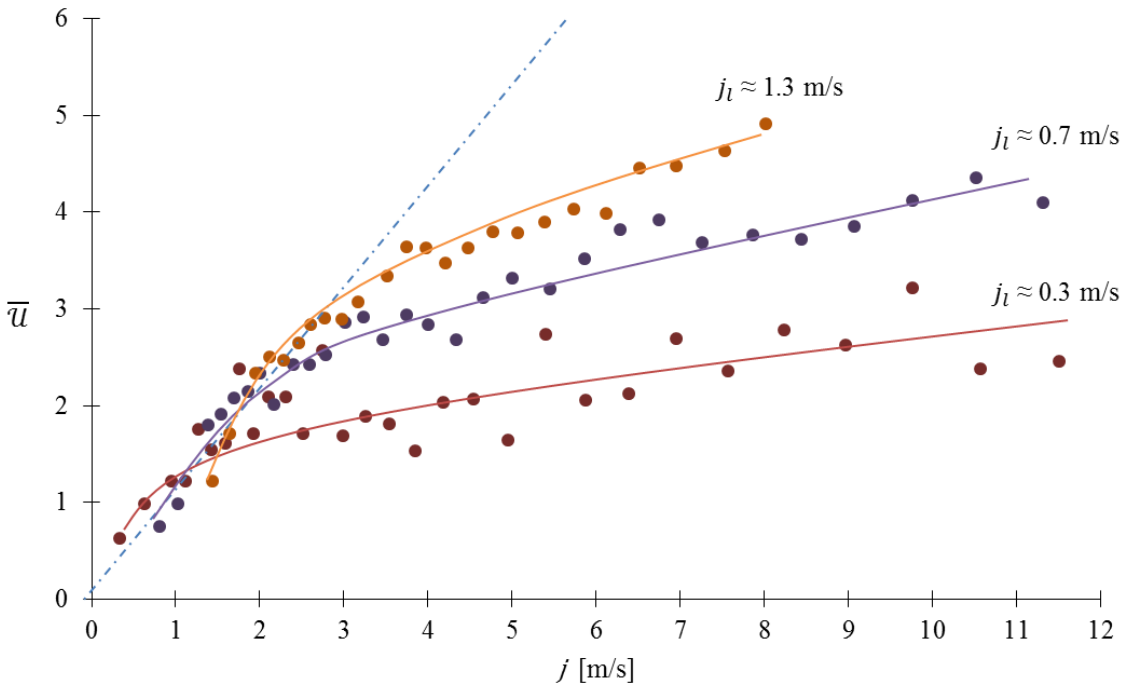

Figure 63: Average interfacial velocity plotted vs. total superficial velocity

The average interfacial velocity, over the length of the test section, does not necessarily correspond to the WMS average interfacial velocity over the distance separating the sensors. In order to assess the effect that the sensors might have on the velocity of the flow, separate velocity measurements were taken with the high-speed camera over the length of pipe upstream, downstream and near the WMS, as shown in Figure 64.

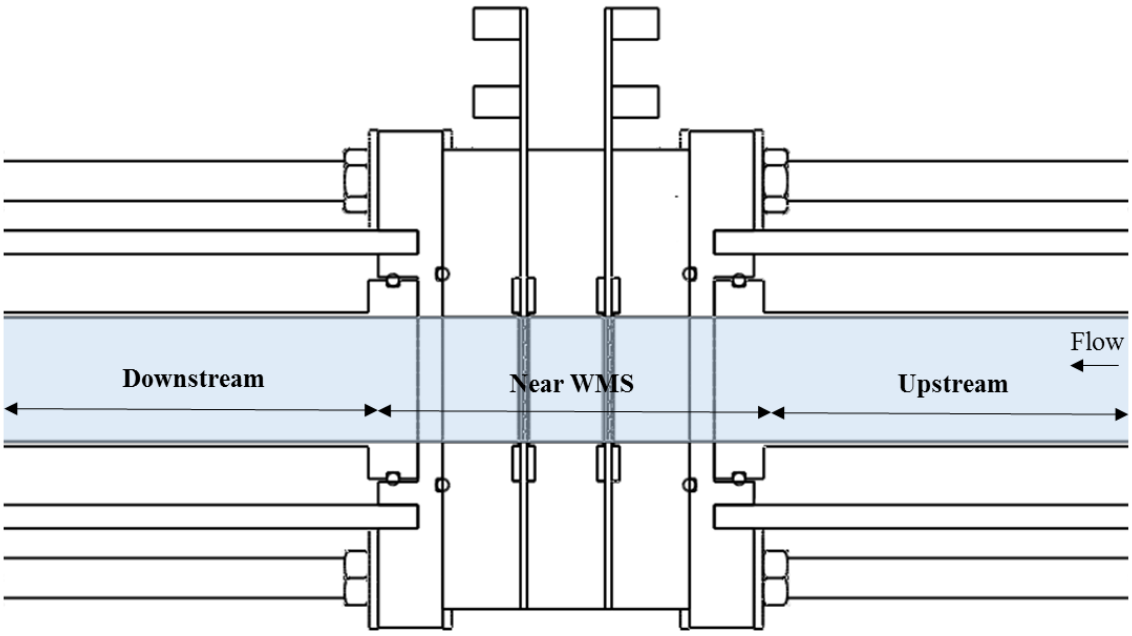

Figure 64: Axial distance ranges for average interfacial velocity comparisons

In Figure 65, for a range of liquid superficial velocities between roughly 0.5 m/s and 1.5 m/s, the upstream velocities are consistently lower than the others. Moreover, they show a strong linear trend with respect to the liquid superficial velocity. Over the distance between the flanges upstream and downstream of the sensors (near-WMS), the velocity increases, suggesting a flow acceleration across the sensor array due to the flow restriction caused by the wires. Once again, the near-WMS velocities measured show a linear trend with respect to j_l. At lower j_l, the downstream velocities happen to coincide fairly closely to the near-WMS velocities, but this trend breaks down at higher j_l where the downstream velocities exceed the near-WMS velocities by a significant margin. The difference between the upstream and downstream velocities grows rapidly as j_l increases.

When j_l= 1.5 m/s, the upstream velocity surpass the downstream one by almost 50%. Hence, the flow obstruction caused by the WMS becomes increasingly significant as the liquid superficial velocity increases.

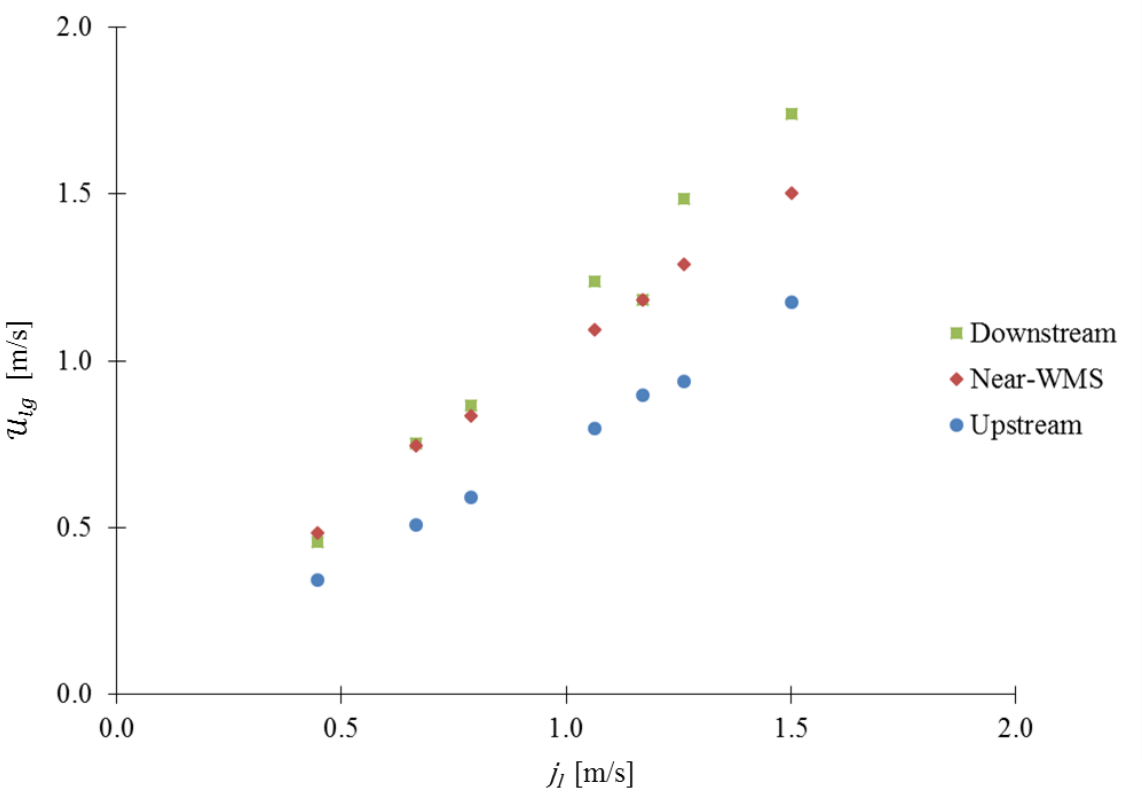

Figure 65: Interfacial velocity variation as measured upstream, downstream and near the WMS

Chapter 6 Development of a drift-flux model

The drift-flux model has been introduced in section 2.4. Its purpose it to provide a linear relationship between the total superficial velocity j of the flow and the void fraction ε. The adjustable parameters appearing in this relationship are the distribution parameter c_0 and the drift velocity v_{gj}.

To estimate the empirical coefficients in the drift-flux model, one may rearrange the terms in equation (7) to express the drift flux model as a the following linear relationship between the ratio j_g/ε and j

$$\frac{j_g}{\varepsilon} = c_0\, j + v_{gj} \tag{37}$$

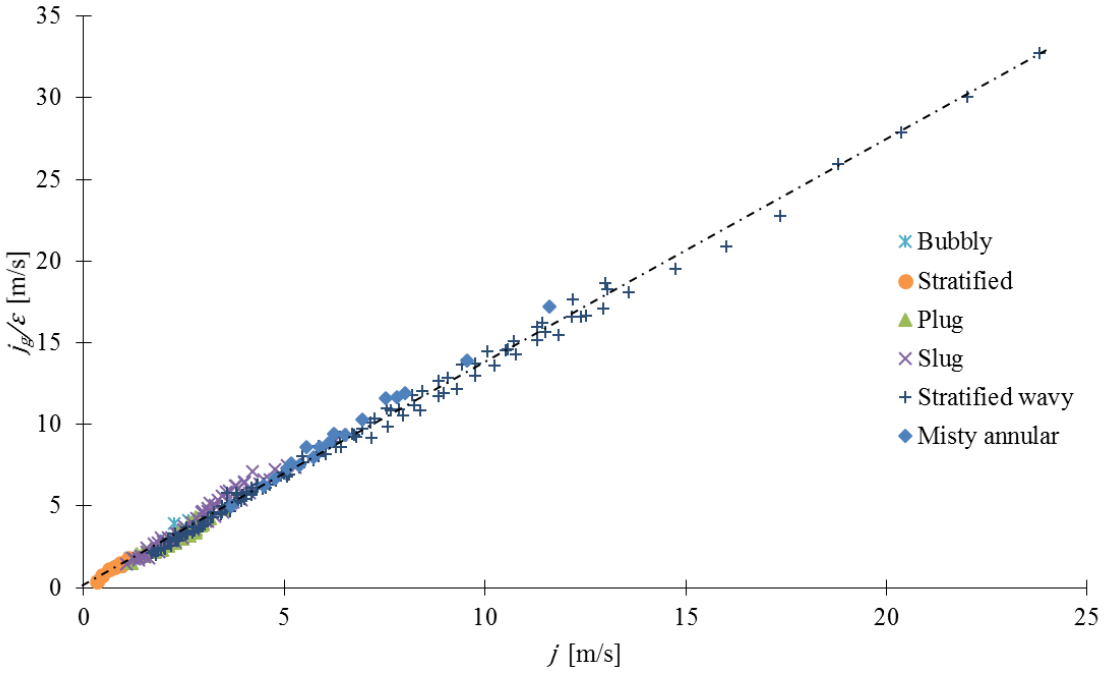

Figure 66: Linear relationship between j and j_g/ε

Figure 66 shows that the full set of data obtained in this work is approximately compatible with this linear relationship over the full range of total superficial velocities and all air-water regimes considered. The linear least squares fit to all data was

$$\frac{j_g}{\varepsilon} = 1.4\, j + 0.13 \tag{38}$$

with an RMS difference of 0.40 m/s. Then, the original expression for the drift-flux model may be written as

$$\varepsilon_{df} = \frac{j_g}{1.4\, j + 0.13} \tag{39}$$

In order to assess the goodness of fit of this model to the measurements, the percent error e_n can be evaluated for each WMS void fraction measurement $\varepsilon_{n,wms}$, as

$$e_n = 100\,\frac{\varepsilon_{n,df} - \varepsilon_{n,wms}}{\varepsilon_{n,wms}}\% \qquad n = 1 \ldots N \tag{40}$$

The average percent error $\overline{e}$ of the void fraction for N measurements is found as

$$\overline{e} = \frac{1}{N}\sum_{n=1}^{N} e_n \tag{41}$$

whereas the RMS error e_{rms} is found as

$$e_{rms} = \sqrt{\frac{1}{N}\sum_{n=1}^{N} e_n^2} \tag{42}$$

The RMS difference and average percent difference between the void fraction measurements and this overall drift-flux model predictions for each regime is shown in Table 11. It is seen that the drift-flux model tends to underestimate systematically the void fraction to various degrees, and that the RMS difference is highest in the low flow rate regimes (stratified, plug) and lowest in the high flow rate regimes (stratified wavy, misty annular).

Table 11: Void fraction average percent and RMS differences for various regimes

Regime	$\overline{e}$	e_{rms}
Stratified	-2.6 %	16.8 %
Plug	-12.1 %	15.5 %
Slug	-4.0 %	10.5 %
Stratified wavy	-6.3 %	8.9 %
Misty annular	-2.1 %	3.9 %

By plotting each individual void fraction percent difference e and identifying them by flow regime in Figure 67, we notice a diminished scatter of the data as the void fraction increases. The misty annular regime stands out as the most consistent and closest to a 0 % difference, while the plug, slug and stratified wavy regimes display the greatest scatters, as observed by their RMS difference. The stratified regime has the fewest data points and as a result does not seem to follow any noticeable trend.

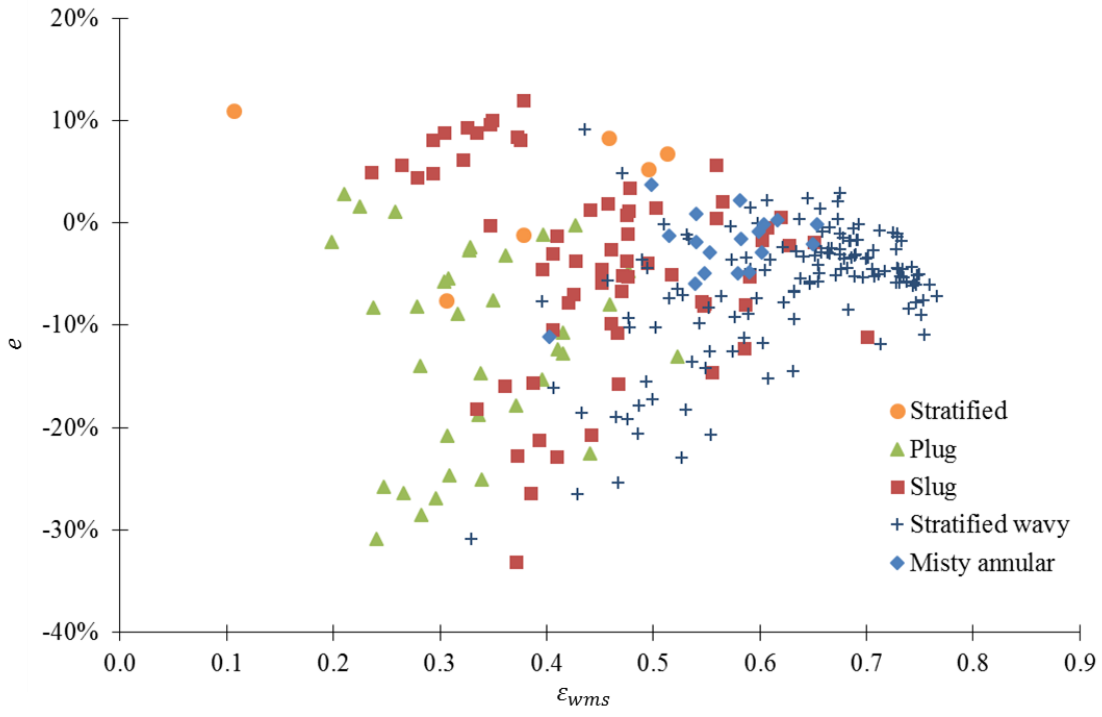

Figure 67: Percent difference based on flow regime

Drift-flux models were also fitted to the data in each regime separately, and the void fractions were compared to the measurements. The corresponding parameters c_0 and v_{gj}, along with the average and RMS differences between the measured and predicted void fractions are listed in Table 12. The numbers of data points corresponding to each regime, also shown in the table, varied significantly, which implies that the coefficients of the overall drift-flux model would be biased towards regimes represented by a large number of data points. Bubbly flow results are not shown in this table, as the accuracy of void fraction by the available WMS was deemed to be fairly low.

Table 12: Estimated values of the two drift-flux model parameters fitted to data in each flow regime and associated average percent and RMS differences

Regime	c_0	v_{gj}	$\bar{e}$	e_{rms}	# of data points
Stratified	1.7	-0.07	-1.0 %	9.7 %	7
Plug	1.3	0.01	-4.9 %	9.6 %	35
Slug	1.5	-0.25	-5.0 %	9.1 %	66
Stratified wavy	1.4	0.02	-3.1 %	5.8 %	135
Misty annular	1.5	-0.50	-6.7 %	7.1 %	18

As a comparison example, for horizontal turbulent slug flow, the following relationship was proposed (Armand, 1946)

$$\varepsilon = 0.833\, j_g/j \tag{43}$$

Re-arranging this equation following the previous format yields a distribution parameter $c_0 = 1.2$ and a drift velocity $v_{gj} = 0$.

$$\frac{j_g}{\varepsilon} = 1.2\, j \tag{44}$$

The experimental results exceed this value with a distribution parameter of 1.5, while the drift velocity is slightly underestimated. Similar parameters are proposed for elongated bubble flow (Collier, 1994). Comparing the plug (elongated bubble) flow experimental results to this proposed model, we do see a very close match for either parameter. The drift-flux parameters for each group of measurements taken at a

roughly constant liquid superficial velocity j_l were also measured and are listed in Table 13, in ascending order. The flow regimes that were the most often observed in each of these measurement groups are indicated. The plots from which these constants were derived are available in Appendix F. The average percent and RMS differences following these drift-flux parameters are found to be significantly lower than based on the parameters obtained by flow regime grouping.

Table 13: Experimental drift-flux constants based on measurements at constant liquid superficial velocity, and associated average percent and RMS differences

Test #	Dominant flow regimes	j_l [m/s]	c_0	v_{gj} [m/s]	$\overline{e}$	e_{rms}	# of data points
93 - 129	Slug, Strat. wavy	0.28	1.3	0.24	-1.2 %	1.7 %	37
137 - 173	Strat. wavy	0.40	1.3	0.13	-0.7 %	1.1 %	37
9 - 17	Plug, Slug	0.57	1.2	0.47	-3.2 %	3.4 %	9
177 - 206	Strat. wavy	0.71	1.4	-0.15	-0.7 %	0.7 %	30
20 - 26	Plug, Slug	0.86	1.4	0.04	-1.5 %	1.5 %	7
210 - 239	Strat. wavy	1.00	1.4	-0.36	-0.8 %	0.8 %	30
29 - 40	Plug, Slug	1.16	1.6	-0.46	-1.4 %	1.5 %	14
245 - 266	Strat. wavy, Annular misty	1.29	1.5	-0.74	-0.6 %	0.6 %	22
46 - 59	Slug	1.45	1.5	-0.37	-0.6 %	0.7 %	14
270 - 286	Plug	1.57	1.6	-1.05	-0.4 %	0.5 %	17
62 - 71	Slug	1.74	1.8	-0.97	-0.6 %	0.7 %	10
74 - 82	Slug	1.85	1.8	-0.94	-0.7 %	0.8 %	9
290 - 296	Plug, Slug	1.88	1.7	-1.6	-0.2 %	0.5 %	7

Figure 68 shows the fitted lines for different values of j_l. As j_l is increased, it is clear that c_0 increases monotonically, whereas v_{gj} decreases. These trends are consistent with those found by França (França and Lahey, 1992).

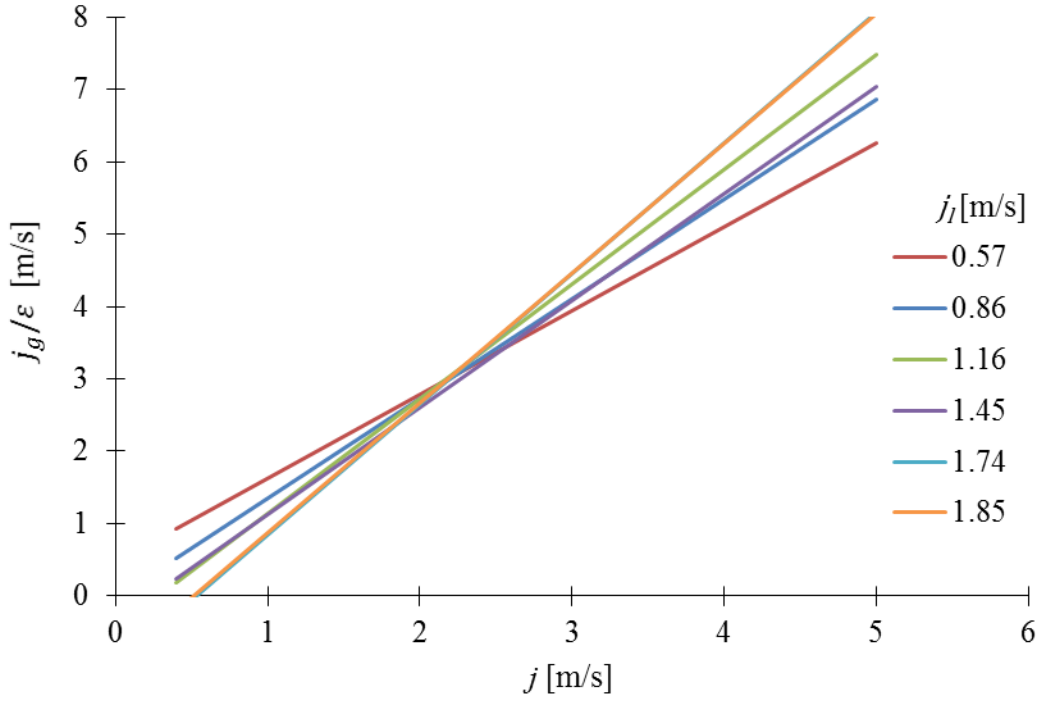

Figure 68: Drift-flux linear profiles at various liquid superficial velocities

Chapter 7 Conclusions and recommendations for future work

7.1 Conclusions

This research has been motivated by the current need in the industry for reliable prediction and measurement methods for two-phase flows in header/feeder systems. As a contribution to address this issue, an air-water flow loop was designed to allow void fraction and interfacial velocity measurements in horizontal flows using wire-mesh sensors and high-speed photography. In order to obtain fully-developed flow in the test section on a consistent and repeatable fashion, a long development section and a head tank to maintain constant head pressure were used. The flow loop was able to successfully reproduce a wide range of horizontal flow regimes of interest, except for annular flow due to the water flow rate limitations.

Void fraction measurements by two sensors, one positioned downstream of the other, were found to be in good agreement at high gas and liquid superficial velocities, but differed significantly at low superficial velocities. For this reason, all reported void fraction measurements were taken with the upstream sensor, which is exposed to a flow that is less disturbed by the intrusion of the device than its downstream counterpart. Void fraction measurements were also found to depend on the technique used to calibrate the WMS. The time-averaged calibration technique was found to be more reliable than the histogram calibration technique when taking measurements over a range of different regimes.

Interfacial velocity measurements using a pair of wire-mesh sensors were found to be fairly accurate in bubbly, slug and plug flows, but not in stratified, wavy and annular flows, in which many nodes of the sensor were never or seldom crossed by the air-water interface. Average interfacial velocity measurements obtained by photography at low void fractions were in good agreement with those from the WMS. The uncertainties of both methods increased with increasing liquid velocity.

The drift-flux models are based on the linear relationship between j_g/ε and j. Parameters were proposed based on the overall population of measurements, by flow regime grouping and finally liquid superficial velocity grouping, and the average and RMS percent differences were determined. When comparing the WMS void fraction measurements to the linear least squares fit of the overall population of measurements and by flow regime grouping, the drift-flux parameters followed linear trends with significant scatter of the data. The parameter c_0, which corresponds to the slope in such plots, generally increased as the liquid superficial velocity j_l increased. As a result, when combining measurements by flow regime, a fairly large RMS difference was observed. The drift velocity parameter v_{gj}, which physically represents the relative velocity between the air and the water, generally decreased as the liquid superficial velocity increased. On the other hand, a strong linear relationship with relatively small errors was observed when considering the groups of measurements taken at a constant liquid superficial velocity j_l. These observations suggest that the drift-flux parameters c_0 and v_{gj} would be sensitive to the liquid superficial velocity, and that drift-flux models based solely on flow regime would not be sufficient to accurately predict the void fraction.

7.2 Recommendations for future work

The flow loop described in Chapter 3.1 was designed and built with a head tank meant to maintain a constant head with respect to the test section, and to dampen the motions induced by the centrifugal pump within the fluid. The room ceiling limited the elevation at which the head tank could be installed and the maximum water flow rate that could be achieved by the maximum tank head. Although misty-annular flow patterns were observed, they were highly eccentric. In order to obtain a more uniform water layer across the circumference of the inner pipe in annular flow, one should either use a test section with a smaller inner diameter, or connect the test section directly to a sufficiently large pump, therefore eliminating the head tank.

The air injector located at the inlet of a relatively long development section (97 *D*) of the pipe was designed to provide a uniform dispersion of the air. Under most flow

regimes, the air rapidly rose to the top of the channel and the flow regimes developed to their final state relatively close (10-20*D*) to the injector. Because the injector used in this work produced relatively large bubbles at the inlet and the water flow rate was limited by an upper bound, bubbly flows with small distributed bubbles could not be sustained. The use of an air diffuser with a finer mesh would produce smaller bubbles, which would be more likely to follow the water flow rather than rise to the top. Modifying the system to permit higher water flow rates would also help in generating bubbly flows.

Replacement of the present 8×8 WMS by 16×16 ones for the same pipe diameter would provide an improved spatial resolution, thus reducing the uncertainty of the void fraction measurements. On the other hand, this would also cause a larger flow obstruction and possibly an increase in the uncertainty of interfacial velocity measurements. A comparison of the performance of the two sensors would be necessary to identify the optimal choice. In addition, void fraction measurements by WMS should be compared to those by a more accurate method, as for example the quick-closing valve method.

The void fraction measurements were based on procedures by the sensor manufacturer. It appears that, in some cases, these procedures could be improved. For example, some special filtering of the signal could be performed whenever the node occasionally measures intermediate values of void fractions (i.e., it is close to neither 0 or 1).

The procedure for measuring the interfacial velocity from the WMS recordings can potentially provide erroneous results if care is not taken in its interpretation. Because the velocity profile of the flow is different near the centre of the channel than near its edges, it is important to process the data on a node-to-node basis in order to obtain correct results. Moreover, the WMS cannot take into account the fact that bubbles may break down and coalesce, and as a result it may associate interfaces which do not belong to the same bubble. To account for this, the program used for this analysis set restrictive boundaries to the range of valid velocities that could be measured, and rules that dictated which results could be considered valid and which ought to be discarded. This approach can be further improved. The interfacial velocity measurements were taken with a 20 mm nominal spacing between the measurement planes. This spacing can be optimized to

improve measurement accuracy. The experiments presented in this report were also performed under a fixed tube diameter. Future investigations would be of interest to account for the effect that the tube diameter has on the flow regimes and their transitional areas.

Analysis of the bubble numbers and size distributions measured by the downstream and upstream sensors in various flow regimes would yield additional insight into the effect that the wires might have on the bubbles as they cross the measurement planes of the sensors.

References

Armand, A. A. (1946), "The resistance during the movement of a two-phase system in horizontal pipes". *Izvestia Vses. Teplo. Inst.* (1), 16-23. AERE-Lib/Trans 828.

Balachandar, S. and Eaton, J. K. (2010). "Turbulent Dispersed Multiphase Flow", *Ann. Rev. Fluid Mech.* **42**, 111–33.

Collier, J. G. and Thome, J. R. (1994). *Convective Boiling and Condensation*. Oxford University Press, New York, USA.

Crowe, C. T. (2006). *Multi-phase Flow Handbook*. CRC Press, Taylor & Francis, Boca Raton, Florida, USA.

França, F. and Lahey Jr., R. T. (1992). "The use of drift-flux techniques for the analysis of horizontal two-phase flows". *Int. J. Multiphase Flow* **18 (6)**, 787-801.

Helmholtz-Zentrum Dresden-Rossendorf. Official website: http://www.hzdr.de

Key Intruments Flowmeter sizing. http://www.keyinstruments.com/technical-support/flow-meter-sizing

Kleinstreuer, C. (2003). *Two-Phase Flow: Theory and Applications*. Taylor & Francis, New York, USA.

Mandhane, J.M., Gregory, G.A. & Aziz, K. (1974), "A flow pattern map for gas-liquid flow in horizontal pipes", *Int. J. Multiphase Flow* **1**, 537- 53.

Omega Canada. Official website: www.omega.ca

PCO (2011), *Pco.edge scientific CMOS camera*, v 1.04, Cooke Corporation, Romulus, Michigan, USA.

Pietruske, H., and Prasser, H.-M. (2007), "Wire-mesh sensors for high-resolving two-phase flow studies at high pressures and temperatures", *Flow Meas. Instrum.* **18**, 87-94.

Prasser, H.-M., Böttger, A., and Zschau, J. (1998), "A New Electrode-Mesh Tomograph for Gas-Liquid Flows", *Flow Meas. Instrum.* **9**, 111-119.

Prasser, H.-M., Zschau, J., Peters, D., Pietzsch, G., Taubert, W., Trepte, M. (2000), "Wire-mesh sensor – now 10,000 frames per second", *Annual Report 1999*, Institute of Safety Research, FZR-284, Feb. 2000, ISSN 1437-322X, 15-18.

Prasser, H.-M., Scholz, D. and Zippe, C. (2001a), "Bubble size measurement using wire-mesh sensors", *Flow Meas. Instrum.* **12**, 299-312.

Prasser, H.-M., Krepper, E., Lucas, D., Zschau, J., Peters D., Pietzsch, G., Taubert, W., Trepte, M. (2001b), "Fast Wire-Mesh Sensors for Gas-Liquid Flows and Decomposition of Gas Fraction Profiles according to Bubble Size Classes", in *Experimental Heat Transfer Fluid Mechanics and Thermodynamics World Conference*, Thessaloniki, Greece, **2**, 1135-1140.

Shaban, H. (2013), "Experimental and numerical studies of gas-liquid flows in models of nuclear reactor header/feeder systems", Ph.D. Thesis Proposal, Department of Mechanical Engineering, University of Ottawa, Ottawa, Canada

Sharaf, S., Da Silva, M., Hampel, U., Zippe, C., Beyer, M. and Azzopardi, B. (2011), "Comparison between wire mesh sensor and gamma densitometry void measurements in two-phase flows", Meas. Sci. Technol. **22**, 104019.

Tavoularis, S. (2005). *Measurement in Fluid Mechanics*. Cambridge University Press, New York, USA.

Teletronic Rossendorf GmbH (2008), *Wire Mesh System WMS 200*, Radeberg, Germany, September 2008.

Teletronic Rossendorf GmbH (2009), *Wire-Mesh-System WMS 200 Specification*, Version 1.03, Radeberg, Germany, November 26 2009.

Teletronic Rossendorf GmbH (2010), *Wire Mesh Sensor System WMS 200 Manual*, Version 1.2, Radeberg, Germany, December 9 2010.

Thome, J. R. (2004). *Engineering Data Book III*. Wolverine Tube Inc., Lausanne, Switzerland.

Yang, J. (2013), *Header Test Facility*, Thermalhydraulics Branch, Chalk River Laboratories, Atomic Energy of Canada Ltd., June 19th 2013.

Zuber, N. and Findlay, J. A. (1965), "Average Volumetric Concentration in Two-Phase Flow Systems", *J. Heat Transfer* **87**, 453-468.

Appendix A Flowmeter calibration

A1 Water flowmeter calibration

The water flowmeter was calibrated using a 100 liter container and a handheld stopwatch. The calibration tests for the water flow-meter are plotted in Figure A1.

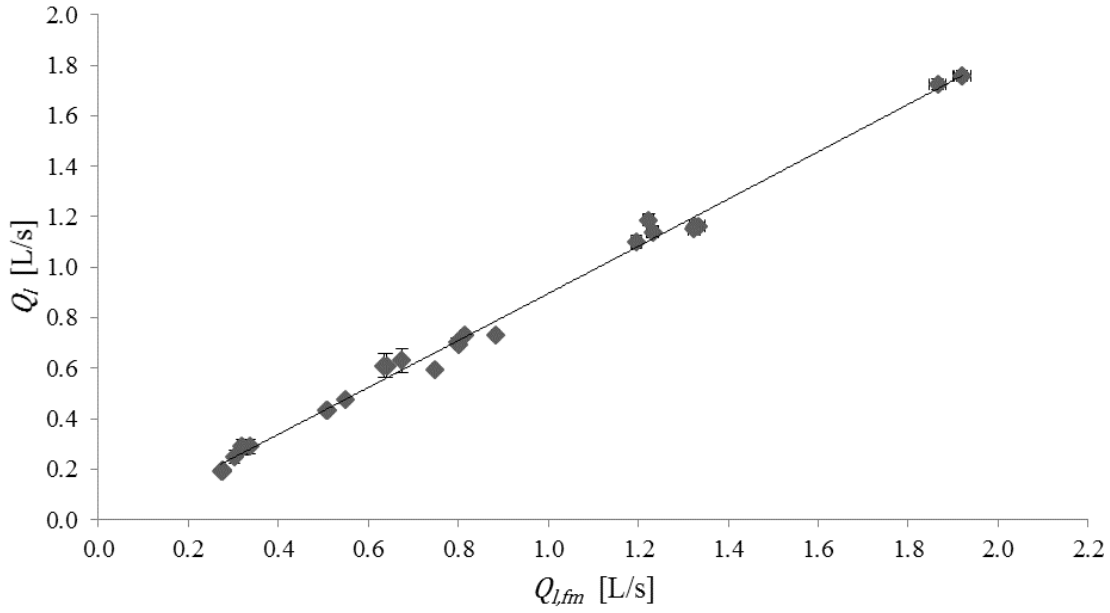

Figure A1: Water flowmeter flow rate correction curve based on experimental calibration

All volume flow rates (and incidentally, the resulting velocities) in this report were adjusted based on this calibration following a second-order polynomial trend-line as

$$Q_l = 5.1 * 10^{-3} * Q_{l,fm}^2 + 0.9226 * Q_{l,fm} - 0.032 \qquad \text{(A1)}$$

where Q_l is the measured volume flow rate of water and $Q_{l,fm}$ is the displayed flow rate by the flowmeter (in liters per second). Table A1 summarizes the calibration tests that were performed, along with their respective uncertainties. The uncertainties of the measured volume and time measurements are 0.25 L and 1 s respectively.

Table A1: Water flowmeter calibration data

Test #	$Q_{l,fm}$ [L/s]	Measured volume [L]	t [s]	Q_l [L/s]	u_{Ql} [L/s]
1	0.303	18.9	76	0.249	0.019
2	0.337	18.9	65	0.291	0.020
3	0.322	18.9	66	0.287	0.020
4	0.318	18.9	65	0.291	0.020
5	0.675	18.9	30	0.631	0.036
6	0.641	18.9	31	0.610	0.035
7	0.635	18.9	31	0.610	0.035
8	0.277	56.5	286	0.198	0.006
9	0.273	57.0	296	0.193	0.006
10	0.275	57.0	294	0.194	0.006
11	0.549	57.0	120	0.475	0.009
12	0.507	57.0	131	0.435	0.009
13	0.511	57.0	132	0.432	0.009
14	0.797	57.0	81	0.704	0.013
15	0.801	57.0	82	0.695	0.013
16	0.814	57.0	78	0.731	0.014
17	1.22	57.0	48	1.19	0.021
18	1.23	57.0	50	1.14	0.020
19	1.20	55.0	50	1.10	0.021
20	0.884	96.6	132	0.732	0.008
21	0.748	96.6	162	0.596	0.007
22	1.33	96.6	83	1.16	0.012
23	1.33	96.6	83	1.16	0.012
24	1.32	96.6	84	1.15	0.012
25	1.87	96.6	56	1.73	0.018
26	1.92	96.6	55	1.76	0.018
27	1.92	96.6	55	1.76	0.018

A2 Air flow rate corrections

The calibration pressure measurements taken for the air rotameter are shown in the Table A2, where p_{rot} corresponds to the pressure measured at the rotameter's inlet and p corresponds to the pressure measured inside the test section. All pressures shown in this table are absolute pressures.

Table A2: Pressure measurements for air flow rate correction

Backpressure [kPa]	Q_l [L/s]	Q_g [L/s]	p_{rot} [kPa]	p [kPa]
203	0.50	0.38	128.6	113.7
203	0.50	0.66	129.6	111.7
203	0.50	0.94	135.5	109.9
203	1.01	0.38	133.0	115.1
203	1.01	0.66	136.1	115.1
203	1.01	0.94	142.0	115.5
203	1.01	1.23	149.2	116.5
203	1.01	1.51	156.5	118.2
203	1.51	0.38	142.0	119.3
203	1.51	0.66	147.9	121.3
203	1.51	0.94	151.7	122.4
203	1.51	1.23	159.9	123.0
203	0.25	0.38	128.2	108.2
203	0.25	0.66	128.9	108.2
203	0.25	0.94	134.1	107.9
203	0.25	1.42	142.3	108.6
203	0.25	1.89	155.8	109.6
203	0.25	2.36	178.5	108.9
203	0.25	2.83	212.3	108.9
203	0.25	3.30	259.9	108.6
405	0.63	0.38	130.3	110.3
405	0.63	0.66	133.0	111.0
405	0.63	0.94	137.9	111.7
405	0.63	1.42	148.2	114.1
405	0.63	1.89	162.0	115.1
405	0.63	2.36	184.1	115.5
405	0.63	2.83	221.3	117.9
405	1.39	0.38	141.0	116.5
405	1.39	0.66	144.8	120.6
405	1.39	0.94	150.3	121.7
405	1.39	1.42	163.4	122.7
405	1.39	1.89	178.5	125.5
405	0.50	0.38	128.6	108.6
405	0.50	0.66	131.7	108.9
405	0.50	0.94	135.8	109.6
405	1.01	0.38	133.7	114.1
405	1.01	0.66	137.2	114.4
405	1.01	0.94	142.7	114.8
405	1.01	1.51	156.5	116.5

Backpressure [kPa]	Q_l [L/s]	Q_g [L/s]	p_{rot} [kPa]	p [kPa]
405	1.01	2.08	176.8	119.3
405	1.01	2.64	212.3	121.3
405	1.51	0.38	142.3	117.9
405	1.51	0.66	146.8	121.7
405	1.51	0.94	153.0	122.0
405	1.51	1.23	158.6	123.4

A polynomial regression was applied to each set for interpolation purposes. The constants presented in Table A3 were used to determine the gage pressures p_{rot} and p as a function of the gas volume flow rate Q_g (expressed in L/s) according to the following equations.

$$\begin{cases} p_{rot} = C_1 \cdot Q_g^2 + C_2 \cdot Q_g + C_3 \\ p = C_4 \cdot Q_g^2 + C_5 \cdot Q_g + C_6 \end{cases} \quad \text{(A2)}$$

Table A3: Pressure interpolation constants

Backpressure [kPa]	Q_l [L/s]	C_1	C_2	C_3	C_4	C_5	C_6
203	0.51	30.1	-27.7	135	2.15	-9.55	116
203	1.01	8.69	4.77	130	3.70	-4.31	116
203	1.51	7.32	8.52	138	-4.31	11.3	116
203	0.25	18.6	-25.4	138	-0.32	1.42	107
405	0.63	15.5	-14.5	135	-0.13	3.41	109
405	1.39	8.22	6.48	137	-2.37	10.5	114
405	0.51	6.46	4.25	126	2.15	-1.02	109
405	1.01	13.4	-6.74	135	-0.13	3.41	109
405	1.51	3.01	14.5	136	-7.51	18.0	112

The plots for these pressure measurements and their corresponding quadratic regression curves are shown below.

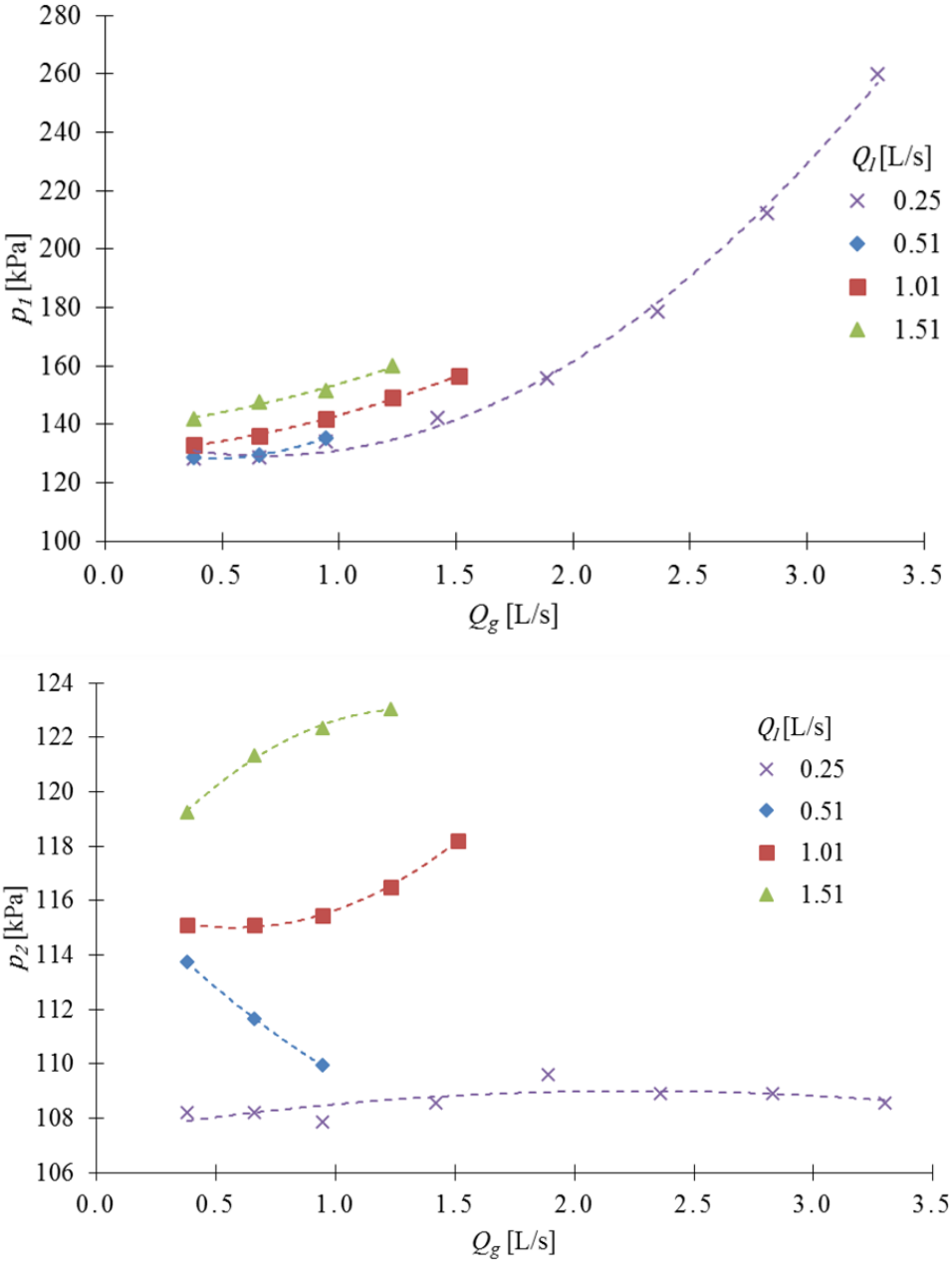

Figure A2: Air flow-meter calibration curves at 203 kPa backpressure

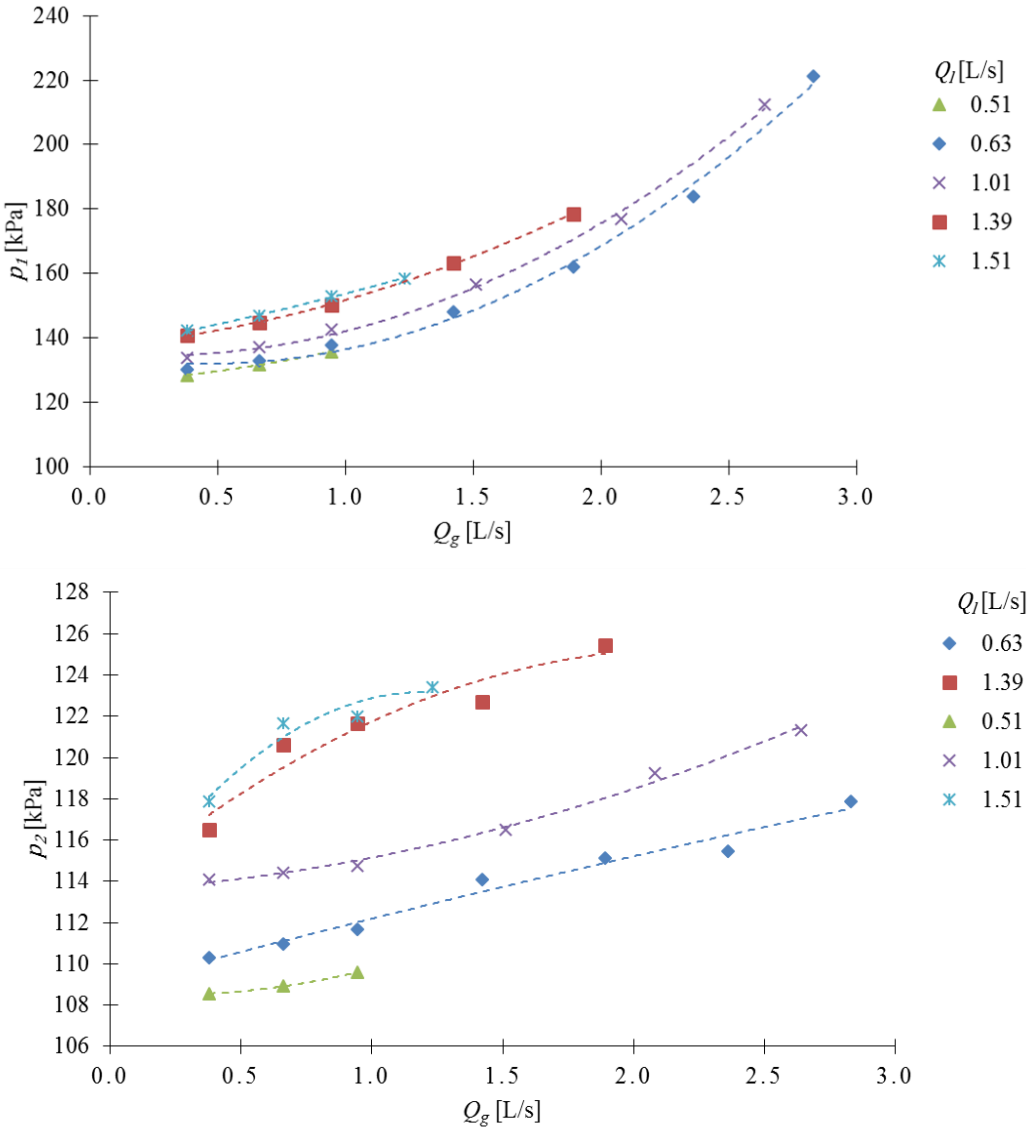

Figure A3: Air flow-meter calibration curves at 405 kPa backpressure

Appendix B Programming code

This programs decodes the data output of the WMS into a readable format. Post-processing of the information is then performed. This code was run in Matlab R2012a version 7.14.0.739.

Main code

```
% Main decryption code wms_data_analyzer.m
fprintf('Clearing memory.');
clear
load variablesave;
filerow=17; %File number to be opened

while filerow<18 % range: 2-303
save('variablesave','datfilematrix','filerow','nij1','nUilecumul','nUit
ecumul','relative_area','Ugij','validnode','Fijdkmax1','cornercut');
clear
fprintf('\nMemory cleared.\n');
load variablesave; % Load variables

% dat file selector
filename='C:\datfiles\37_0004.dat';calibfilename='C:\datfiles\37_0006.d
at';filename(17)=num2str(datfilematrix(filerow,1));filename(18)=num2str
(datfilematrix(filerow,2));filename(19)=num2str(datfilematrix(filerow,3
));calibfilename(17)=num2str(datfilematrix(filerow,4));calibfilename(18
)=num2str(datfilematrix(filerow,5));calibfilename(19)=num2str(datfilema
trix(filerow,6));

fprintf('--------------------\nDefining variables: ');
fid=fopen(filename,'r');
A=fread(fid,'short');
n=1; R=16; C=16; Nframes=length(A)/(R*C); f_meas=10000; % counter, row,
column, total frames numbers & measurement frequency
T=Nframes;  % NUMBER OF FRAMES TO BE CONVERTED
fprintf('done.\nAnalyzing %d out of %d frames of %s
(filerow=%.0f)\n',T,Nframes,filename,filerow);

fprintf('Import dat file to matrix M: ');
for k=1:T
    for i=1:R
        for j=1:C
            M(i,j,k)=A(n);
            n=n+1;
        end
    end
end
status = fclose(fid);
clearvars n;
fprintf('file imported.\n');

fprintf('Post-processing data: ');
```

```
for k=1:T
    for j=1:8
        for i=1:8
            wms1(j,9-i,k)=M(i,j,k);%wms1(i,j,k)=M(i,j,k);%% Extract
WMS1 matrix, corrected for orientation (90 deg cw)
            wms2(17-(i+8),(j+8)-8,k)=M(i+8,j+8,k);%% Extract WMS2
matrix, corrected for orientation (180 deg and mirrored)
            %wms2(9-i,9-j,k)=M(i+8,j+8,k);
        end
    end
end
clearvars M A; %free memory
fprintf('done.\n');

% Calibration file import
fid=fopen(calibfilename,'r');
A=fread(fid,'short');
n=1; Nframescalib=length(A)/(R*C);Tcalib=Nframescalib;
fprintf('Calibration: Convert %s to Mcalib (%d out of %d frames):
',calibfilename, Tcalib, Nframescalib);
for k=1:Nframescalib
    for j=1:C
        for i=1:R
            Mcalib(j,i,k)=A(n);
            n=n+1;
        end
    end
end
status = fclose(fid);
clearvars n;
fprintf('done\n');

fprintf('Post-processing calibration data: ');
for k=1:Tcalib
    for j=1:8
        for i=1:8
            wms1calib(j,9-i,k)=Mcalib(i,j,k);% Extract WMS1calib matrix
            wms2calib(17-(i+8),(j+8)-8,k)=Mcalib(i+8,j+8,k);% Extract
WMS2calib matrix, corrected for orientation
        end
    end
end
clearvars Mcalib A; %free memory
fprintf('done.\n');

fprintf('Histogram calibration: ');
wms1calibavg2(1:8,1:8)=zeros; calibagreement1(1:8,1:8)=zeros;
calibagreement1avg=0; %Initialize
for i=1:8 %WMS1
    for j=1:8
        %Initialize
        freqbin(1:5000)=zeros;
        maxfreq=0;
        zerosignal=0;
        % Fill bins
        for k=1:T
```

```
            if wms1(i,j,k)>0

freqbin(ceil(wms1(i,j,k)))=freqbin(ceil(wms1(i,j,k)))+1;
            else
                zerosignal=zerosignal+1;
            end
        end
        %fprintf('No signal= %d at %d , %d\n',zerosignal, i, j);
        % Find maximum
        for n=1800:5000 % 1800 is arbitrary
            if freqbin(n)>=maxfreq
                wms1calibavg2(i,j)=n;
                maxfreq=freqbin(n);
            end
        end
    end
end
wms2calibavg2(1:8,1:8)=zeros; calibagreement2(1:8,1:8)=zeros;
calibagreement2avg=0; % Initialize
for i=1:8 %WMS2
    for j=1:8
        %Initialize
        freqbin(1:5000)=zeros;
        maxfreq=0;
        zerosignal=0;
        % Fill bins
        for k=1:T
            if wms2(i,j,k)>0

freqbin(ceil(wms2(i,j,k)))=freqbin(ceil(wms2(i,j,k)))+1;
            else
                zerosignal=zerosignal+1;
            end
        end
        %fprintf('No signal= %d at %d , %d\n',zerosignal, i, j);
        % Find maximum
        for n=1800:5000 % 1800 is arbitrary
            if freqbin(n)>=maxfreq
                wms2calibavg2(i,j)=n;
                maxfreq=freqbin(n);
            end
        end
    end
end

clearvars freqbin maxfreq n;
fprintf('done.\nNo signal WARNING: %d.\n',zerosignal);

fprintf('Average signal processing: ');
for j=1:8
        for i=1:8
            % Time-averaged voltage signal per node
            wms1avg(i,j)=mean(wms1(i,j,:));
            wms2avg(i,j)=mean(wms2(i,j,:));
            wms1calibavg(i,j)=mean(wms1calib(i,j,:));
            wms2calibavg(i,j)=mean(wms2calib(i,j,:));
```

```
            % Time-averaged void fractions per node
            wms1avg_ivf(i,j)=1-wms1avg(i,j)/wms1calibavg(i,j);
            wms2avg_ivf(i,j)=1-wms2avg(i,j)/wms2calibavg(i,j);
            wms1avg_ivf2(i,j)=1-wms1avg(i,j)/wms1calibavg2(i,j);
            wms2avg_ivf2(i,j)=1-wms2avg(i,j)/wms2calibavg2(i,j);
        end
end
fprintf ('done.\n');

fprintf('Computing instantaneous void fraction: ');
for k=1:T
    for j=1:8
        for i=1:8
            % Instant void fractions
            wms1_ivf(i,j,k)=1-wms1(i,j,k)/wms1calibavg(i,j);
            wms2_ivf(i,j,k)=1-wms2(i,j,k)/wms2calibavg(i,j);
            wms1_ivf2(i,j,k)=1-wms1(i,j,k)/wms1calibavg2(i,j);
            wms2_ivf2(i,j,k)=1-wms2(i,j,k)/wms2calibavg2(i,j);
        end
    end
end
fprintf('done. \n');

%Calibration agreement
% fprintf('Calibration methods agreement analysis: ');  %TO FIX
% calibagreement1avg=0; calibagreement2avg=0; % Initialize
% for i=1:8
%     for j=1:8
%         %fprintf('WARNING!: SUSPICIOUS CALIBRATION VALUE AT %d
%d\n',i,j);
%         calibagreement1(i,j)=wms1calibavg2(i,j)-wms1calibavg(i,j);
%
calibagreement1avg=calibagreement1avg+calibagreement1(i,j)*relative_are
a(i,j);
%         %fprintf('WARNING!: SUSPICIOUS CALIBRATION VALUE AT %d
%d\n',i,j);
%         calibagreement2(i,j)=(wms2calibavg2(i,j)-wms2calibavg(i,j));
%
calibagreement2avg=calibagreement2avg+calibagreement2(i,j)*relative_are
a(i,j);
%     end
% end
% fprintf('done.\n');

fprintf('Computing average void fraction: ');
ivf1=0;ivf2=0;ivf12=0;ivf22=0;  %Initialize
for i=1:8
    for j=1:8
        ivf1=ivf1+relative_area(i,j)*wms1avg_ivf(i,j);
        ivf2=ivf2+relative_area(i,j)*wms2avg_ivf(i,j);
        ivf12=ivf12+relative_area(i,j)*wms1avg_ivf2(i,j);
        ivf22=ivf22+relative_area(i,j)*wms2avg_ivf2(i,j);
    end
end
fprintf('done.\n');
```

```
gasvelocity; %Run gas velocity measurement script gasvelocity.m
Uiscript; % Run interfacial velocity measurement script Uiscript.m

% Save data
fprintf('Saving data to datfilematrix.mat: ');
datfilematrix(filerow,7)=ivf1; %Save WMS1 AVG IVF
datfilematrix(filerow,8)=ivf2; %Save WMS1 AVG IVF
datfilematrix(filerow,9)=ivf12;
datfilematrix(filerow,10)=ivf22;
datfilematrix(filerow,15)=zerosignal;
datfilematrix(filerow,16)=now; % Time stamp of operation
fprintf('done.\n');
fprintf('\n%s (filerow=%.0f)\nVoid fraction\tTA calib\tHist
calib\nWMS1\t\t\t%3.2f %%\t\t%3.2f %%\nWMS2\t\t\t%3.2f %%\t\t%3.2f
%%\nWMS2 - WMS1\t\t%3.2f%%\t\t%3.2f %%\nAverage\t\t\t%3.2f%%\t\t%3.2f
%%\n',filename,filerow,ivf1*100,ivf12*100,ivf2*100,ivf22*100,(ivf2-
ivf1)*100,(ivf22-ivf12)*100,(ivf1+ivf2)/2*100,(ivf22+ivf12)/2*100);
save('variablesave','datfilematrix','filerow','nij1','nUilecumul','nUit
ecumul','relative_area','Ugij','validnode','Fijdkmax1','cornercut'); %
Save results
filerow=filerow+1; % Link to next file in the directory
end
filerow=filerow-1; % To correct for the while loop
clearvars i j k C R;
fprintf('\nClosing program.\n');
```

Cross-correlation program for gas velocity measurement

```
% Gas velocity measurement
fprintf('Computing gas velocity of %s
(filerow=%.0f)\n',filename,filerow);
load Fijdk1plot;
dkmax=800; Ug=0; Ugnorm=0;
nij1(1:8,1:8,filerow)=ones;Fijdkmax1(1:8,1:8,filerow)=zeros; %
Initialize

% Cross-correlation
for dk=1:dkmax
    denom1(1:8,1:8)=zeros; denom2(1:8,1:8)=zeros; % Initialize
    for i=1:8 % Compute denominators for Eq 1.7, based on the same
quantity of frames as the numerator
        for j=1:8
            if relative_area(i,j)>0
                for k=1:Nframes-dk

denom1(i,j)=denom1(i,j)+(wms1_ivf(i,j,k)-wms1avg_ivf(i,j))^2;

denom2(i,j)=denom2(i,j)+(wms2_ivf(i,j,k)-wms2avg_ivf(i,j))^2;
%                     denom1(i,j)=denom1(i,j)+(wms1_ivf2(i,j,k)-
wms1avg_ivf2(i,j))^2;
%                     denom2(i,j)=denom2(i,j)+(wms2_ivf2(i,j,k)-
wms2avg_ivf2(i,j))^2;
                end
            end
        end
```

```
    end
    for i=1:8
        for j=1:8
            num=0; % Initialize numerator
            if relative_area(i,j)>0 % not corner nodes
                for k=1:Nframes-dk
                    num=num+(wms1_ivf(i,j,k)-
wms1avg_ivf(i,j))*(wms2_ivf(i,j,k+dk)-wms2avg_ivf(i,j));
                    %num=num+(wms1_ivf2(i,j,k)-
wms1avg_ivf2(i,j))*(wms2_ivf2(i,j,k+dk)-wms2avg_ivf2(i,j));
                end

Fijdk(i,j,dk)=num/(sqrt(denom1(i,j))*sqrt(denom2(i,j))); % Eq 1.7
                if Fijdk(i,j,dk)>Fijdkmax1(i,j,filerow)
                    Fijdkmax1(i,j,filerow)=Fijdk(i,j,dk);
                    nij1(i,j,filerow)=dk;
                end
            else
                Fijdk(i,j,dk)=0;nij1(i,j,filerow)=1000000; % Corner
nodes
            end
        end
    end
end
%Determine valid nodes
for i=1:8
    for j=1:8
        if nij1(i,j,filerow)<2 % >108.5 m/s
            validnode(i,j,filerow)=0;
        elseif nij1(i,j,filerow)<20 % >10.85 m/s
            validnode(i,j,filerow)=0*cornercut(i,j);
            %fprintf('Suspiciously high Ugij at %d,%d\n',i,j);
            zerosignal=zerosignal+1;
        elseif nij1(i,j,filerow)>dkmax-3 %
            validnode(i,j,filerow)=0;
        elseif nij1(i,j,filerow)>750 % <.3m/s
            validnode(i,j,filerow)=0;
            %fprintf('Suspiciously low Ugij at %d,%d\n',i,j);
            zerosignal=zerosignal+1;
        elseif max(wms1_ivf(i,j,:))<.5
            validnode(i,j,filerow)=0;
        elseif min(wms1_ivf(i,j,:))>.5
            validnode(i,j,filerow)=0;
        else
            validnode(i,j,filerow)=1*cornercut(i,j);
        end
    end
end
fprintf('Number of valid nodes =
%.0f.\n',sum(sum(validnode(:,:,filerow))));

%Calculate velocity
for i=1:8
    for j=1:8
        %fprintf('%3.0f\t%3.0f\t%3.0f\t%3.0f\n
',i,j,nij1(i,j,filerow),validnode(i,j,filerow));
```

```
        Ugij(i,j,filerow)=0.0226625*f_meas./nij1(i,j,filerow); %
22.6625 mm spacer, 10kHz

Ug=Ug+validnode(i,j,filerow)*Ugij(i,j,filerow)/sum(sum(validnode(:,:,fi
lerow)));

Ugnorm=Ugnorm+validnode(i,j,filerow)*Ugij(i,j,filerow)*Fijdkmax1(i,j,fi
lerow)/sum(sum(validnode(:,:,filerow).*Fijdkmax1(:,:,filerow)));
    end
end

%Fijdkplot
for i=1:8
    for j=1:8
        for k=1:dkmax
            Fijdk1plot(k,(i-
1)*8+j,filerow)=cornercut(i,j)*Fijdk(i,j,k);
        end
    end
end

fprintf('%s (filerow=%.0f)\nUg = %3.2f m/s\tUg norm = %3.2f
m/s\n',filename,filerow,Ug,Ugnorm);

% Save
datfilematrix(filerow,11)=Ug;
datfilematrix(filerow,12)=sum(sum(validnode(:,:,filerow)));
datfilematrix(filerow,13)=max(max(Fijdkmax1(:,:,filerow)));
datfilematrix(filerow,14)=Ugnorm;
save ('Fijdk1plot','Fijdk1plot');


clearvars nom denom1 denom2 dk i j dkmax; %Fijdk nij1 Fijdkmax1
%fprintf('done\n');
```

Average void fraction plot

```
fprintf('Average void fraction plots for wms: \n');

% WMS1
h1=subplot(1,2,1);
set(h1,'position',[0.05 0.2 0.45 0.6]);
imagesc(wms1avg_ivf(:,:)); colorbar('YLim',[0,1]);
set(gca,'YDir','reverse');
title('WMS1 average void fraction');

% % WMS2
h2=subplot(1,2,2);
set(h2,'position',[0.55 0.2 0.45 0.6]);
imagesc(wms2avg_ivf(:,:)); colorbar('YLim',[0,1]);
set(gca,'YDir','reverse');
title('WMS2 average void fraction');
```

Node signal plot

```
clearvars node1 node2 node12 node22;
r=1;c=4; % row and column
kmin=1;
kmax=size(wms1_ivf,3);
for k=kmin:kmax
    node1(k-kmin+1)=wms1_ivf(r,c,k);
    node12(k-kmin+1)=wms1_ivf(r,c,k);
    node2(k-kmin+1)=wms2_ivf(r,c,k);
    node22(k-kmin+1)=wms2_ivf(r,c,k);
    k=k+1;
end

% WMS1 node signal time plot
h1=subplot(2,2,1);
set(h1,'position',[0.05 0.55 0.5 0.425]);
plot(node1);
%axis([kmin kmax 0 1]);
%title('WMS1 node signal');

% % WMS1 node signal histogram by frequency of occurence
h2=subplot(2,2,2);
set(h2,'position',[0.625 0.55 0.35 0.425]);
hist(node12,50);
%title('WMS1 node signal histogram by frequency of occurence');

% WMS2 node signal time plot
h3=subplot(2,2,3);
set(h3,'position',[0.05 0.05 0.5 0.425]);
plot(node2);
%axis([kmin kmax 0 1]);
%title('WMS2 node signal');

% WMS2 node signal histogram by frequency of occurence
h4=subplot(2,2,4);
set(h4,'position',[0.625 0.05 0.35 0.425]);
hist(node22,50);
%title('WMS2 node signal histogram by frequency of occurence');
```

Uncertainty analysis of average velocity

```
% u_Ug calculation script
clear
load cornercut.mat;
load Fijdk1plot;
load Fijdkmax1;
load nij1.mat;
load validnode1;
%load uUg1;
load uUgij1;
load uUgij1relative;
```

```
load u_dtij;
threshold=0.70;
f_meas=10000;

filerow=1;
   while filerow<293
fprintf('%3.0f.',filerow);
% Valid nodes filtering
for i=1:8
    for j=1:8
        if cornercut(i,j)==1
            if Fijdkmax1(i,j,filerow)>=threshold
                validnode1(i,j,filerow)=1;
            else
                validnode1(i,j,filerow)=0;
            end
             if nij1(i,j,filerow)==800
                 validnode1(i,j,filerow)=0;
             end
             if nij1(i,j,filerow)==1
                 validnode1(i,j,filerow)=0;
             end
        else
            validnode1(i,j,filerow)=0;
        end
    end
end

% u_Ug calculation
u_dt2=0;
u_dtij(1:8,1:8,filerow)=zeros;
for i=1:8
    for j=1:8
        ij=(i-1)*8+j;
        if validnode1(i,j,filerow)==1
                for k=1:800
                    abcd(k,ij)=Fijdk1plot(k,ij,filerow); % plot matrix
                end

                min=nij1(i,j,filerow);
                while
Fijdk1plot(min,ij,filerow)>=0.98*Fijdkmax1(i,j,filerow)
                    min=min-1;
                    if min==0
                        break;
                    end
                end
            max=nij1(i,j,filerow);
                while
Fijdk1plot(max,ij,filerow)>=0.98*Fijdkmax1(i,j,filerow)
                    max=max+1;
                    if max==801
                        break;
                    end
                end
```

```
                u_dtij(i,j,filerow)=sqrt(0.5*(min/f_meas-
nij1(i,j,filerow)/f_meas)^2+0.5*(max/f_meas-
nij1(i,j,filerow)/f_meas)^2);


uUgij1(i,j,filerow)=.3/22.7+u_dtij(i,j,filerow)/(nij1(i,j,filerow)/f_me
as);
                %fprintf('%f %f udk=%f\n',i,j,udkmax1(i,j,filerow));
        end
        u_dt2=u_dt2+(validnode1(i,j,filerow)*u_dtij(i,j,filerow))^2;
    end
end
uUgij1relative(:,:,filerow)=uUgij1(:,:,filerow)./(.0226625*f_meas./nij1
(:,:,filerow)).*validnode1(:,:,filerow);
uUg1relative(filerow,1)=sqrt(sum(sum(uUgij1relative(:,:,filerow).^2))/s
um(sum(validnode1(:,:,filerow))));

filerow=filerow+1;
   end
plot(abcd);
load datfilematrix;
% for i=1:245
%     fprintf('%f : %f\n',i, uUg1(i,1)/datfilematrix(i,11));
% end

% Save
save ('uUg1relative','uUg1relative');
save ('uUgij1relative','uUgij1relative');
%save ('uUg1','uUg1');
save ('uUgij1','uUgij1');
save ('u_dtij','u_dtij');
save ('validnode1','validnode1');
```

Interfacial velocity histogram

```
% U histogram
n=1;
clearvars a;
for i=1:1
    for j=3:3
        for k=1:Nframes-1
            if Uile(i,j,k)~=0
                a(n,1)=Uile(i,j,k);
                n=n+1;
            end
        end
    end
end
a=sort(a);
hist(a,50);
```

Appendix C Instrumentation specifications

Details on the assembly of the air injector nozzle are shown in Figure C1 and Figure C2.

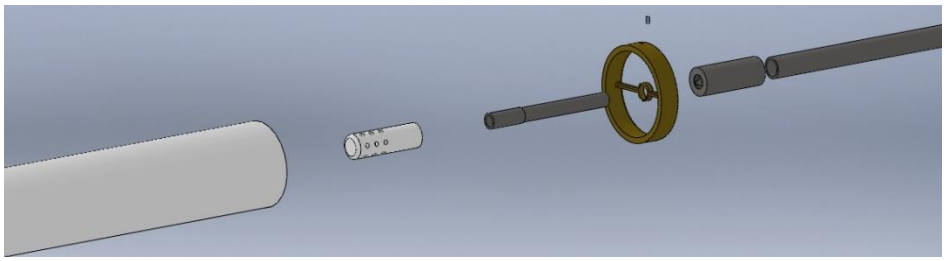

Figure C1: Air injector nozzle assembly

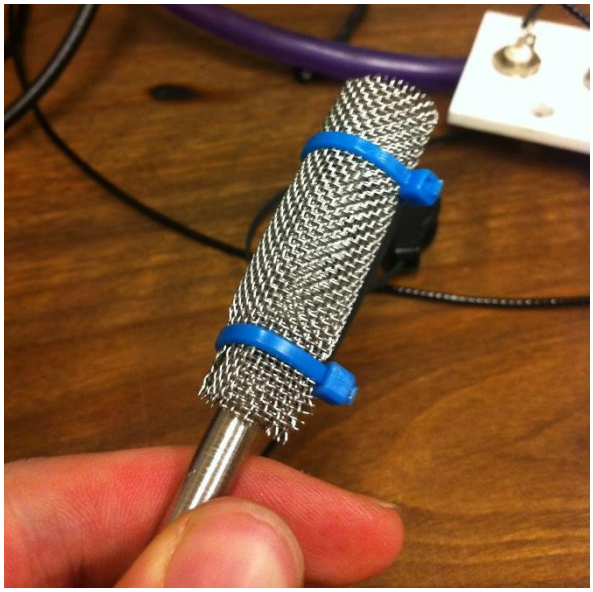

Figure C2: Diffusing mesh assembled on the air injector's nozzle

Further specifications of the FDT-33 transit time ultrasonic water flowmeter (Omega Canada) are shown in Table C1.

Table C1: Water flowmeter specifications (from www.omega.ca)

Description	Specification
Input Voltage	11-30 VDC @ 0.25A
Flow Range Reference	0.1 to 40 FPS [0.03 to 12.4 MPS]
Sch 40 ½" Pipe	0.5 to 25 GPM [20 to 850 BPD]
Sch 40 ¾" Pipe	1.0 to 55 GPM [40 to 1800 BPD]
Sch 40 1" Pipe	2.0 to 100 GPM [80 to 3400 BPD]
Sch 40 1¼" Pipe	4.0 to 150 GPM [170 to 5000 BPD]
Sch 40 1½" Pipe	5.0 to 220 GPM [170 to 7500 BPD]
Sch 40 2" Pipe	8.0 to 400 GPM [275 to 13500 BPD]
Accuracy	±1% of rate above 1 FPS [0.3 MPS]
Environment	Indoor use
Ambient Temperature	General Purpose: 0 to +185°F [-20 to +85°C] Hazardous Area: 0 to +105°F [-20 to +40°C
Altitude	Up to 2000 meters
Humidity	-20º to 31ºC; 80% max; decreasing linearly to 50% at 40ºC
Transient Overvoltages	According to installation category 1, in accordance with IEC 664
Pollution Degree	2 in accordance with IEC 664
Enclosure Material	ABS/Polycarbonate
4-20 mA Output	12-bit, sourcing, DC ground referenced
Pulse Output	Turbine Frequency Output/Pulse Output—Switch Selectable, non-ground referenced AC/Ground referenced square wave, 0-1,000 Hz, 100mVpp minimum/5VDC.

Appendix D Experimental data

The experimental data based on time-averaged calibration are summarized below. Any missing test numbers (such as tests 1-6) correspond to either calibration files or irrelevant files.

Table D1: WMS data

Test #	j_l [m/s]	j_g [m/s]	Flow regime	$\overline{\varepsilon_{1,tac}}$	$\overline{\varepsilon_{2,tac}}$	$\overline{\varepsilon_{1,hc}}$	$\overline{\varepsilon_{2,hc}}$	$\overline{u}$ [m/s]
7	0.55	0.05	Bubbly	0.013	0.026	0.018	0.028	0.73
8	0.55	0.05	Bubbly	0.015	0.029	0.019	0.031	0.75
9	0.57	0.65	Bubbly	0.368	0.326	0.374	0.321	1.75
10	0.57	0.80	Plug	0.397	0.355	0.403	0.349	1.64
11	0.57	0.95	Plug	0.460	0.431	0.465	0.425	1.90
12	0.57	0.95	Plug	0.427	0.403	0.433	0.397	1.92
13	0.57	1.10	Plug	0.476	0.451	0.480	0.442	2.08
14	0.57	1.27	Slug	0.476	0.459	0.478	0.449	2.30
15	0.57	1.44	Slug	0.547	0.518	0.548	0.507	2.07
16	0.57	1.44	Slug	0.545	0.520	0.547	0.509	2.26
17	0.57	1.63	Strat. wavy	0.534	0.511	0.534	0.500	2.30
18	0.86	0.04	Bubbly	0.020	0.021	0.030	0.030	1.06
19	0.85	0.33	Bubbly	0.164	0.160	0.173	0.167	1.51
20	0.85	0.64	Plug	0.317	0.307	0.324	0.311	1.84
21	0.88	0.80	Plug	0.350	0.343	0.357	0.342	2.12
22	0.86	0.96	Plug	0.410	0.398	0.416	0.392	2.13
23	0.87	1.13	Slug	0.406	0.396	0.403	0.388	2.37
24	0.87	1.30	Slug	0.466	0.453	0.468	0.444	2.45
25	0.86	1.49	Slug	0.471	0.454	0.459	0.443	2.49
26	0.85	1.68	Strat. wavy	0.489	0.468	0.480	0.456	2.41
27	1.17	0.04	Bubbly	0.001	0.006	0.018	0.020	1.20
28	1.17	0.31	Bubbly	0.043	0.044	0.059	0.057	1.62
29	1.15	0.63	Plug	0.281	0.274	0.291	0.279	2.12
30	1.14	0.80	Plug	0.304	0.304	0.311	0.305	2.39
31	1.17	0.97	Plug	0.327	0.317	0.332	0.313	2.57
32	1.16	1.15	Plug	0.361	0.348	0.359	0.340	2.61
33	1.16	1.34	Slug	0.396	0.383	0.381	0.373	2.82
34	1.15	1.54	Slug	0.409	0.392	0.393	0.381	2.76
35	1.15	1.74	Slug	0.451	0.436	0.433	0.422	3.14
36	1.15	1.95	Slug	0.440	0.424	0.423	0.411	3.14

Test #	j_l [m/s]	j_g [m/s]	Flow regime	$\overline{\varepsilon_{1,tac}}$	$\overline{\varepsilon_{2,tac}}$	$\overline{\varepsilon_{1,hc}}$	$\overline{\varepsilon_{2,hc}}$	$\overline{u}$ [m/s]
37	1.14	2.17	Slug	0.458	0.441	0.440	0.426	3.08
38	1.17	2.40	Strat. wavy	0.435	0.422	0.417	0.408	3.48
39	1.17	2.64	Strat. wavy	0.471	0.466	0.468	0.443	3.38
40	1.17	2.89	Strat. wavy	0.510	0.507	0.506	0.483	3.60
44	1.49	0.04	Bubbly	0.006	0.008	0.006	0.008	1.27
45	1.47	0.32	Bubbly	0.036	0.038	0.038	0.038	1.73
46	1.44	0.65	Plug	0.237	0.231	0.229	0.224	2.57
47	1.43	0.83	Plug	0.278	0.273	0.269	0.263	2.67
48	1.42	1.00	Plug	0.307	0.302	0.296	0.288	2.80
49	1.43	1.18	Plug	0.328	0.322	0.314	0.304	3.03
50	1.43	1.38	Slug	0.347	0.341	0.331	0.320	3.10
51	1.47	1.57	Slug	0.405	0.402	0.396	0.382	3.87
52	1.47	1.78	Slug	0.420	0.418	0.409	0.398	3.72
53	1.46	2.00	Slug	0.426	0.422	0.417	0.401	3.79
54	1.45	2.23	Slug	0.451	0.447	0.440	0.425	3.90
55	1.44	2.47	Slug	0.475	0.470	0.461	0.446	4.04
56	1.42	2.73	Slug	0.476	0.471	0.457	0.447	3.77
57	1.50	3.00	Slug	0.475	0.471	0.459	0.446	4.55
58	1.48	3.29	Slug	0.478	0.475	0.461	0.449	4.23
59	1.48	3.60	Slug	0.502	0.498	0.485	0.472	4.34
60	1.77	0.04	Bubbly	0.000	0.003	0.008	0.009	1.56
61	1.73	0.33	Bubbly	0.119	0.118	0.115	0.117	2.37
62	1.77	0.68	Plug	0.198	0.197	0.186	0.185	3.03
63	1.78	0.85	Plug	0.225	0.221	0.215	0.211	3.23
64	1.77	1.03	Plug	0.258	0.253	0.246	0.240	3.29
65	1.75	1.22	Slug	0.278	0.273	0.266	0.257	3.49
66	1.73	1.41	Slug	0.293	0.289	0.280	0.268	3.61
67	1.74	1.62	Slug	0.322	0.317	0.306	0.296	3.73
68	1.73	1.83	Slug	0.334	0.328	0.318	0.305	3.90
69	1.72	2.05	Slug	0.349	0.346	0.332	0.322	4.01
70	1.72	2.28	Slug	0.375	0.373	0.359	0.348	4.11
71	1.69	2.53	Slug	0.378	0.375	0.361	0.349	4.23
74	1.95	0.68	Bubbly	0.183	0.183	0.170	0.160	3.19
75	1.94	0.85	Plug	0.210	0.206	0.200	0.197	3.42
76	1.92	1.03	Slug	0.236	0.230	0.227	0.220	3.43
77	1.88	1.22	Slug	0.263	0.258	0.254	0.245	3.61
78	1.85	1.41	Slug	0.293	0.289	0.283	0.273	3.69
79	1.84	1.62	Slug	0.304	0.298	0.293	0.280	3.71
80	1.80	1.83	Slug	0.325	0.322	0.314	0.303	3.95
81	1.77	2.05	Slug	0.347	0.341	0.335	0.321	3.87
82	1.73	2.28	Slug	0.372	0.368	0.359	0.348	4.10

Test #	j_l [m/s]	j_g [m/s]	Flow regime	$\overline{\varepsilon_{1,tac}}$	$\overline{\varepsilon_{2,tac}}$	$\overline{\varepsilon_{1,hc}}$	$\overline{\varepsilon_{2,hc}}$	$\overline{u}$ [m/s]
87	0.12	0.04	Stratified	0.378	0.416	0.377	0.400	0.64
88	0.12	0.34	Stratified	0.459	0.490	0.458	0.475	1.02
89	0.11	0.66	Stratified	0.513	0.533	0.513	0.519	1.07
90	0.10	0.81	Stratified	0.550	0.534	0.551	0.521	1.18
91	0.29	0.04	Stratified	0.106	0.119	0.108	0.120	0.61
92	0.29	0.34	Stratified	0.306	0.317	0.308	0.305	0.99
93	0.30	0.66	Stratified	0.495	0.488	0.496	0.476	1.34
94	0.30	0.81	Stratified	0.468	0.443	0.470	0.429	1.25
95	0.30	0.97	Slug	0.586	0.542	0.587	0.529	1.73
96	0.30	1.13	Slug	0.586	0.574	0.588	0.559	1.56
97	0.30	1.29	Slug	0.559	0.517	0.560	0.504	1.66
98	0.30	1.46	Slug	0.564	0.536	0.560	0.522	2.40
99	0.29	1.63	Slug	0.559	0.511	0.561	0.500	1.82
100	0.29	1.82	Slug	0.607	0.586	0.608	0.573	2.11
101	0.29	2.01	Slug	0.627	0.603	0.628	0.590	2.09
102	0.30	2.22	Slug	0.619	0.583	0.619	0.570	1.67
103	0.30	2.45	Slug	0.701	0.693	0.699	0.679	2.72
104	0.30	2.69	Slug	0.651	0.631	0.650	0.619	1.70
105	0.30	2.96	Strat. wavy	0.665	0.639	0.662	0.626	1.81
106	0.30	3.24	Strat. wavy	0.682	0.669	0.679	0.656	1.84
107	0.29	3.55	Strat. wavy	0.644	0.620	0.644	0.607	1.40
108	0.29	3.89	Strat. wavy	0.657	0.630	0.657	0.618	1.92
109	0.29	4.26	Strat. wavy	0.707	0.693	0.706	0.681	2.07
110	0.29	4.66	Strat. wavy	0.673	0.663	0.673	0.651	1.60
111	0.30	5.10	Strat. wavy	0.691	0.668	0.690	0.656	2.78
112	0.30	5.58	Strat. wavy	0.687	0.670	0.685	0.659	2.03
113	0.29	6.10	Strat. wavy	0.673	0.658	0.673	0.644	2.10
114	0.29	6.66	Strat. wavy	0.693	0.688	0.692	0.675	2.77
115	0.29	7.28	Strat. wavy	0.675	0.667	0.674	0.655	2.03
116	0.28	7.95	Strat. wavy	0.729	0.718	0.722	0.700	2.89
117	0.29	8.67	Strat. wavy	0.743	0.731	0.737	0.716	2.59
118	0.30	9.46	Strat. wavy	0.744	0.734	0.738	0.720	3.29
119	0.26	10.31	Strat. wavy	0.713	0.713	0.712	0.701	2.46
120	0.27	11.24	Strat. wavy	0.727	0.721	0.726	0.709	1.86
121	0.27	12.24	Strat. wavy	0.747	0.747	0.738	0.734	3.54
122	0.27	13.32	Strat. wavy	0.743	0.743	0.741	0.731	2.75
123	0.27	14.48	Strat. wavy	0.749	0.749	0.746	0.737	2.17
124	0.27	15.73	Strat. wavy	0.766	0.762	0.757	0.749	2.43
125	0.27	17.08	Strat. wavy	0.759	0.758	0.756	0.744	3.22
126	0.26	18.54	Strat. wavy	0.725	0.727	0.716	0.712	3.30
127	0.26	20.10	Strat. wavy	0.728	0.731	0.725	0.718	2.65
128	0.26	21.77	Strat. wavy	0.733	0.732	0.730	0.719	2.26

Test #	j_l [m/s]	j_g [m/s]	Flow regime	$\overline{\varepsilon_{1,tac}}$	$\overline{\varepsilon_{2,tac}}$	$\overline{\varepsilon_{1,hc}}$	$\overline{\varepsilon_{2,hc}}$	$\overline{u}$ [m/s]
129	0.25	23.56	Strat. wavy	0.729	0.730	0.725	0.716	3.34
135	0.43	0.04	Bubbly	-0.002	0.005	0.004	0.004	0.39
136	0.43	0.31	Plug	0.098	0.106	0.103	0.105	0.79
137	0.42	0.64	Slug	0.467	0.429	0.470	0.418	1.63
138	0.41	0.80	Slug	0.460	0.438	0.463	0.425	1.62
139	0.41	0.98	Slug	0.554	0.523	0.557	0.511	1.77
140	0.41	1.15	Slug	0.548	0.527	0.551	0.515	1.76
141	0.42	1.33	Strat. wavy	0.607	0.594	0.610	0.581	1.97
142	0.40	1.52	Strat. wavy	0.632	0.623	0.633	0.610	2.06
143	0.40	1.71	Strat. wavy	0.588	0.577	0.589	0.564	1.88
144	0.42	1.91	Strat. wavy	0.632	0.621	0.634	0.607	1.95
145	0.40	2.12	Strat. wavy	0.632	0.621	0.634	0.608	2.04
146	0.40	2.33	Strat. wavy	0.638	0.629	0.639	0.615	2.13
147	0.41	2.56	Strat. wavy	0.646	0.635	0.645	0.621	2.13
148	0.41	2.79	Strat. wavy	0.655	0.646	0.655	0.632	2.28
149	0.39	3.03	Strat. wavy	0.683	0.674	0.683	0.660	2.78
150	0.39	3.28	Strat. wavy	0.713	0.703	0.711	0.689	2.62
151	0.42	3.53	Strat. wavy	0.637	0.628	0.635	0.612	1.88
152	0.39	3.80	Strat. wavy	0.665	0.658	0.662	0.643	2.50
153	0.39	4.08	Strat. wavy	0.688	0.680	0.686	0.666	2.46
154	0.41	4.37	Strat. wavy	0.679	0.673	0.679	0.659	2.79
155	0.40	4.68	Strat. wavy	0.696	0.690	0.695	0.676	2.64
156	0.39	4.99	Strat. wavy	0.689	0.683	0.687	0.668	2.04
157	0.41	5.32	Strat. wavy	0.689	0.686	0.688	0.672	2.76
158	0.39	5.66	Strat. wavy	0.705	0.700	0.699	0.685	2.48
159	0.40	6.01	Strat. wavy	0.711	0.707	0.706	0.691	2.44
160	0.40	6.38	Strat. wavy	0.702	0.699	0.696	0.682	2.77
161	0.42	6.76	Strat. wavy	0.754	0.750	0.740	0.730	4.04
162	0.42	7.16	Strat. wavy	0.740	0.737	0.731	0.720	2.89
163	0.39	7.57	Strat. wavy	0.728	0.726	0.725	0.710	3.30
164	0.39	7.99	Strat. wavy	0.752	0.747	0.741	0.729	3.13
165	0.41	8.43	Strat. wavy	0.731	0.729	0.727	0.711	2.82
166	0.41	8.89	Strat. wavy	0.746	0.744	0.734	0.725	2.85
167	0.40	9.36	Strat. wavy	0.732	0.729	0.728	0.714	2.60
168	0.39	9.85	Strat. wavy	0.735	0.731	0.731	0.716	3.48
169	0.41	10.36	Strat. wavy	0.737	0.736	0.732	0.721	2.80
170	0.42	10.88	Strat. wavy	0.730	0.730	0.724	0.713	2.91
171	0.42	11.42	Strat. wavy	0.753	0.752	0.741	0.734	3.34
172	0.41	11.97	Strat. wavy	0.734	0.733	0.728	0.717	3.03
173	0.40	12.55	Strat. wavy	0.746	0.745	0.740	0.729	3.46
175	0.72	0.09	Bubbly	0.012	0.015	0.015	0.017	0.74
176	0.69	0.33	Bubbly	0.061	0.057	0.064	0.059	0.99

Test #	j_l [m/s]	j_g [m/s]	Flow regime	$\overline{\varepsilon_{1,tac}}$	$\overline{\varepsilon_{2,tac}}$	$\overline{\varepsilon_{1,hc}}$	$\overline{\varepsilon_{2,hc}}$	$\overline{u}$ [m/s]
177	0.73	0.65	Slug	0.393	0.383	0.395	0.377	1.88
178	0.72	0.82	Slug	0.441	0.431	0.443	0.421	1.97
179	0.72	0.98	Strat. wavy	0.476	0.465	0.477	0.454	2.08
180	0.72	1.14	Strat. wavy	0.526	0.517	0.524	0.505	2.18
181	0.68	1.31	Strat. wavy	0.554	0.546	0.550	0.532	2.39
182	0.68	1.49	Strat. wavy	0.549	0.537	0.547	0.524	2.10
183	0.72	1.67	Strat. wavy	0.553	0.545	0.550	0.530	2.48
184	0.72	1.87	Strat. wavy	0.574	0.566	0.569	0.550	2.59
185	0.71	2.07	Strat. wavy	0.577	0.568	0.572	0.552	2.60
186	0.72	2.29	Strat. wavy	0.603	0.595	0.598	0.578	2.88
187	0.70	2.52	Strat. wavy	0.597	0.589	0.592	0.573	2.93
188	0.69	2.77	Strat. wavy	0.572	0.562	0.566	0.549	2.73
189	0.71	3.04	Strat. wavy	0.605	0.594	0.598	0.579	2.96
190	0.68	3.32	Strat. wavy	0.632	0.623	0.624	0.605	3.01
191	0.70	3.63	Strat. wavy	0.591	0.580	0.584	0.566	2.76
192	0.69	3.96	Strat. wavy	0.647	0.638	0.641	0.620	3.10
193	0.68	4.32	Strat. wavy	0.641	0.631	0.627	0.609	3.56
194	0.75	4.70	Strat. wavy	0.607	0.600	0.591	0.578	3.42
195	0.75	5.12	Strat. wavy	0.654	0.650	0.639	0.631	3.66
196	0.72	5.56	Strat. wavy	0.671	0.664	0.653	0.639	4.06
197	0.70	6.05	Strat. wavy	0.676	0.672	0.648	0.643	4.22
198	0.69	6.56	Strat. wavy	0.659	0.653	0.642	0.629	3.95
199	0.74	7.12	Strat. wavy	0.675	0.669	0.657	0.646	4.19
200	0.72	7.72	Strat. wavy	0.665	0.660	0.651	0.636	3.98
201	0.70	8.37	Strat. wavy	0.675	0.669	0.659	0.645	4.13
202	0.70	9.06	Strat. wavy	0.685	0.680	0.666	0.655	4.50
203	0.72	9.80	Strat. wavy	0.700	0.693	0.680	0.670	4.34
204	0.71	10.60	Strat. wavy	0.692	0.687	0.669	0.660	4.29
205	0.70	11.46	Strat. wavy	0.717	0.711	0.698	0.685	5.16
206	0.69	12.37	Strat. wavy	0.706	0.700	0.681	0.673	4.78
208	1.03	0.08	Bubbly	0.007	0.009	0.008	0.010	0.92
209	1.02	0.33	Bubbly	0.057	0.054	0.059	0.056	1.33
210	0.97	0.65	Slug	0.371	0.362	0.371	0.358	2.07
211	1.05	0.82	Slug	0.385	0.381	0.379	0.368	2.44
212	1.05	0.99	Strat. wavy	0.429	0.421	0.420	0.405	2.58
213	1.03	1.16	Strat. wavy	0.467	0.459	0.459	0.442	2.68
214	1.01	1.34	Strat. wavy	0.485	0.475	0.475	0.457	2.61
215	1.00	1.53	Strat. wavy	0.493	0.482	0.484	0.465	2.69
216	1.00	1.73	Strat. wavy	0.530	0.522	0.519	0.500	2.82
217	0.97	1.94	Strat. wavy	0.536	0.527	0.524	0.508	2.93
218	0.95	2.15	Strat. wavy	0.527	0.514	0.516	0.496	2.82
219	1.05	2.39	Strat. wavy	0.543	0.532	0.527	0.508	3.21

Test #	j_l [m/s]	j_g [m/s]	Flow regime	$\overline{\varepsilon_{1,tac}}$	$\overline{\varepsilon_{2,tac}}$	$\overline{\varepsilon_{1,hc}}$	$\overline{\varepsilon_{2,hc}}$	$\overline{u}$ [m/s]
220	1.05	2.63	Strat. wavy	0.552	0.543	0.539	0.520	3.20
221	1.03	2.89	Strat. wavy	0.564	0.554	0.551	0.534	3.19
222	1.02	3.17	Strat. wavy	0.589	0.580	0.569	0.553	3.50
223	1.02	3.47	Strat. wavy	0.573	0.561	0.551	0.537	3.45
224	1.01	3.78	Strat. wavy	0.591	0.581	0.573	0.559	3.55
225	1.01	4.12	Strat. wavy	0.623	0.613	0.598	0.587	4.11
226	0.99	4.48	Strat. wavy	0.610	0.602	0.590	0.578	3.79
227	1.00	4.86	Strat. wavy	0.598	0.586	0.570	0.549	3.82
228	0.99	5.28	Strat. wavy	0.621	0.613	0.599	0.580	4.27
229	0.97	5.71	Strat. wavy	0.634	0.627	0.607	0.604	4.29
230	0.96	6.18	Strat. wavy	0.656	0.646	0.616	0.606	4.72
231	0.97	6.68	Strat. wavy	0.651	0.643	0.621	0.613	4.53
232	0.96	7.22	Strat. wavy	0.657	0.649	0.616	0.609	4.63
233	1.05	7.79	Strat. wavy	0.652	0.646	0.621	0.608	5.00
234	1.04	8.39	Strat. wavy	0.663	0.656	0.623	0.607	5.00
235	1.02	9.04	Strat. wavy	0.667	0.661	0.629	0.619	5.19
236	1.00	9.72	Strat. wavy	0.675	0.670	0.647	0.643	5.34
237	0.98	10.45	Strat. wavy	0.686	0.681	0.648	0.639	5.70
238	0.97	11.22	Strat. wavy	0.678	0.672	0.642	0.631	5.46
239	0.97	12.04	Strat. wavy	0.684	0.679	0.648	0.642	5.69
243	1.35	0.08	Bubbly	0.003	0.002	0.003	0.004	1.10
244	1.31	0.33	Bubbly	0.083	0.080	0.084	0.082	1.65
245	1.30	0.65	Plug	0.296	0.291	0.290	0.281	2.46
246	1.30	0.82	Plug	0.339	0.339	0.330	0.316	2.63
247	1.30	0.99	Slug	0.373	0.371	0.361	0.339	2.78
248	1.30	1.16	Slug	0.409	0.409	0.396	0.370	2.96
249	1.26	1.34	Strat. wavy	0.433	0.431	0.419	0.397	3.07
250	1.24	1.53	Strat. wavy	0.465	0.458	0.448	0.426	3.03
251	1.24	1.73	Strat. wavy	0.487	0.476	0.469	0.448	3.21
252	1.24	1.94	Strat. wavy	0.478	0.466	0.465	0.438	3.19
253	1.36	2.15	Strat. wavy	0.477	0.471	0.456	0.443	3.52
254	1.36	2.39	Strat. wavy	0.502	0.495	0.474	0.465	4.04
255	1.34	2.63	Strat. wavy	0.494	0.488	0.470	0.458	3.73
256	1.32	2.89	Strat. wavy	0.523	0.517	0.503	0.488	3.72
257	1.31	3.17	Ann. misty	0.539	0.531	0.517	0.501	3.74
258	1.31	3.47	Ann. misty	0.548	0.542	0.528	0.512	3.97
259	1.28	3.78	Ann. misty	0.553	0.545	0.525	0.515	4.04
260	1.26	4.12	Ann. misty	0.579	0.573	0.554	0.546	4.19
261	1.26	4.48	Ann. misty	0.590	0.584	0.566	0.554	4.37
262	1.25	4.86	Ann. misty	0.582	0.574	0.556	0.544	4.14
263	1.23	5.28	Ann. misty	0.602	0.596	0.570	0.560	4.71
264	1.23	5.71	Ann. misty	0.599	0.592	0.566	0.547	4.65

Test #	j_l [m/s]	j_g [m/s]	Flow regime	$\overline{\varepsilon_{1,tac}}$	$\overline{\varepsilon_{2,tac}}$	$\overline{\varepsilon_{1,hc}}$	$\overline{\varepsilon_{2,hc}}$	$\overline{u}$ [m/s]
265	1.34	6.18	Ann. misty	0.581	0.575	0.539	0.529	4.92
266	1.33	6.68	Ann. misty	0.604	0.598	0.567	0.558	5.10
268	1.65	0.08	Bubbly	0.002	0.003	0.003	0.004	N/A
269	1.62	0.34	Bubbly	0.076	0.078	0.076	0.077	1.97
270	1.61	0.69	Plug	0.265	0.265	0.251	0.244	2.86
271	1.59	0.86	Plug	0.309	0.310	0.291	0.285	3.00
272	1.57	1.05	Plug	0.336	0.336	0.317	0.309	3.11
273	1.54	1.24	Plug	0.371	0.369	0.352	0.339	3.26
274	1.53	1.43	Plug	0.395	0.392	0.376	0.362	3.40
275	1.52	1.64	Plug	0.415	0.409	0.392	0.378	3.52
276	1.66	1.85	Plug	0.415	0.411	0.390	0.378	3.97
277	1.65	2.07	Slug	0.424	0.421	0.399	0.388	4.05
278	1.62	2.30	Slug	0.460	0.455	0.434	0.421	4.27
279	1.59	2.54	Slug	0.470	0.464	0.445	0.430	4.22
280	1.58	2.80	Slug	0.475	0.469	0.448	0.435	4.29
281	1.56	3.07	Slug	0.494	0.489	0.469	0.456	4.39
282	1.54	3.36	Slug	0.517	0.511	0.486	0.476	4.63
283	1.52	3.66	Ann. misty	0.515	0.508	0.486	0.475	4.53
284	1.56	3.99	Ann. misty	0.498	0.491	0.468	0.457	4.47
285	1.55	4.33	Ann. misty	0.541	0.535	0.510	0.500	5.02
286	1.52	4.70	Ann. misty	0.540	0.533	0.503	0.497	5.17
288	1.88	0.08	Bubbly	0.007	0.011	0.005	0.007	N/A
289	1.93	0.34	Bubbly	0.106	0.117	0.090	0.081	2.59
290	1.95	0.69	Plug	0.240	0.244	0.218	0.211	3.21
291	1.92	0.86	Plug	0.283	0.283	0.259	0.256	3.37
292	1.88	1.05	Plug	0.307	0.304	0.282	0.273	3.50
293	1.87	1.24	Slug	0.334	0.332	0.311	0.298	3.67
294	1.84	1.43	Slug	0.361	0.357	0.333	0.322	3.79
295	1.85	1.64	Slug	0.387	0.383	0.360	0.348	3.90
296	1.84	1.85	Ann. misty	0.403	0.398	0.375	0.364	4.05
299	0.57	0.64	Plug	0.441	0.425	0.441	0.416	1.72
300	0.58	1.15	Plug	0.523	0.508	0.521	0.497	1.99
301	0.58	1.71	Strat. wavy	0.585	0.574	0.584	0.562	2.41
302	1.15	0.65	Strat. wavy	0.329	0.325	0.327	0.320	2.27
303	1.18	1.16	Strat. wavy	0.406	0.399	0.397	0.380	2.71
304	1.15	1.73	Strat. wavy	0.499	0.490	0.488	0.467	3.14
305	1.16	2.39	Strat. wavy	0.515	0.506	0.503	0.481	3.26
306	1.16	3.17	Strat. wavy	0.531	0.520	0.512	0.493	3.40
307	1.16	4.12	Slug	0.590	0.582	0.566	0.552	3.92
308	1.15	5.28	Slug	0.602	0.593	0.570	0.560	4.23
309	1.13	6.68	Ann. misty	0.616	0.607	0.580	0.564	4.66
310	1.16	8.39	Ann. misty	0.650	0.645	0.611	0.597	5.54

Test #	j_l [m/s]	j_g [m/s]	Flow regime	$\overline{\varepsilon_{1,tac}}$	$\overline{\varepsilon_{2,tac}}$	$\overline{\varepsilon_{1,hc}}$	$\overline{\varepsilon_{2,hc}}$	$\overline{u}$ [m/s]
311	1.16	10.45	Ann. misty	0.654	0.649	0.613	0.600	5.59
312	1.77	0.69	Plug	0.247	0.249	0.233	0.229	3.05
313	1.74	1.24	Plug	0.338	0.336	0.320	0.308	3.47
314	1.73	1.85	Strat. wavy	0.396	0.393	0.374	0.361	3.89
315	1.67	2.54	Strat. wavy	0.457	0.454	0.432	0.423	4.36

Appendix E High-speed photography data

The data collected from the high-speed photography interfacial velocity measurements is shown in Table E1.

Table E1: High-speed photography data

j_l [m/s]	t_2 (s)	x_2	t_1 (s)	x_1	$\mathcal{U}_{lg}$ [m/s]	$u_{\mathcal{U}_{lg}}$ [m/s]
0.446	47.353	2255	47.756	6	0.443	0.015
0.446	48.026	2548	48.514	16	0.413	0.012
0.446	48.155	2543	48.647	15	0.408	0.012
0.446	48.350	2553	48.828	3	0.423	0.013
0.446	48.483	2546	48.952	15	0.428	0.013
0.446	48.629	2549	48.970	803	0.406	0.016
0.666	46.707	1948	46.920	56	0.706	0.037
0.666	46.933	2556	47.248	73	0.627	0.024
0.666	46.964	2533	47.279	49	0.627	0.024
0.666	47.279	2541	47.580	27	0.663	0.026
0.666	47.571	2548	47.904	46	0.598	0.022
0.666	47.691	2546	48.023	24	0.603	0.022
0.666	47.735	2551	48.032	8	0.680	0.027
0.666	47.957	2501	48.258	32	0.651	0.026
0.789	52.656	1730	52.820	51	0.824	0.052
0.789	52.656	1947	52.834	34	0.868	0.051
0.789	52.714	2523	53.020	22	0.658	0.024
0.789	52.798	2544	53.060	4	0.782	0.033
0.789	52.980	2551	53.255	72	0.726	0.029
0.789	53.157	2527	53.432	3	0.739	0.030
0.789	53.405	2533	53.680	30	0.733	0.030
0.789	53.529	2546	53.795	3	0.770	0.032
0.789	53.773	2509	54.039	34	0.749	0.031
0.789	54.052	2527	54.301	242	0.741	0.033
1.063	46.139	2126	46.320	8	0.935	0.053
1.063	46.139	2449	46.325	60	1.029	0.057
1.063	46.258	2546	46.449	75	1.040	0.057
1.063	46.471	2505	46.666	18	1.023	0.055
1.063	46.511	2539	46.706	15	1.038	0.056
1.063	46.551	2514	46.759	77	0.938	0.048
1.063	46.599	2531	46.808	55	0.953	0.048
1.063	46.790	2482	47.007	43	0.901	0.044

j_l [m/s]	t_2 (s)	x_2	t_1 (s)	x_1	$\mathcal{U}_{lg}$ [m/s]	$u_{\mathcal{U}_{lg}}$ [m/s]
1.063	46.830	2523	47.012	89	1.074	0.061
1.063	46.874	2519	47.096	31	0.900	0.043
1.063	46.923	2515	47.127	34	0.976	0.050
1.063	46.932	2514	47.127	92	0.996	0.053
1.063	46.941	2545	47.136	64	1.020	0.055
1.063	46.958	2545	47.140	56	1.099	0.063
1.063	46.967	2547	47.158	30	1.059	0.058
1.063	46.980	2516	47.171	0	1.059	0.058
1.063	46.989	2550	47.184	33	1.035	0.056
1.063	47.078	2535	47.300	25	0.908	0.044
1.063	47.193	2515	47.384	30	1.046	0.057
1.063	47.202	2544	47.384	77	1.089	0.062
1.063	47.211	2553	47.397	31	1.087	0.061
1.063	47.233	2542	47.419	77	1.062	0.059
1.063	47.335	2522	47.530	3	1.036	0.056
1.063	47.397	2537	47.583	43	1.075	0.060
1.063	47.410	2527	47.601	79	1.030	0.056
1.171	2.964	2494	3.150	3	1.077	0.060
1.171	2.978	2532	3.177	58	0.998	0.053
1.171	3.017	2527	3.204	36	1.077	0.060
1.171	3.097	2542	3.283	6	1.096	0.061
1.171	3.283	2496	3.469	71	1.048	0.059
1.171	3.328	2545	3.514	20	1.092	0.061
1.171	3.403	2532	3.594	3	1.068	0.058
1.171	3.438	2553	3.625	20	1.095	0.061
1.171	3.478	2540	3.678	74	0.995	0.052
1.263	44.185	2317	44.336	17	1.228	0.082
1.263	44.234	2474	44.402	48	1.159	0.071
1.263	44.313	2458	44.486	20	1.135	0.068
1.263	44.415	2488	44.584	21	1.179	0.072
1.263	44.513	2491	44.699	60	1.051	0.059
1.263	44.557	2500	44.726	70	1.161	0.071
1.263	44.601	2543	44.801	43	1.009	0.053
1.263	44.646	2510	44.819	42	1.149	0.068
1.501	0.056	2254	0.175	98	1.455	0.120
1.501	0.242	2460	0.375	165	1.393	0.105
1.501	0.273	2529	0.419	159	1.308	0.090
1.501	0.787	2510	0.937	2	1.344	0.090
1.501	1.208	2523	1.336	157	1.486	0.115
1.501	1.230	2497	1.358	106	1.502	0.116

Appendix F Drift-flux plots for constant interfacial liquid velocity measurements

The following graphs represent the drift-flux model constants c_0 and v_{gj} for each group of measurements sets at an approximately constant water superficial velocity j_l, in the order in which they were taken as shown in Table D1.

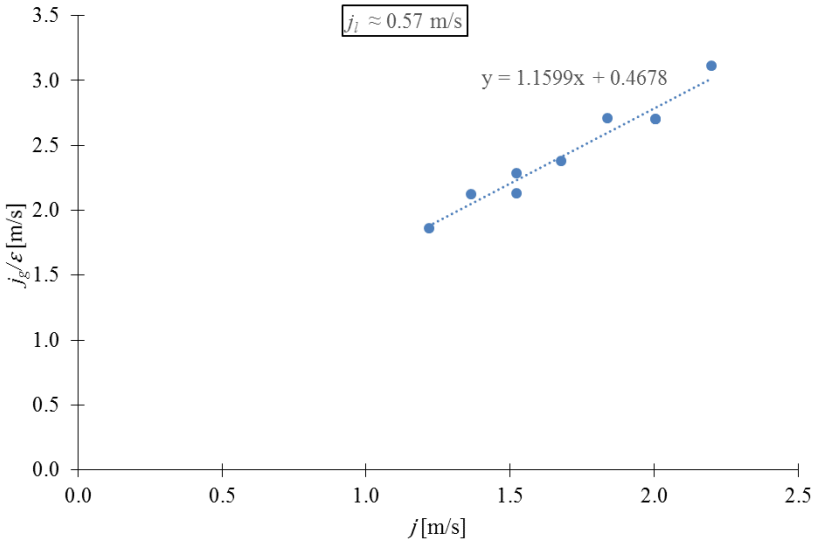

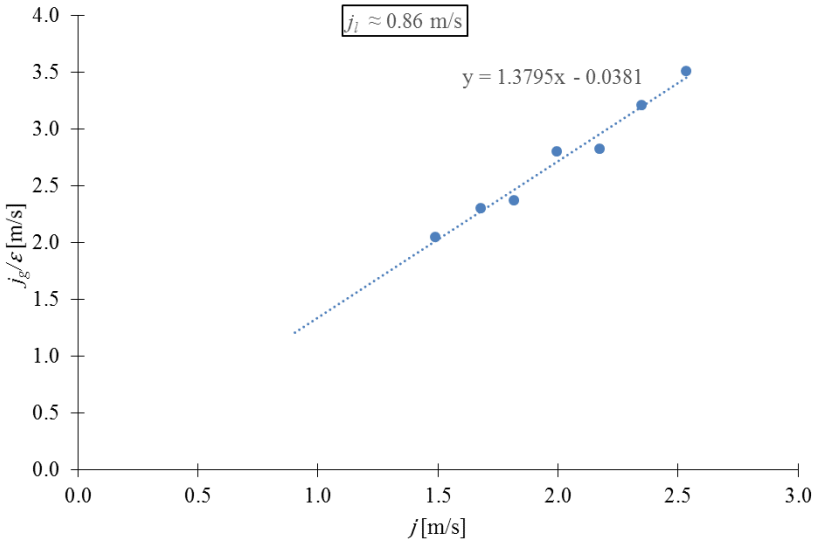

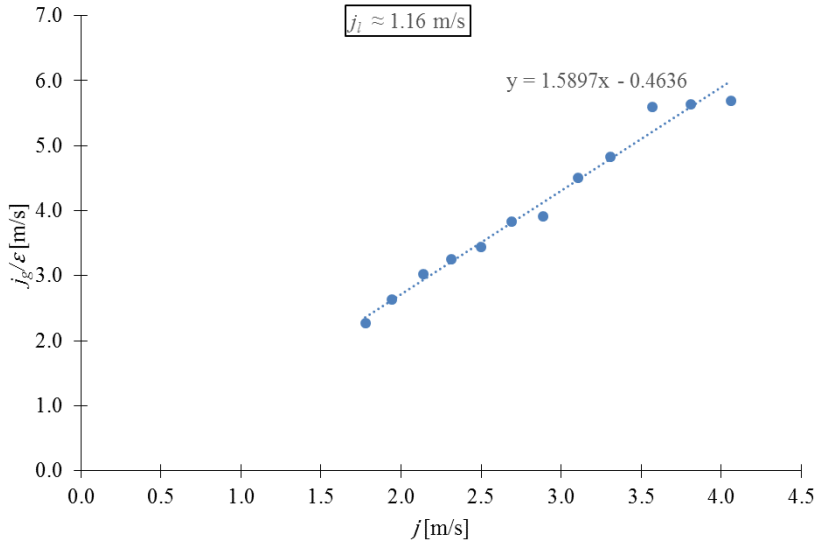
$j_l \approx 1.16$ m/s
y = 1.5897x - 0.4636
j_g/ε [m/s]
j [m/s]
0.0
1.0
2.0
3.0
4.0
5.0
6.0
7.0
0.5
1.5
2.5
3.5
4.5

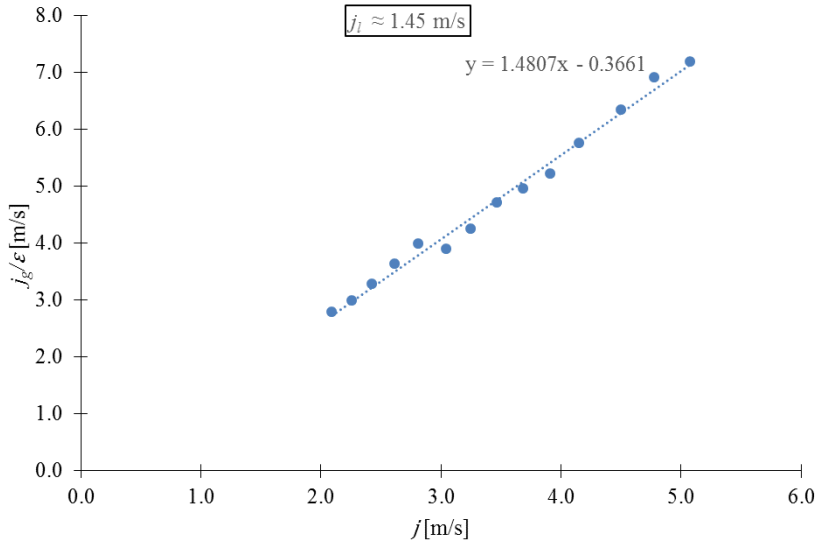
$j_l \approx 1.45$ m/s
y = 1.4807x - 0.3661
j_g/ε [m/s]
j [m/s]
0.0
1.0
2.0
3.0
4.0
5.0
6.0
7.0
8.0

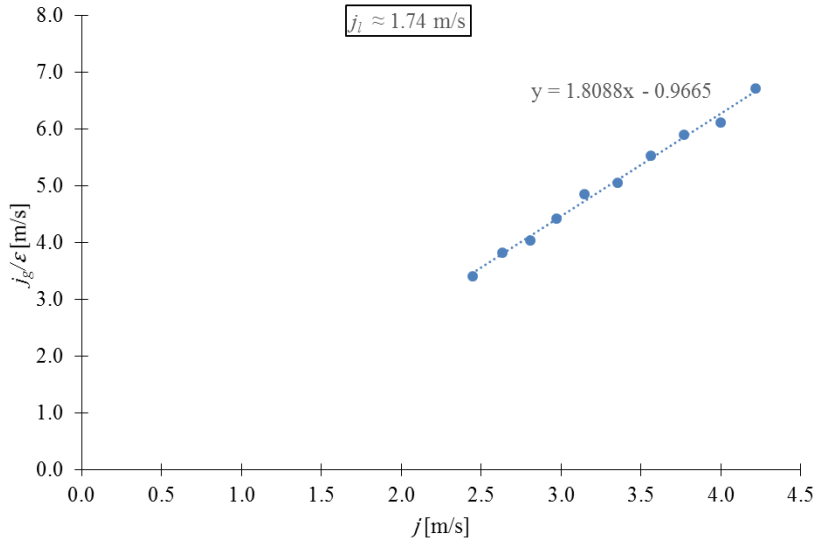
$j_l \approx 1.74$ m/s
y = 1.8088x - 0.9665
j_g/ε [m/s]
j [m/s]
0.0
1.0
2.0
3.0
4.0
5.0
6.0
7.0
8.0
0.5
1.5
2.5
3.5
4.5

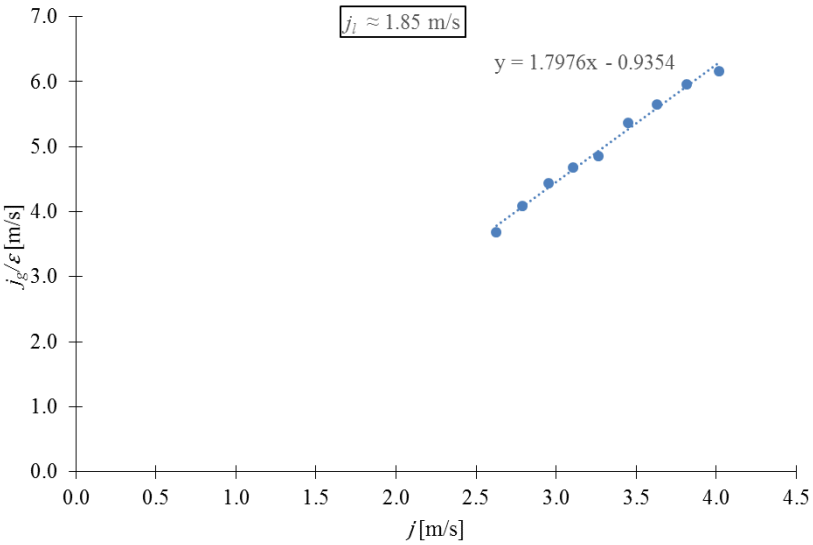
$j_l \approx 1.85$ m/s
y = 1.7976x - 0.9354
j_g/ε [m/s]
j [m/s]
0.0
1.0
2.0
3.0
4.0
5.0
6.0
7.0
0.0
0.5
1.0
1.5
2.0
2.5
3.0
3.5
4.0
4.5

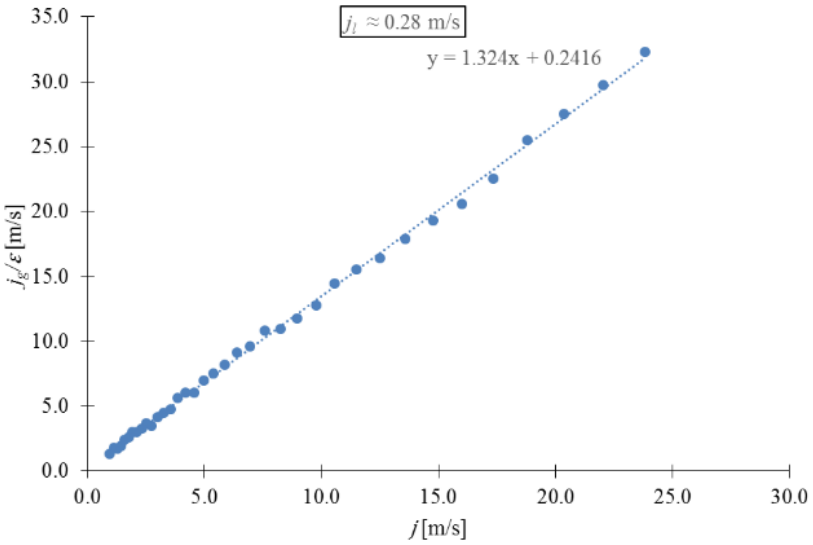
$j_l \approx 0.28$ m/s
y = 1.324x + 0.2416
j_g/ε [m/s]
j [m/s]
0.0
5.0
10.0
15.0
20.0
25.0
30.0
35.0
0.0
5.0
10.0
15.0
20.0
25.0
30.0

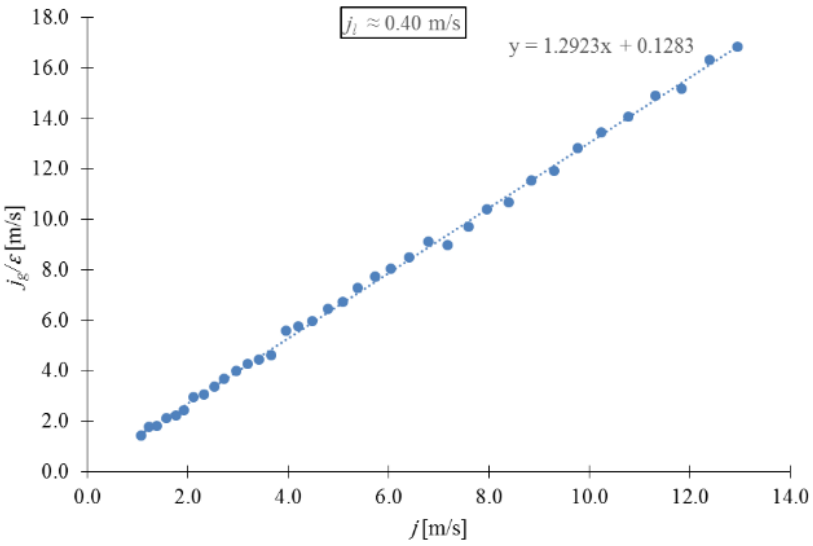
$j_l \approx 0.40$ m/s
y = 1.2923x + 0.1283
j_g/ε [m/s]
j [m/s]
0.0
2.0
4.0
6.0
8.0
10.0
12.0
14.0
16.0
18.0
0.0
2.0
4.0
6.0
8.0
10.0
12.0
14.0

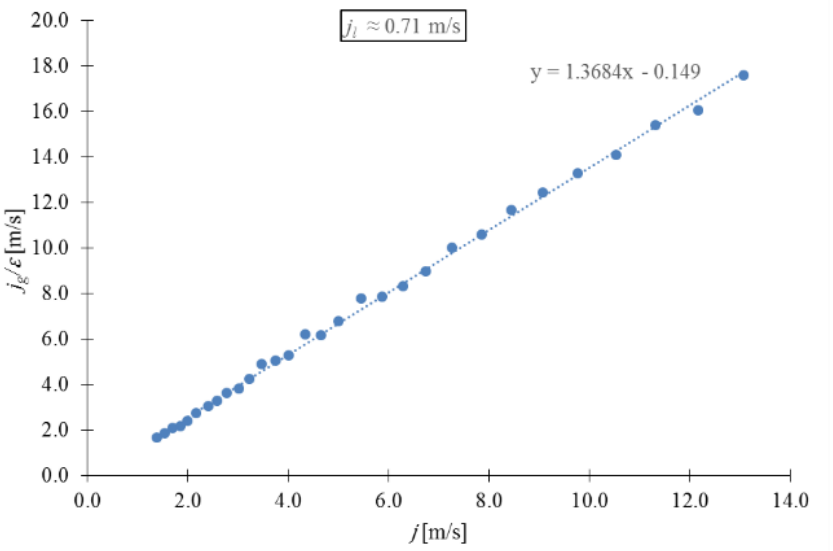
$j_l \approx 0.71$ m/s
y = 1.3684x - 0.149
j_g/ε [m/s]
j [m/s]
0.0
2.0
4.0
6.0
8.0
10.0
12.0
14.0
16.0
18.0
20.0

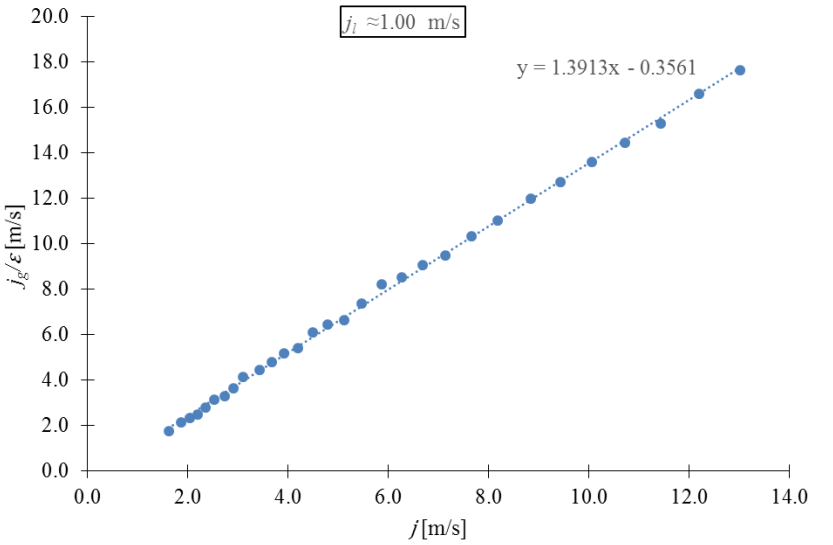
$j_l \approx 1.00$ m/s
y = 1.3913x - 0.3561
j_g/ε [m/s]
j [m/s]
0.0
2.0
4.0
6.0
8.0
10.0
12.0
14.0
16.0
18.0
20.0

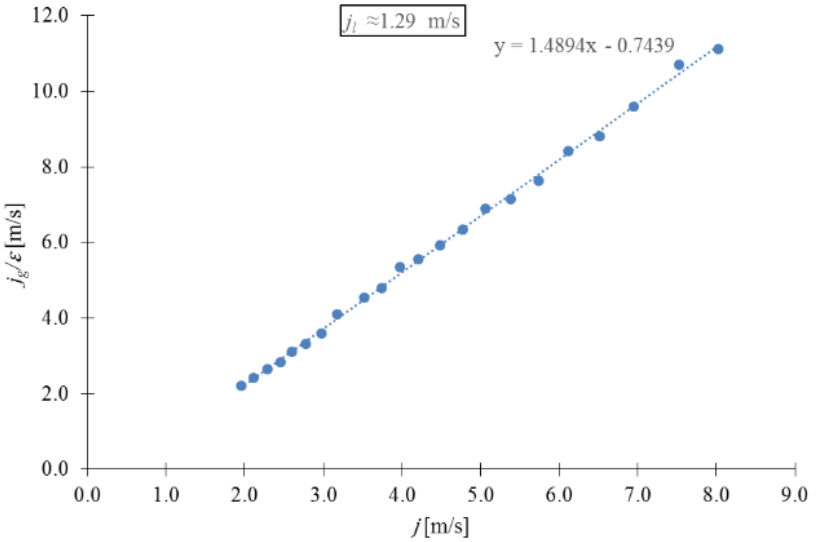
$j_l \approx 1.29$ m/s
y = 1.4894x - 0.7439
j_g/ε [m/s]
j [m/s]
0.0
1.0
2.0
3.0
4.0
5.0
6.0
7.0
8.0
9.0
10.0
12.0

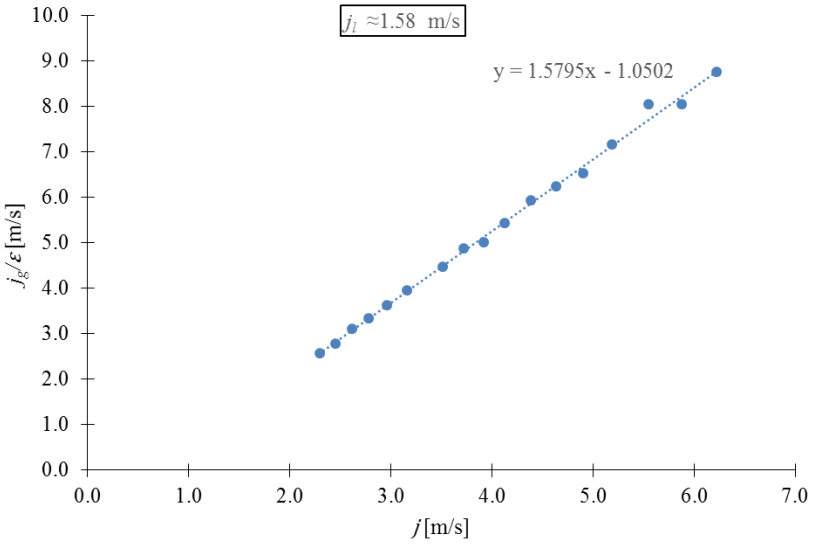
j_l ≈1.58 m/s
y = 1.5795x - 1.0502
j_g/ε [m/s]
j [m/s]
0.0
1.0
2.0
3.0
4.0
5.0
6.0
7.0
8.0
9.0
10.0

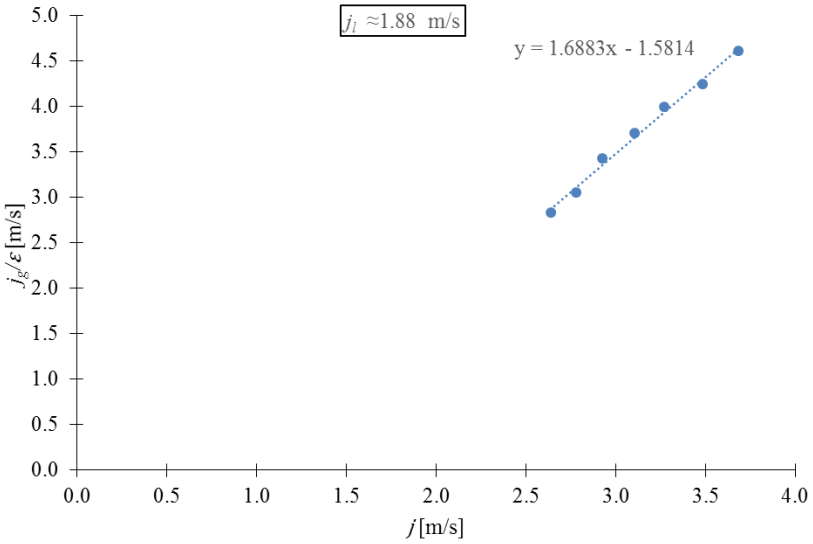
j_l ≈1.88 m/s
y = 1.6883x - 1.5814
j_g/ε [m/s]
j [m/s]
0.0
0.5
1.0
1.5
2.0
2.5
3.0
3.5
4.0
4.5
5.0